University of Liège
Faculty of Sciences
Space sciences, Technologies and Astrophysics Research
(STAR) Institute

Space debris detection and characterization with the 4m International Liquid Mirror Telescope (ILMT)

Author:
Bikram Pradhan

Supervisor:
Prof. Jean Surdej
Co-supervisor:
Prof. Serge HABRAKEN

A thesis submitted in fulfillment of the requirements
for the degree of Doctor of Philosophy in Space Science
in the
Planetary and Stellar systems Imaging Laboratory (PSILab) group
Space sciences, Technologies and Astrophysics Research (STAR)
Institute

October 2019

Members of the jury:

Prof. Jérôme Loicq (ULg, FSA & CSL)	**President**
Prof. Serge Habraken (ULg, FS)	**Co-promoter**
Dr. Peter De Cat (Observatoire Royal de Belgique) Prof. Philippe Dierickx (ESO, München, Allemagne) Dr. Christian Barbier (ULg, CSL) Dr. Tim Flohrer (ESA-ESOC, Darmstadt, Allemagne)	
Dr. Michaël De Becker (ULg, FS)	**Secretary**
Prof. Jean Surdej (ULg, FS)	**Promoter** (Supervisor)

"Only two things are infinite, the universe and human stupidity, and I'm not sure about the former."

Albert Einstein, 1936

Acknowledgements

At the end of my 4 years of compelling and captivating PhD journey, I find myself as a new person who questions and tries to improve continuously. Thanks to my supervisor Prof. Jean, who has groomed me to lead an independent life, stood up by my side when I desperately needed any sort of help personally or professionally, handled my mistakes with utmost wisdom and gave new ideas for my thesis. Most of all, I feel blessed to find him as an inspiration and an ideal to be followed through out the rest of my life.

Having several opportunities to work and discuss with Prof. Paul Hickson, I realized that there is no limit to the knowledge a person can hold. Without his expertise in building liquid mirror telescopes, it is difficult to imagine the success of the ILMT project.

I am grateful to my sibling Bharti, my parents Pitabasa & Lalita, my father figure Late Sachi uncle and to my friends Sudeep, Subrat, Satish and Shwetank who supported me on my unorthodox decisions to leave a corporate life and pursue the path leading to a PhD.

With a special mention to Anna, who has always pushed me to work hard with a lovely smile, care and kind words.

I also thank the members of the jury for accepting to evaluate my work: Prof. Jérôme Loicq, Prof. Serge Habraken, Dr. Peter De Cat, Prof. Philippe Dierickx, Dr. Christian Barbier, Dr. Tim Flohrer, Dr. Michaël De Becker and Prof. Jean Surdej.

Many thanks to Usman, Bonny, Carlos, Maddalena, Ludovic, Elsa, Aissa & Gilles to make me feel like home away from home. Thank you Sylvia and Nicole for saving me from all the mind blowing administrative tasks.

Dear Mridweeka, you inspired me to work hard and kept me positive during my tough times in Nainital as well as in Liège. I am also grateful to Kailash, Dheeraj and Hem at Devasthal to tolerate my never ending tantrums and keeping me out of stress at the end of every hectic day. I also thank Dr. Hum Chand, Hitesh, Himanshu, Khushal, the ARIES observing staff and technical assistants for their support with the ILMT construction.

A very special gratitude goes out to all down at Wallonie - Bruxelles International (WBI) (www.wbi.be) for funding this research.

Thesis abstract

The size and population distributions of space debris constitute an important input to risk analysis for current and future space missions. In preparation for future observations with the zenith-pointing 4-m International Liquid Mirror Telescope (ILMT), the 1.3-m Devasthal Fast Optical Telescope (DFOT) was used to gain experience with zenith-pointing observations and, serendipitously, to detect, identify and characterize orbital debris. An effective data reduction and calibration strategy was developed to treat raw CCD images recorded in the time-delay integration (TDI) mode. Thirteen debris streaks were detected visually, mostly during dawn and twilight. By modeling each of the debris as a diffuse-specular Lambertian sphere with an albedo ρ= 0.175, their effective diameters were estimated from the observed apparent magnitudes, altitudes, velocities and solar phase angles.

We also present an automatic detection technique to detect streaks invisible to human eyes by using the matched filtering technique. The Fourier space implementation of the matched filtering has been found to be computationally efficient. Monte Carlo simulations were performed to evaluate the efficiency of the proposed technique. After comparing with other existing streak detection techniques, the matched filtering in the Fourier space has been found to have better sensitivity in detecting fainter debris streaks.

An observation strategy in the TDI imaging mode has been proposed and demonstrated to obtain the information on the angular velocity or the altitude of the detected debris. This will provide an independent estimate of the orbital parameters and help in upgrading the existing catalogued information. It was found that debris in low-Earth orbits can be detected and characterized using the 4-m ILMT down to a size of 5 cm.

We also highlighted the construction work accomplished at the ARIES observatory (Devasthal, Uttarakhand, India) leading to the proper functioning of the ILMT observatory. We have been very actively participating in the installation of the various components related to the pneumatic and electronic systems, primary mirror stability, alignment of the rotation axis along the center of the prime focus and safety mechanism concerning the mercury handling.

Résumé

Les distributions en nombre et en taille des débris spatiaux constituent un élément important dans l'analyse des risques pour les missions spatiales actuelles et futures. En vue de prochaines observations au zénith avec le télescope à miroir liquide international de 4 m (ILMT), nous avons utilisé le télescope optique rapide de 1,3m (DFOT) situé à Devasthal en vue d'acquérir de l'expérience en matière d'observations pointées au zénith dans le but de détecter, identifier et caractériser les débris spatiaux. Une stratégie efficace de réduction et d'analyse des données a été mise au point pour traiter les images CCD brutes en mode d'intégration TDI (en anglais «Time-Delay Integration»). Treize traces de débris spatiaux ont été détectées visuellement, principalement à l'aube et au crépuscule. En modélisant chacun des débris au moyen d'une sphère lambertienne diffusante/spéculaire avec un albédo $\rho = 0.175$, leur diamètre effectif a été estimé à partir des magnitudes apparentes, altitudes, vitesses et angles de phase solaire.

Nous présentons également une technique de détection automatique permettant de détecter de faibles traces de débris spatiaux invisibles à l'œil nu sur les images CCD en utilisant la méthode de filtrage adapté. L'implémentation dans l'espace de Fourier de cette méthode s'est avérée très efficace en termes de puissance et de temps de calcul. Des simulations Monte Carlo ont été effectuées pour évaluer l'efficacitè de la technique proposée. Après comparaison avec d'autres techniques existantes de détection de traces de débris spatiaux, il s'est avéré que le filtrage adapté dans l'espace de Fourier présentait une bien meilleure sensibilité pour la détection de traînées de très faibles débris.

Une nouvelle stratégie d'observation en imagerie TDI a été proposée et testée pour obtenir des informations sur la vitesse angulaire ou l'altitude des débris détectés. Cela fournira une estimation indépendante des paramètres d'orbite et facilitera la mise à niveau des informations cataloguées existantes. Nous avons estimé que les débris en orbites basses et moyennes pourront être détectés et caractérisés à l'aide de l'ILMT de 4 m jusqu'à une taille d'environ 5 cm.

Nous présentons également les travaux de construction réalisés à l'Observatoire ARIES (Devasthal, Uttarakhand, Inde) qui vont permettre la prochaine mise en opération du télescope à miroir liquide de 4m, le ILMT. Nous avons participé très activement à l'installation des divers composants liés aux systèmes pneumatiques et électroniques, à la stabilité du miroir primaire, à l'alignement de l'axe de rotation passant par le centre du foyer principal du télescope et au mécanisme de sécurité concernant la manipulation du mercure.

Contents

1 Introduction

1.1 Space situational awareness

Orbital debris present at altitudes ranging from low-Earth orbits (LEO - an altitude of 2000 km or less) to geosynchronous orbits (GEO) consists primarily of expired spacecraft, rocket stages, separation devices and products of collision or breakup of satellites (Chobotov et al., 1997). Debris in the Earth-space environment poses a threat to the survivability of resident satellites and future space missions (Schaub et al., 2015; Zhang et al., 2017). In addition, several accidents and intentional anti-satellite weapon tests fuel the threat to a higher level by decreasing the lifetime of a functional satellite (Wright, 2007; Black and Butt, 2010). Simulations have also predicted that even if no more spacecraft is launched, the risk will keep on increasing due to collision cascade effect ('Kessler Syndrome', Kessler and Cour-Palais, 1978) and increase in debris population (Liou and Johnson, 2006). The debris not only affects active satellites but also constantly threatens manned spacecraft such as the International Space Station (ISS) (Johnson and Klinkrad, 2009). The only natural mechanism for debris removal is atmospheric drag, which is relatively slow even for objects in LEO. If enough warning is provided, the spacecraft can maneuver to avoid collisions with debris. But for this to be effective, a real time updated database of all space debris should be produced.

Ground-based observations employ radar or reflected sunlight to detect and track orbiting objects (Mehrholz et al., 2002; Lederer et al., 2016). The orbital radius, and distance from the observer can then be determined from the observed position, angular rate, and time of observation. Figure 1.1

shows the sample of objects estimated in LEO by various types of measurements. It can been noticed that the majority of the population has been observed by means of radar surveillance technology and there a lack of optical observations for fainter or smaller size population. The sensitivity of radar measurements falls proportionally to the distance to the fourth power of the target object, but in case of optical measurements the sensitivity reduces proportional to the distance squared. Another advantage of the optical telescopes are their better pointing accuracy and angular resolution than the radar ones. These are the main advantages of the optical telescopes over the radar antennas which encourage in constructing an independent and complementary catalogue to the radar ones. Most debris objects have near-circular orbits (Xu and Xiong, 2013). In an optical observation, these parameters can be determined from the length of the streak that the objects leave on timed exposures, or angular distance traveled if they appear in two or more sequential exposures. The orientation of the streak provides information on the inclination of the orbit. If one assumes an albedo and phase function, the size is readily estimated (Mulrooney and Matney, 2007, 2008). Identification of the detected objects can be achieved by matching the derived ephemeris and direction of the streak with predicted values for cataloged objects.

Till now several optical survey results have been published, such as 1) measurements at LEO from the 3-m NASA Liquid Mirror Telescope (LMT, Africano et al., 1999) and measurements at higher orbits like, Medium Earth Orbits (MEO) or GEO belt using 2) NASA CCD Debris Telescope (CDT, Barker et al., 2005), 3) Michigan Orbital DEbris Survey Telescope (MODEST, Abercromby et al., 2010), 4) Transitoires - Rapid Action Telescope for Transient Objects network of telescopes (TATROT, Boër et al., 2017), 5) ESA's Space Debris Telescope (ESASDT, Hinze et al., 2013), etc. Despite all these surveys, a meagre information on the optical characteristics and statistics is not enough to represent a significant sample of the debris population. As the population of space debris is increasing steadily (see Figure 1.2) and smaller or fainter space debris are exceedingly more numerous than larger ones (Portee and Loftus, 1999), more such surveys are required particularly focusing on the small debris population, which is until this date sparsely cataloged.

1.2 The ILMT project

A new facility, the 4m International Liquid Mirror Telescope (ILMT) (Jean et al., 1999; Surdej et al., 2006, 2018) is expected to achieve first light in early 2020 at Devasthal (India), with the joint efforts from the scientific and engineering communities of several institutions [1]. While its primary purpose

[1]Space sciences, Technologies and Astrophysics Research (STAR) Institute of Liège University, the Royal Observatory of Belgium (ROB), University of British Columbia

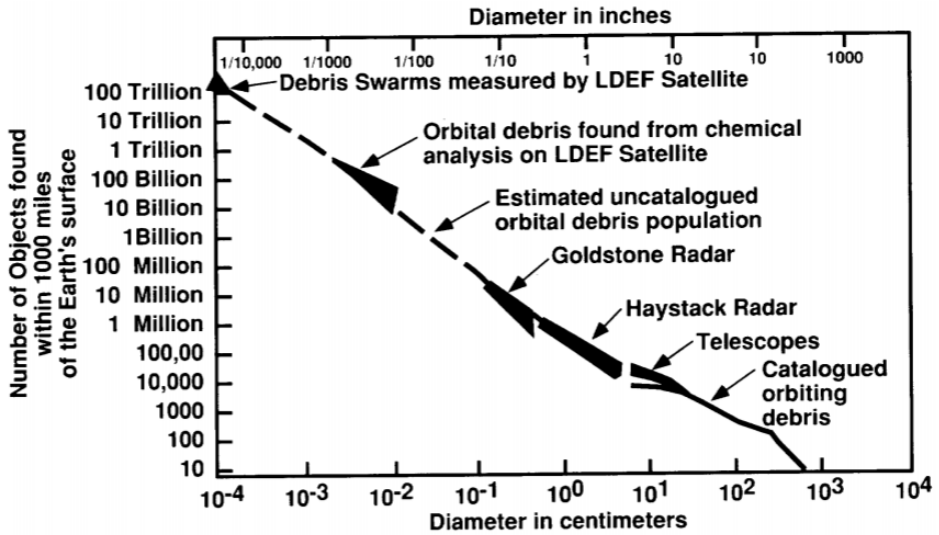

Figure 1.1: Object size distribution in LEO. Source: Portree and Loftus Jr, 1999

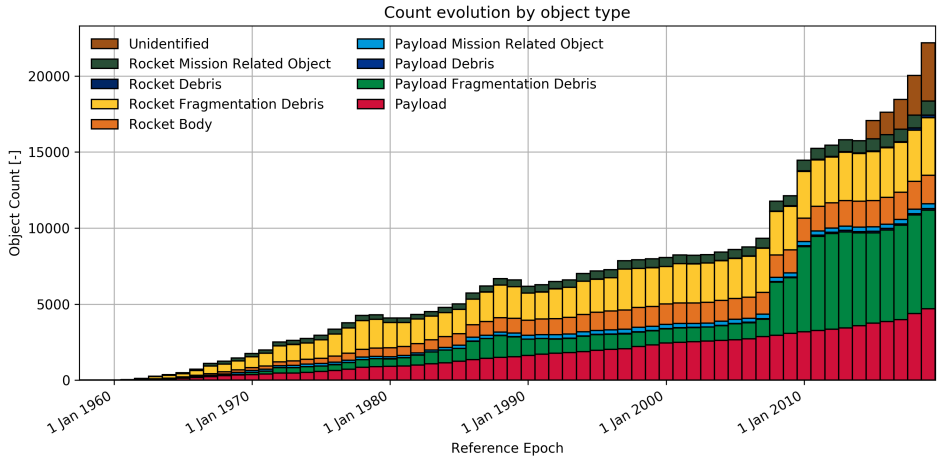

Figure 1.2: Evolution in the space debris population. Source: https://www.esa.int/Our_Activities/Space_Safety/Space_Debris/About_space_debris

is to conduct astronomical surveys, the data that will be obtained will have many uses, including the detection and characterization of space debris.

(UBC, Canada), Université Laval (Canada), University of Montreal (Canada), University of Toronto (Canada), York University (Canada), University of Victoria (Canada), Aryabhatta Research Institute of Observational Science (ARIES, India) and the Observatory of Poznań (UAM, Poland)

1.2.1 Working principle

Borra et al. (1985, 1992) have first suggested to use a CCD in the TDI mode sky observations with liquid mirrors. The fundamental working principle of this telescope is to make use of a rotating liquid (Mercury) surface which takes the shape of a paraboloid and record the patch of the sky that passes overhead (Borra et al., 1985). The telescope set up primarily comprises a 4-m diameter bowl containing liquid Mercury, a rotation table to spin the bowl and a system of corrector lens along with a cryo-cooled CCD camera employing time-delay-integration readout (TDI) at the prime focus (see Figure 1.3).

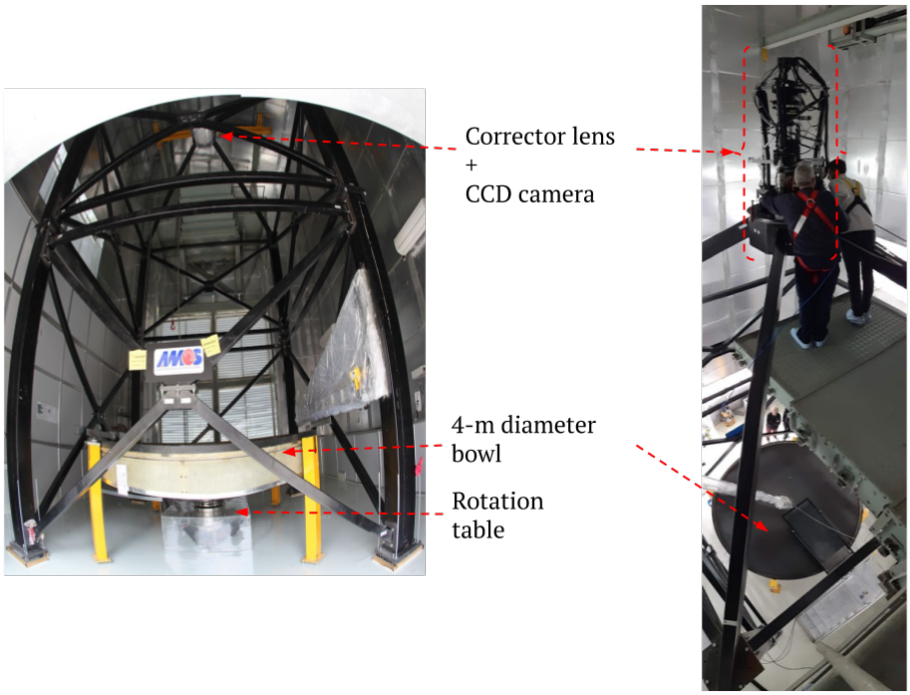

Figure 1.3: The image on the left is a front fish-eye view and the image on the right is a corner panoramic view of the 4-m ILMT.

Figure 1.4 shows a basic schematic of the liquid mirror telescope. The rotating liquid Hg experiences accelerations due to the centrifugal force along the radial direction ($\hat{r}$) and the local gravity downwards ($-\hat{z}$, see Figure 1.4). Hence at the equilibrium, the liquid surface settles perpendicularly to the net acceleration. If the angle between the tangent over the liquid surface and the horizontal plane is ζ, then

$$\tan(\zeta) = \frac{dz}{dr} = \frac{\Omega^2 r}{g}, \tag{1.1}$$

where Ω is the angular velocity of the primary mirror, r is the radial distance of the liquid surface from the axis of rotation and g is the local gravitational acceleration. By integrating Eq. 1.1 along the axis of rotation and along the radial direction,

$$\begin{aligned} \int_0^z dz' &= \int_0^r \frac{\Omega^2 r'}{g} dr', \\ z &= \frac{\Omega^2 r^2}{2g}. \end{aligned} \tag{1.2}$$

The expression derived above can be compared to the standard equation of a parabola with a focal length F and the axis of parabola being -$\hat{z}$, i.e.,

$$z = \frac{r^2}{4F}. \tag{1.3}$$

Hence, the focal length of the telescope takes the expression

$$F = \frac{g}{2\Omega^2}. \tag{1.4}$$

The focal length of the ILMT is set at 8 meters that can be achieved by rotating the liquid mirror surface with $\sim$ 7.5 revolutions per minute. To achieve a surface quality for astronomical observation, a pressurized air-bearing is used at the rotation table which restricts a significant amount of vibration being transferred to the liquid mirror surface and thereby avoids wavelets formation. As a conventional parabolic mirror, the liquid mirror also induces coma aberration and astigmatism at the focal plane (to know the details about these effects see Schroeder, 1999). In addition to these, TDI observation induces optical distortion also known as 'TDI distortion' (Hickson et al., 1993; Hickson and Richardson, 1998a; Vangeyte et al., 2002). In order to correct for these effects, a complex corrector lens setup is placed before the CCD camera to correct for a field of view of 27 by 27 arcminutes.

1.2.2 Scientific applications

Several scientific possibilities have been discussed by Borra (1995, 1997). Observing and recording 27' wide patch of the sky at the zenith centered at a constant declination (= the latitude of the telescope, 29.3617°N), the ILMT will cover a total of $\sim$141.2 square degrees sky field. Approximately half of the sky coverage falls under the high Galactic latitude ($|b| \geq 30°$) which facilitates the detection of fainter and distant objects such as quasars, galaxies and supernovae, whereas in the low galactic latitudes predominant milky way stars will be visible. Hence, various research works concerning galactic as well as extra-galactic astrophysics can be accomplished. The initial running phase for the ILMT project is 5 years. Repeatedly observing

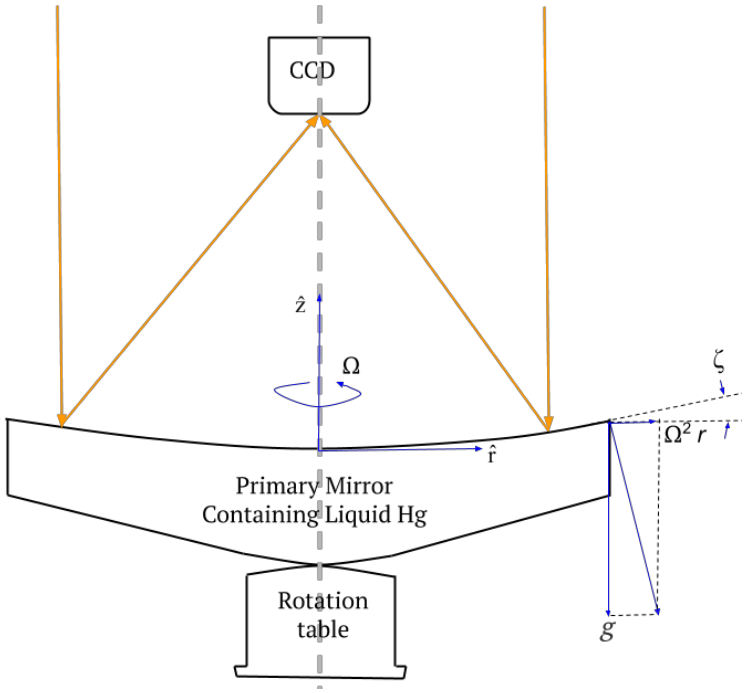

Figure 1.4: Basic schematic of a liquid mirror telescope.

the same part of the sky night after night will not only give access to fainter magnitude objects but also make inter-day as well as inter-year transient studies possible. A brief description of a few scientific cases are as follows:

- Statistical estimation of the cosmological parameters H_o, Ω_M, Ω_Λ based on the Supernova type Ia studies or the gravitational lens studies among multiply imaged quasars.
- Study of faint galaxies by co-adding images of equal field of view from multiple nights.
- Photometric variability study of RR Lyrae stars, Novae, transiting exo-planets and other transient events.
- Photometric follow up of supernova remnants, active galactic nuclei, etc.
- Estimation of the trigonometric parallax of nearby objects such as red, white and brown dwarfs, milky way's halo stars.
- Detection of high proper motion stellar objects
- Astrometry of multiple star systems

2

TDI OBSERVATIONS

The imaging technique termed "Time-Delay Integration (TDI)" or, "Drift Scanning" is a special method of directly imaging celestial objects. While the telescope is in the non tracking mode, the TDI implementation on a CCD detector makes the photoelectrons being transferred from one CCD row to the next one such that the image of the moving celestial objects comes out sharp without image blurring. The necessary conditions to obtain such images are the proper alignment of the CCD camera and the correct photoelectron transfer rate. The CCD columns should be parallel to the linear motion of the objects (see Figure 2.1) and the charge transfer rate should be synchronized with the speed of the moving objects. Operating a CCD camera in the TDI mode has been a usual practice in many digital sky surveying telescopes since more than three decades (McGraw et al., 1980; Wright and Mackay, 1981; Gehrels et al., 1986; Gunn et al., 1998, 2006; Zaritsky et al., 1996; Gorjian et al., 1997; Baltay et al., 2002; Hickson et al., 2007; Gaia Collaboration et al., 2016a,b).

This whole setup provides the advantage of always working under the best seeing conditions as it encounters the least air-mass (Z=1). Transparency at the zenith is also naturally the best. Scanning the same part of the sky repeatedly by the fixed telescope also enables one to access fainter sources by co-adding CCD frames of the same field and to detect variable or moving objects by subtraction of a reference CCD frame from those acquired on different nights (cf. Section 3.5).

In preparation for the ILMT survey, we have obtained and analyzed several nights of data using a conventional optical telescope pointed towards the zenith and equipped with a CCD image sensor operating in TDI mode. The telescope employed was the 1.3-m Devasthal Fast Optical Telescope

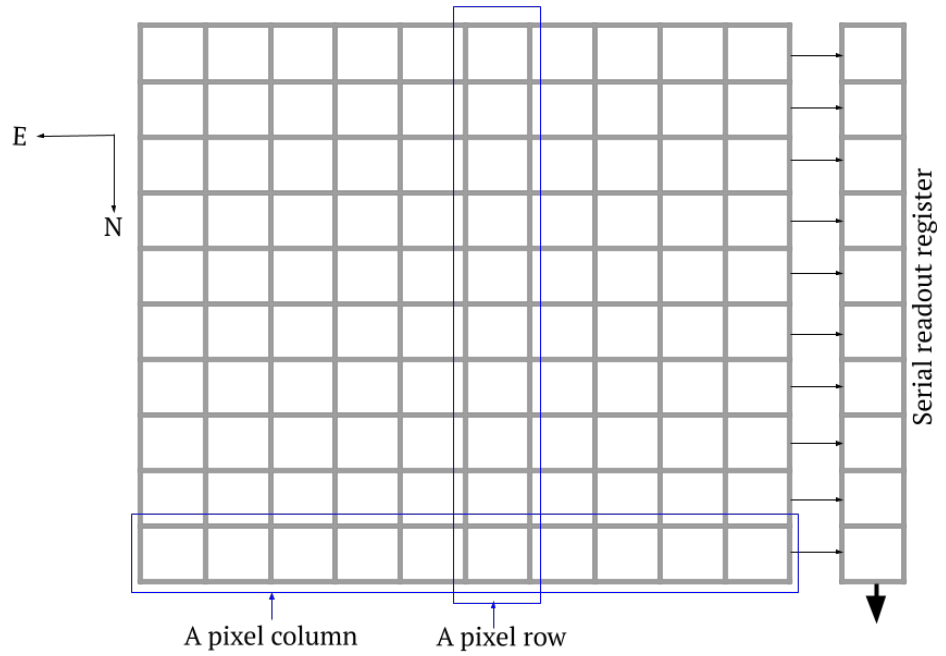

Figure 2.1: Schematic of a properly oriented CCD camera chip for TDI operation.

(DFOT) of ARIES, Uttarakhand, India (Sagar et al., 2013). It is located adjacent to the ILMT, at N29°21′42″ E79°41′06″ and 2410-m altitude, and therefore experiences very similar observing conditions. In the following sections we describe our data analysis techniques and present the results for the detected objects.

2.1 1.3-m DFOT observations

Observations were conducted by parking the telescope near the zenith and implementing the TDI mode, also known as drift-scanning to compensate for the Earth's rotation (McGraw et al., 1980; Wright and Mackay, 1981). This is the observing mode that will be used for the ILMT. The detector used was an SBIG 2K × 2K CCD camera, having a field of view of 10.1 × 10.1 arcmin and an image scale of 0.295 arcsec per pixel. The gain of the CCD was 0.59 e^-/ADU and its readout noise was approximately 25 e^-. Initially the CCD camera was placed at the Cassegrain focus of the telescope. Then several TDI frames were taken with an arbitrary TDI rate. If the scanning direction of the CCD columns is not properly oriented along the East-West direction and that the readout rate is not the same as the sidereal rate, then the celestial sources detected on the CCD frame will appear as elongated

trails inclined with respect to the CCD rows. It is then necessary to bring the trails parallel to the CCD rows (see Figure 2.2) by adjusting the readout rate to match the angular velocity of the objects passing up above. At this point the orientation of the CCD is still not tuned. To do so, while changing the azimuthal orientation of the CCD, we took several long exposures in the classical mode of observation (i.e., not using the TDI mode) and made sure that the long trails observed for the stars were getting perfectly parallel to the columns of the CCD (see Figure 2.3).

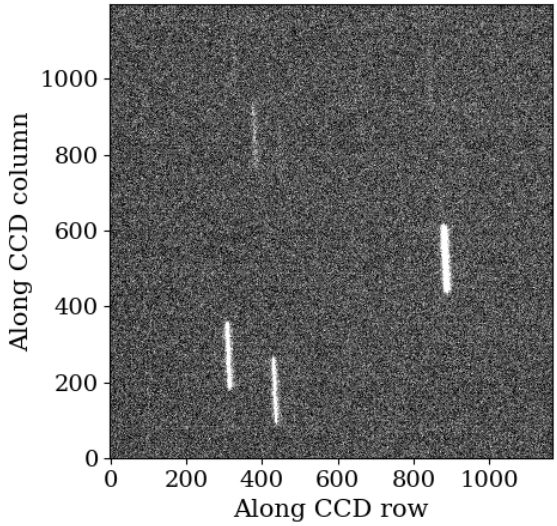

Figure 2.2: This picture illustrates a part of a CCD frame obtained with DFOT pointing towards the zenith while the CCD camera operating in the TDI mode was not properly aligned along the East-West direction. If the TDI rate would perfectly match the angular velocity of the stars passing over the focal plane, the star trails would appear vertical, i.e., perfectly aligned with the CCD rows. We see that the stellar trails are slightly inclined due to a non accurate choice of the TDI rate.

Three filters were set in the camera, matching the g′, r′ and i′ wavelength bands of the Sloan Digital Sky Survey (SDSS) (Gunn et al., 1998). One of these filters was inserted at the beginning of each night and used for the entire night. The median seeing (FWHM) was found to be 1.1 arcsec. In the TDI mode, the CCD is read continuously. The effective integration time for the celestial objects is the time required for their images to drift across the full length of the CCD, which in our case was 46.1 seconds. In practice, the length of the acquired CCD frames was limited by the memory available to the data acquisition system. As a result, each recorded frame has a dimension of 27952 × 2048 pixels, corresponding to a 2.29° × 10.1′

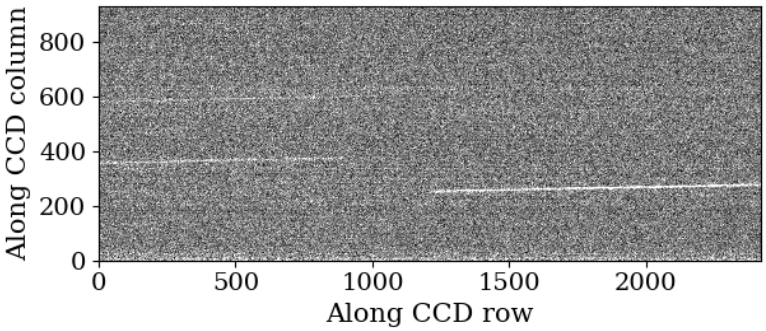

Figure 2.3: Portion of a CCD frame obtained in the classical mode of observation (i.e., without TDI). The long star trails indicate that the CCD camera needs to be better oriented along the East-West direction, i.e. be set exactly parallel to the CCD columns.

field of view. The temperature of the CCD was maintained close to -27° C by means of a Peltier cooling system. Observations were made during 11 nights in May, 2015 (see Table 2.1). However, approximately 60% of the observing time was lost due to bad weather (pre-monsoon season). Of course, orbital debris can be detected optically only when illuminated by the Sun. Particularly, LEO objects can be observed only within a few hours from sunset and sunrise.

2.2 Data reduction

Like any other raw CCD image, TDI data are also affected by well known noise phenomena such as photon noise, dark noise, readout noise and non-uniform response of each pixels. However, TDI data present some unique aspects compared to images obtained in the classical mode of observation (without TDI). Each row of the image is read out at a different time, so any temporal variations in CCD temperature will result in a systematic variation of dark current along the scan direction (right ascension). Similarly, changes in sky brightness will produce background variations in the images.

In our case, a varying gradient in dark current was observed, primarily along the orthogonal (declination) direction. This was removed by subtracting a 1-dimensional mean dark (see Figure 2.4) from each row of the subsequent CCD frames. This mean dark was computed by taking the mean of all rows in several dark frames, using a one-time rejection of outliers that differ by more than 1.5 standard deviations and subsequently fitting a second order polynomial.

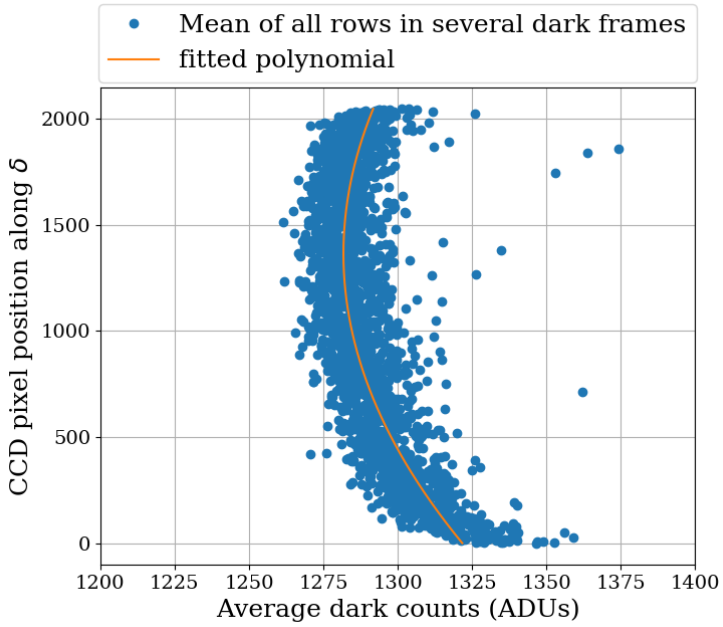

Figure 2.4: Profile of a 1-dimensional mean dark showing a varying gradient of the pixel counts (in ADU) along the declination direction. ADU stands for Analog-to-Digital Unit which in fact is the digital counts present in the CCD pixels.

The pixel-to-pixel variation in the sensitivity of the CCD camera is called flat-field effect which makes the brightness output of each pixel slightly different from each other while being uniformly illuminated. This effect can be removed from the astronomical images in order to be capable of detecting very faint objects. The usual practice to obtain a flat-field image is by illuminating the CCD camera with a uniform light source such as the twilight sky or a dome flat. However, it is difficult to obtain a uniform illumination from these procedures. Such a flat-field also contains information on optical non uniformity due to vignetting, interferences and dust particles deposited on some of the camera lenses. So the flat field frames must be taken without moving or changing anything on the telescope setup.

In TDI images, the output signal is proportional to the sum of the charges generated by the individual pixels in the scan direction. Effectively, the detector response function is averaged along the scan direction. The result is a very uniform response that varies only along the orthogonal (declination) direction. These small residual sensitivity variations have been corrected for by creating a normalized 1-dimensional flat-field from the background sky light. Another big advantage of taking the sky background for the flat-field is that its spectrum is the same as that which dominates the integrated flux of very faint objects. While steadily observing the darkest part of the sky (i.e. at the zenith) and subsequently obtaining the pixel response for each individual CCD frame that varies only in one direction is the most efficient flat-field that can be achieved. Its signal-to-noise ratio turns out to be much higher. After dark subtraction, the average of the pixel values was taken along the scan direction using 1.5-σ outlier rejection. The resulting 1-dimensional sensitivity map was normalized and then applied to (divided into) every row in the science images. An example of such a normalized 1-dimensional pixel response is shown in Figure 2.5.

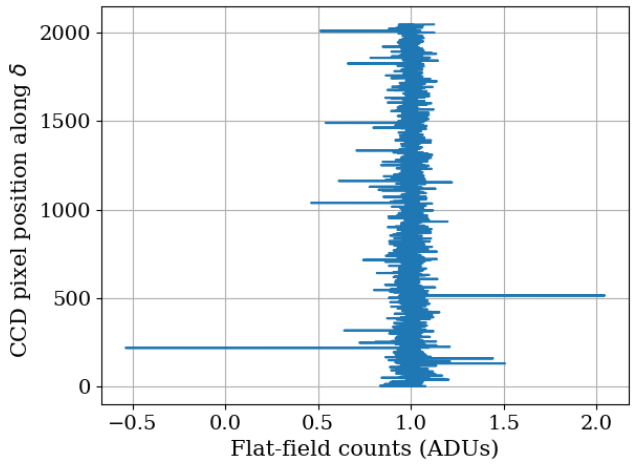

Figure 2.5: 1-dimensional normalized flat-field pixel response along the declination direction.

An independent measurement of the CCD gain was also done in order to better establish the relationship between the number of electrons recorded by the CCD and the digital counts generated. To perform this, we used an equation which relates the electron quantities, which are unknown, to the values that we measure from the CCD in counts or ADUs. We can relate the signal and its associated noise via the gain factor g as,

$$f_e = g\ f_c \text{ and } \sigma_e = g\ \sigma_c, \tag{2.1}$$

where f_c and f_e represent the flux levels expressed in terms of counts recorded in the CCD and electrons produced by the CCD, respectively. Similarly σ_c and σ_e are the one-sigma noise levels associated with the CCD measurements in terms of digital counts and electrons, respectively. The dark noise subtracted and flat-field corrected images remain affected by the photon noise (σ_{phot_e} in e^-) and readout noise (σ_{RON_e} in e^-). Both these noise terms are independent of each other and hence add up in quadrature. So the total noise counts present in the CCD frames can be written as,

$$\sigma_e^2 = \sigma_{phot_e}^2 + \sigma_{RON_e}^2 \tag{2.2}$$

The photon noise follows a Poisson distribution, so $\sigma_{phot_e}^2$ can be approximated by f_e. Adopting this relation in the above equation we get,

$$\begin{aligned} \sigma_e^2 &= f_e + \sigma_{RON_e}^2, \text{or} \\ \sigma_c^2 &= \frac{1}{g}\ f_c + \sigma_{RON_c}^2. \end{aligned} \tag{2.3}$$

Of course $\sigma_{RON_c}^2$ is the readout noise in terms of digital counts. The expression above represents a simple straight line equation (σ_c^2 versus f_c) which slope inverse corresponds to the CCD gain value. If we measure the total counts and the corresponding variance from different regions of a long strip TDI image, we may able to derive the value of the CCD gain appearing in Eq. 2.3. But the selected regions may show a flux gradient due to the change in sky brightness and it may inflate the measured variance. As a result, the gain measurement will not be accurate. In a TDI image each row is read at a different time instance. If we consider that the background brightness of the CCD image does not change significantly over a few rows, then the constituting region can be considered as uniformly illuminated and ready to be used in the signal-variance analysis. But if we again split this region into two sub-regions and take their ratio, then any noise due to pixel-to-pixel variation in the sensitivity can be normalized.

Let us assume the two regions of nearly equal surface brightness to have the flux levels f_{c1}, f_{c2} with standard deviations σ_{c1} and σ_{c2}, respectively. The variance of the ratio of these two regions will be mathematically represented by,

$$\begin{aligned} \text{Var}\left[\frac{f_{c1}}{f_{c2}}\right] &= f_{c_1}^2 \text{Var}\left[\frac{1}{f_{c2}}\right] + \frac{1}{f_{c_2}^2}\text{Var}[f_{c1}], \\ \text{in which Var}[f_{c1}] &= \sigma_{c_1}^2 \\ \text{and Var}\left[\frac{1}{f_{c2}}\right] &= \frac{\sigma_{c_2}^2}{f_{c_2}^4}. \end{aligned} \tag{2.4}$$

Assuming the same flux and noise levels in both regions under consideration, we may write

$$f_{c_1} = f_{c_2} = f_c \text{ and } \sigma^2_{c_1} + \sigma^2_{c_2} = 2\sigma^2_c \tag{2.5}$$

where f_c and σ^2_c are the common flux level and variance, respectively. So Equation 2.4 can be re-written as,

$$\text{Var}\left[\frac{f_{c1}}{f_{c2}}\right] = \frac{2\sigma^2_c}{f^2_c}.$$

Replacing σ^2_c from Equation 2.3 and rearranging the terms gives,

$$\frac{f^2_c}{2}\text{Var}\left[\frac{f_{c1}}{f_{c2}}\right] = \frac{f_c}{g} + \sigma^2_{RON_c} \tag{2.6}$$

We have plotted $\frac{f^2_c}{2}\text{Var}\left[\frac{f_{c1}}{f_{c2}}\right]$ Vs f_c from one of our TDI frames considering sub-regions of shape 100×100 pixels (see Figure 2.6). A straight line fit to these data points enables one to derive the gain of the CCD as 0.59±0.01 e^-s/ADU.

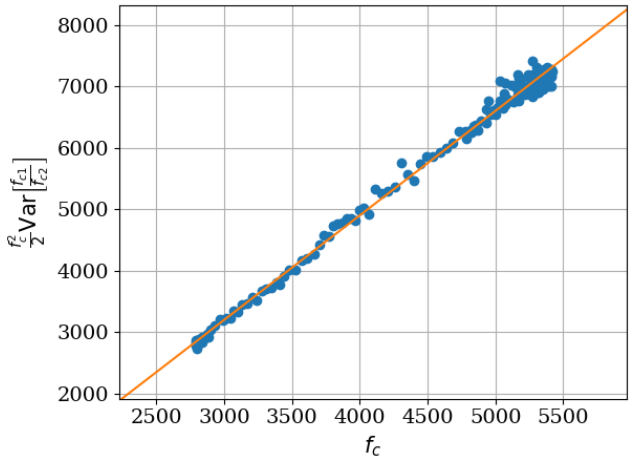

Figure 2.6: CCD gain and readout noise measurement. This measurement is for a single TDI frame obtained on 15 May 2015 at 10:49:01 UTC using the SDSS i' filter.

The presence of moon, clouds or twilight largely contributes to the sky background. Sky subtraction was performed by fitting each image, after dark and flat-field correction, with a smooth two-dimensional polynomial, using outlier rejection to remove the stars. This polynomial was then subtracted in order to remove the sky. A second order polynomial was found to be sufficient to fit the sky background in most of the acquired frames. But

the frames obtained close to sunrise or sunset showed a stiff gradient in their background counts (see Figure 2.7). So, in that case, a higher order polynomial was used to fit the background level. The effectiveness of these preprocessing steps is illustrated in Figure 2.8.

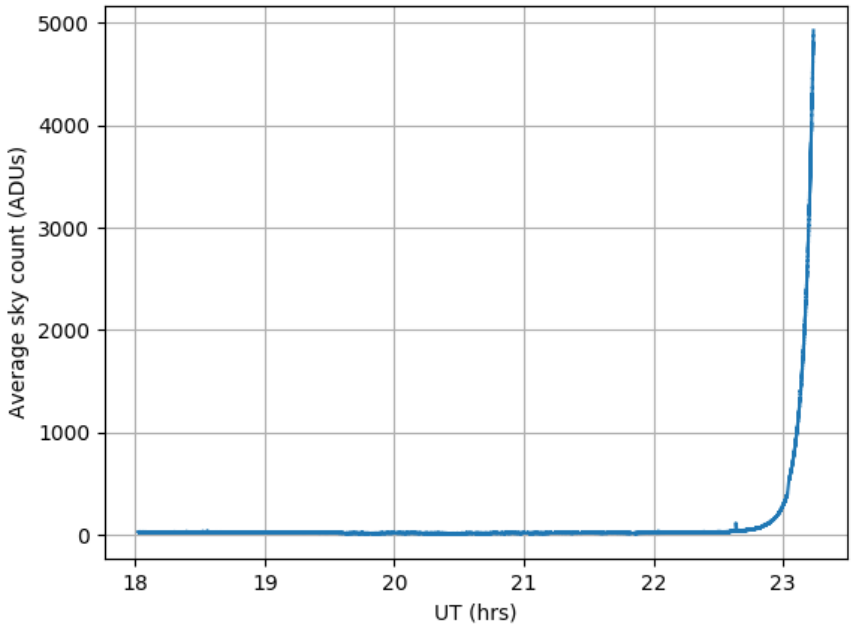

Figure 2.7: Average sky counts along each CCD row recorded through out the night of 16 May 2019. A stiff increase in the average sky counts after 22h 45m (local time = 5h 15m) can be seen at the beginning of sunrise.

2.2.1 Astrometric and Photometric calibration

The Sextractor algorithm (Bertin and Arnouts, 1996) was used to build a catalog of objects present on each individual preprocessed image. A threshold intensity of 1.5-σ above the local background, determined from the median of a 64×64-pixel surrounding region, was applied to isolate connected groups of pixels (objects). A minimum object area of 10 pixels was considered. For each detected object, the centroid was computed by modelling it with a Gaussian ellipsoidal intensity distribution. This resulted in instrumental magnitudes and centroid positions for all detected objects.

Calibrated magnitudes of the detected sources were obtained by matching detected stellar objects with stars in the Gaia Data Release 1 catalog (Gaia Collaboration et al., 2016a,b). As the observations were made towards the

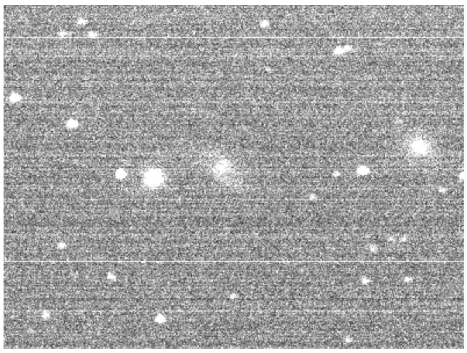

(a)

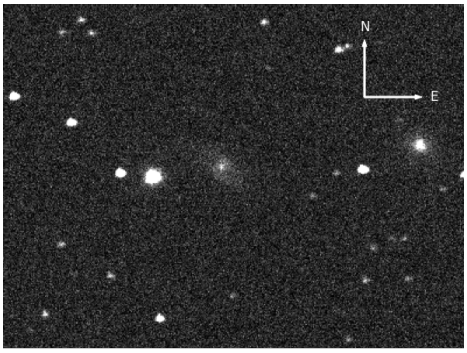

(b)

Figure 2.8: Comparison of a subimage before (2.8a) and after preprocessing (2.8b). An area of $3.5' \times 4'$, centered at $18^h02^m{+}29°$ (J2000.0), is shown. The image was taken on 24 May 2015 at 20:34:46 UTC, using the SDSS g′ filter.

zenith, the atmospheric extinction was minimum. So, the published Gaia magnitudes (m_G) were used directly to estimate the zero-point offset between the calibrated magnitudes and our instrumental magnitudes. Figure 2.9 shows the linear relationship between the instrumental magnitude (m_{inst}) and the corresponding Gaia magnitude scale.

In the TDI observing mode, while the scanning direction is along the right ascension, the CCD columns and rows correspond to different right ascension and declination, respectively. This makes the astrometric calibration straightforward. Mathematically,

$$\begin{aligned} x &= c1\ ra_{\mathrm{J2015.4}} + c2, \\ y &= c3\ \delta_{\mathrm{J2015.4}} + c4, \end{aligned} \tag{2.7}$$

where x and y are pixel positions along CCD rows and columns, respectively, $ra_{\mathrm{J2015.4}}$ and $\delta_{\mathrm{J2015.4}}$ are the right ascension and declination at the epoch of observation , and $c1, c2, c3,$ and $c4$ are the coefficients of the linear equations.

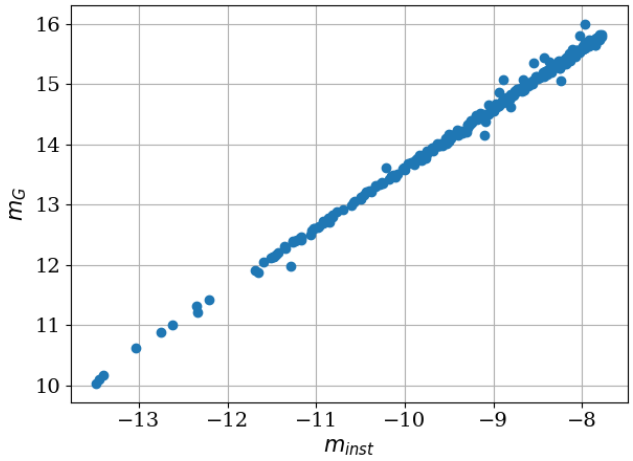

Figure 2.9: Linear relationship between the instrumental magnitude (m_{inst}) and the corresponding Gaia magnitude scale. This measurement is for a single TDI frame obtained on 19 May 2015 at 21:04:17 UTC using the SDSS g' filter.

The calibration was performed by applying corrections for nutation and aberration to the instrumental positions, and then precessing the resulting coordinates to a standard epoch, J2000. These were then compared to the corresponding Gaia positions. Coefficients of a bilinear transformation between instrumental and calibrated positions were determined by minimizing the squared residuals for the matched stars. To improve the calibration in both photometry and astrometry, very faint objects having $m_G > 17$ were excluded. Depending on the galactic latitude of the fields, one to two hundred stars typically were available for the calibration of each image.

The resulting RMS astrometric precision was found to be 0.1 arcsec in declination and 0.15 arcsec in right ascension, as seen in Figures 2.10 and 2.11. The RMS photometric precision is 0.04 magnitude (refer to Figure 2.12). This degree of photometric error is not unexpected due to the differences between the SDSS spectral bands and the broad-spectrum Gaia response.

2.3 Data analysis

2.3.1 Visual detection of space debris

Thirteen linear debris streaks were visually identified in the processed images. These are illustrated in Figure 2.13. To determine the position and flux of each, a line was fit connecting the endpoints of the streak. For each column,

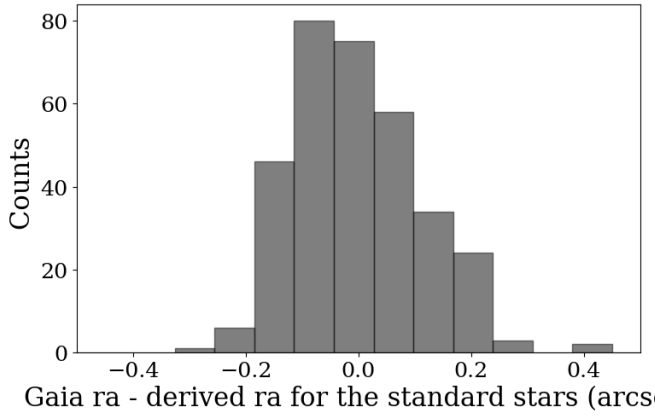

Figure 2.10: Histogram of the residuals in right ascension after astrometric calibration with stars from the Gaia catalog. This is for a single field image, obtained on 19 May 2015 at 21:04:17 UTC, within the ra range of $18^h12^m - 18^h23^m$ (2015.4 epoch) using the SDSS g′ filter.

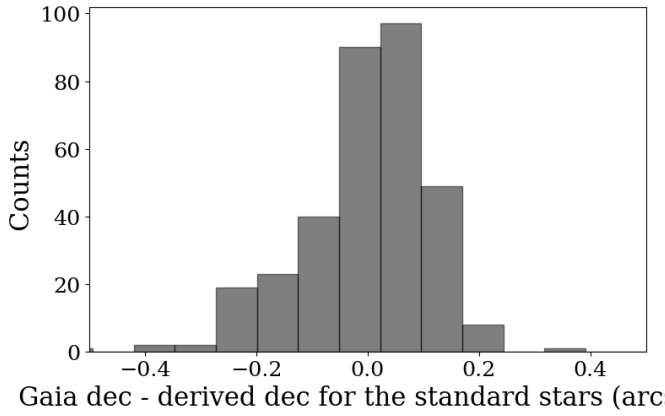

Figure 2.11: Histogram of the residuals in declination after astrometric calibration with stars from the Gaia catalog. This is for a single field image, obtained on 19 May 2015 at 21:04:17 UTC, in the ra range of $18^h12^m - 18^h23^m$ (2015.4 epoch) using the SDSS g′ filter.

pixels within a distance of ±4 times the stellar FWHM of this line were used to generate a profile, with 0.1-pixel resolution, by cubic spline interpolation. The profiles for each column were then shifted and co-added, using cross correlation to determine the required shifts. This resulted in a low-noise composite profile of the line in the scan (ra) direction. This profile was then fit to each individual column of data, using least squares analysis to determine the best amplitude and shift. The uncertainty in estimating the positions of bright streaks on the CCD images was found to be less than a pixel, whereas in fainter streaks the uncertainty increased up to 10 pixels.

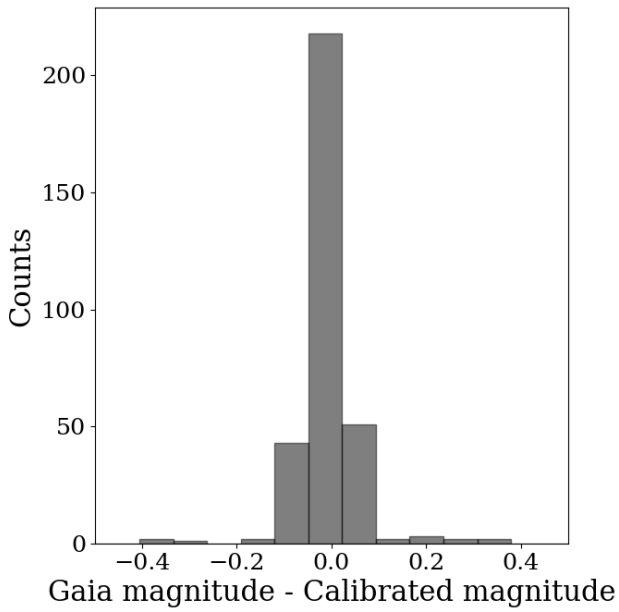

Figure 2.12: Histogram of the residuals obtained after subtracting the Gaia magnitudes of the detected standard sources from those derived in the present work. This is the result obtained after calibrating a single data block, obtained on 19 May 2015 at 21:04:17 UTC, in the ra range of $18^h12^m - 18^h23^m$ (2015.4 epoch) using the g′ SDSS filter.

The fitted profile was then integrated to estimate the total flux in the streak for each column of the image. From this, a one-to-one relationship between flux and position along the streak was obtained. For some objects, this was converted to a light curve (flux vs time) using the angular rate predicted for the object based on its identification (described below).

Some objects showed quasi-periodic photometric variations (e.g. Figure 2.14) in their light curves (e.g. object 6 in Figure 2.13). This is very likely due to the object rotating very fast, causing sunlight to be reflected in a recurrent manner. By analyzing such light variations, one could set interesting constraints on the shape of the object. But such an analysis is beyond the goals of this thesis.

The direction of each object, i.e., the angle ϕ subtended by the streak from North towards East was measured from the images. Although the telescope is not tracking and the Earth is rotating, the TDI scan removes this rotation, so the direction measured on a TDI image is the actual direction of the object in the International Celestial Reference System (ICRS) inertial frame.

With TDI observations, the time at which the object crosses the detector is generally uncertain, because the exact position at which it crossed the CCD

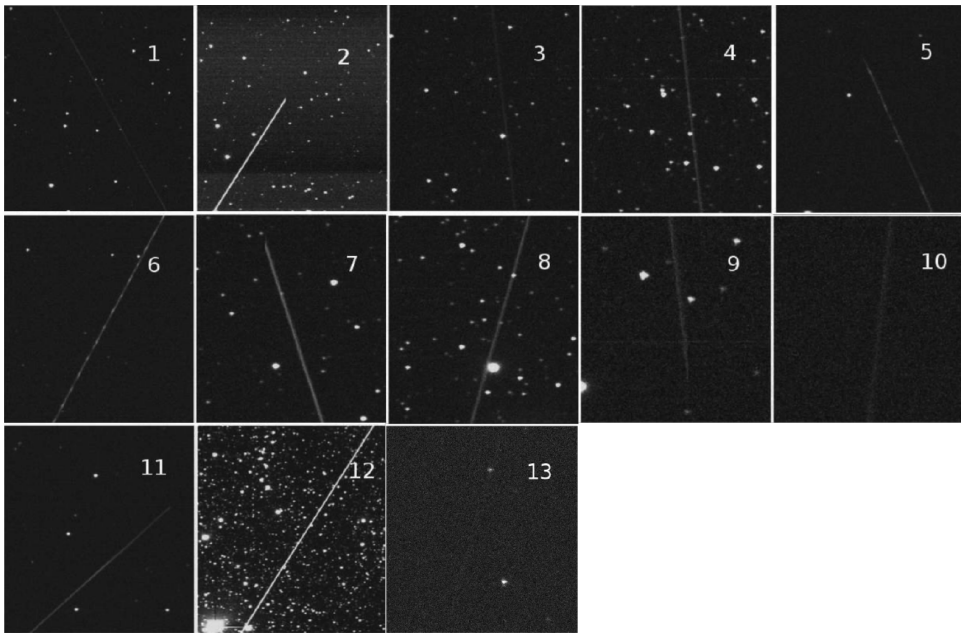

Figure 2.13: Images of the 12 detected objects passing through the CCD field of view. Images 2 and 12 show the same object, detected on two different nights. All the images of the collage are cropped for a better visualization.

is not known. For our observations, images of celestial objects move across the CCD in ∼46 seconds, which is the time required to move charges from one side of the CCD to the other. So the time of detection of a moving object is uncertain by as much as 23 seconds, depending on where it crossed the detector. An exception to this occurs if the object enters or leaves the CCD at an edge that is perpendicular to the scan direction. In that case, the streak ends abruptly, as can be seen for objects 2, 5, 7, 9 and 11 in Figure 2.13. From the direction of the streak and making use of the two line element (TLE) (see below), one can determine whether the object entered or exited at the edge where the charges are read out. Thus the time of entry or exit is known within the precision of the read-out time of the corresponding CCD pixel row. The precision was found to be ±1 second considering the accuracy of the synchronization between the computer's clock and its online time source.

A set of python programs was used to correlate the observed streaks with cataloged objects having their TLEs generated on the same observing date available from the U.S. Air Force Space Command [Space-Track.org]. Each TLE was propagated using the SGP4/SDP4 algorithm (Hoots and Roehrich, 1980; Vallado et al., 2006) and used to predict topocentric positions of the objects as seen from the DFOT observatory, as well as their altitude, angular velocity and direction. Objects predicted to pass through the field of view

of the telescope during the observing period, while at the same time being illuminated by the Sun, were selected. By comparing the observed time and direction of the streak with those predicted from the TLE database, all of the 13 detections were identified. The predicted and observed parameters for these objects are listed in Table 2.2.

One object (SSN 24827; objects 2 and 12 in Figure 2.13) was detected on two different nights. According to the TLE information, its angular velocity was 507.0″/sec. By considering that the average time taken by the object to complete a revolution around the earth is constant, there were 101 revolutions between the consecutive appearances of this object in our TDI observations. Given the number of revolutions and the time interval between the consecutive appearances of the object, we have found that the resulting angular velocity to be 508.67±0.02″/sec. This method could be a possible application of the TDI observation to upgrade the orbital parameters of an object in the TLE database which is being detected multiple times.

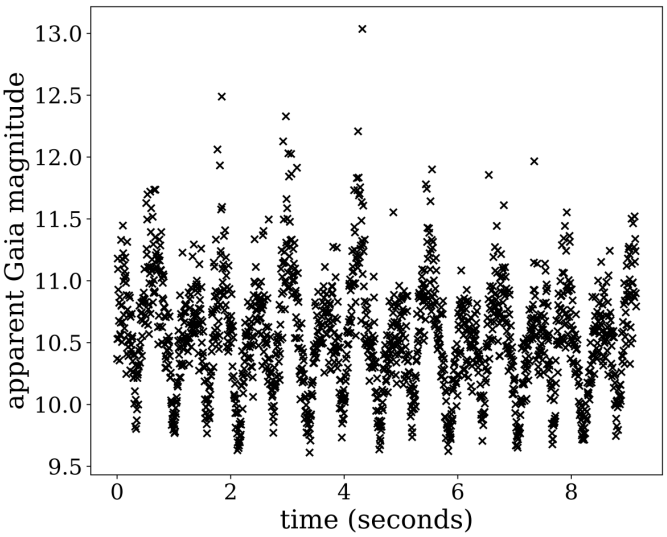

Figure 2.14: The light curve of object 6, detected on 18th May 2015, showing periodic variations with two distinct maxima and minima, probably due to the very fast rotation of an irregular body. The angular velocity of this object is approximately 1 rotation per second.

2.3.2 Debris size estimation

The shape and surface structure of orbital debris can be very complex. So, it is difficult to describe accurately a vast population of debris with a unique model. From the satellite catalog information available from the U.S. Air Force Space Command, 8 out of the 12 identified objects are found to be non-functional payloads and the others are rocket bodies. A study conducted

by Hejduk (2011) suggests that the photometric behavior of 50% of non-geostationary payloads, 70% of rocket bodies and 80% of debris objects can be represented by a diffuse-specular Lambertian sphere model.

The phase function, $F(\varphi)$, represents the angular distribution of sunlight intensity scattered by an object at a given wavelength as a function of the phase angle φ. The phase functions of a diffuse sphere $F_1(\varphi)$ and a specular sphere $F_2(\varphi)$ can be represented as (Williams and G.A., 1966),

$$F_1(\varphi) = \frac{2}{3\pi^2}[(\pi - \varphi)\cos\varphi + \sin\varphi], \tag{2.8}$$

$$F_2(\varphi) = \frac{1}{4\pi}. \tag{2.9}$$

In the context of the diffuse-specular Lambertian sphere model, a mixing coefficient β is used to combine both these phase functions. Mathematically,

$$F(\varphi) = \beta F_1(\varphi) + (1 - \beta)F_2(\varphi). \tag{2.10}$$

Figure 2.15 shows the effect of β on the combined phase function.

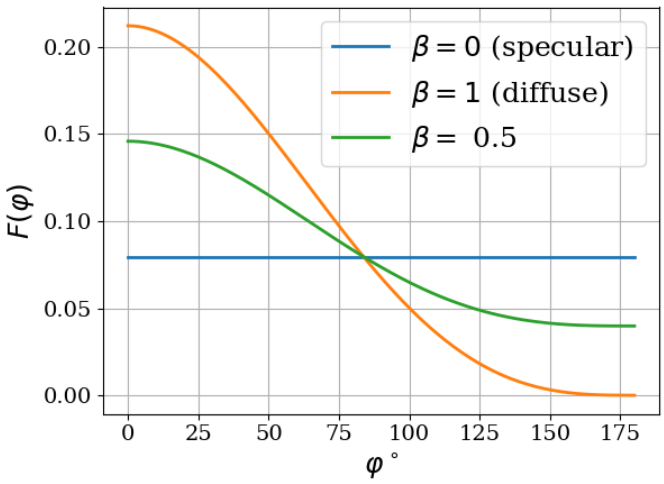

Figure 2.15: Diffuse-specular Lambertian phase function for different values of β.

This means that a value of $\beta = 1$ or 0 would represent a purely diffused or specular sphere, respectively. The apparent brightness m of the reflected sunlight from the sphere can be expressed as;

$$m = m_\odot - 2.5\log(A\rho[\beta F_1(\varphi) + (1 - \beta)F_2(\varphi)]) + 5\log(r), \tag{2.11}$$

where $A = \pi d^2/4$ is the cross-sectional area of the sphere having a diameter d, $m_\odot$ is the apparent magnitude of the Sun, ρ is the albedo and r is the range to the object. By replacing the values of $F_1(\varphi)$, $F_2(\varphi)$ and A, the expression for the optical diameter of the hybrid model can be written as;

$$d = \frac{r10^{-0.2(m-m_\odot)}}{\sqrt{\rho[\frac{\beta}{6\pi}[\sin\varphi + (\pi-\varphi)\cos\varphi] + \frac{1-\beta}{16}]}}. \tag{2.12}$$

In this analysis equal weight to both the specular and diffuse components were assigned by setting β at 0.5. For comparison, we also considered the case $\beta = 1$ (pure diffuse Lambertian sphere) (see Table 2.2). Hejduk (2011) also demonstrated that the contribution of earthshine on the size estimation for objects having a small solar phase angle ($\varphi < 120°$) is negligible. As the objects listed in Table 2.2 have smaller φ, we did not have to take into account the effect of earthshine in our analysis.

To estimate the apparent magnitude m_G of the object, the total flux f of the streak was divided by the time taken to cross the detector, which is the ratio between the angular streak length l and the angular rate v computed from the TLE,

$$m_G = -2.5\log(fv/l) + m_0, \tag{2.13}$$

where m_0 is the magnitude zero point determined by matching stars in the Gaia catalog.

The apparent Gaia magnitude of the Sun was estimated by applying the color transformation given by Jordi et al. (2010) to the Sun's V magnitude of -26.72. This leads to $m_{G\odot} = -26.95 \pm 0.38$.

The albedo ρ was taken to be 0.175 (Mulrooney and Matney, 2008). Since our observations were made near the zenith, the range is equal to the altitude of the object, which was determined from the TLE. The solar phase angle was computed from the observed time and observatory topocentric coordinates using standard relations. The estimated diameters of the detected objects are listed in Table 2.2. The uncertainties in the size estimation were calculated from the uncertainties found in the flux estimation.

From the ESA's Database and Information System Characterising Objects in Space (DISCOS) (Flohrer et al., 2013), the estimated cross-section of 10 of the 12 identified debris could be retrieved. This database contains the minimum and maximum observed cross-sections of the resident space objects. We also calculated the optical cross-section ($\pi d^2/4$) for those 10 objects from the current diameter d (see Table 2.2). These independent sets of results are presented in Table 2.3. The size estimates for both the hybrid model and pure diffuse Lambertian sphere model are found to be comparable to the measurements obtained from the online source catalog except for the case of object 4. We also could obtain the shape and size information of object 2 (SSN 24827) from RussianSpaceWeb.com. The object was found

to be a reconnaissance satellite equipped with a telescope setup of 2 meters diameter and a length of 6.9 meters. There are also solar panels attached to it. So, the dimensions of the satellite can possibly come into agreement with our effective optical diameter estimates of 7.6 or 5.9 meters listed in Table 2.2.

The limiting magnitude for 1000-km LEO objects seen at a solar phase angle of 50° with a β value of 0.5 is estimated from the faintest observed track, which has a signal-to-noise ratio of 18, to be $m_G \simeq 8.4$ for the DFOT telescope under seeing conditions of 1 arcsec. This corresponds to a diameter of 50 cm. The signal-to-noise ratio of the streak was calculated by dividing the total integrated flux of the streak by the total noise from an equivalent streak area. Under similar conditions, the larger aperture and field of view of the ILMT with a better telescope system efficiency (see Table 2.5) should result in a limiting magnitude of $m_G \simeq 13.6$, with a corresponding diameter of 5 cm. A comparison of diameter limits for both telescopes, as a function of altitude, is shown in Figure 2.16. Considering the 11 allocated nights of observation and the two-line element predictions, we found that 10 additional cataloged objects passed the field of view of the 1.3-m DFOT at the appropriate times but these were not detected on our frames. So, the limiting magnitude is used to set a maximum size limit (d_{max}) to these objects. However, the size information on these objects could not be found from online sources for a comparison. The list of all undetected objects and the maximum size limit assigned to them are listed in Table 2.4.

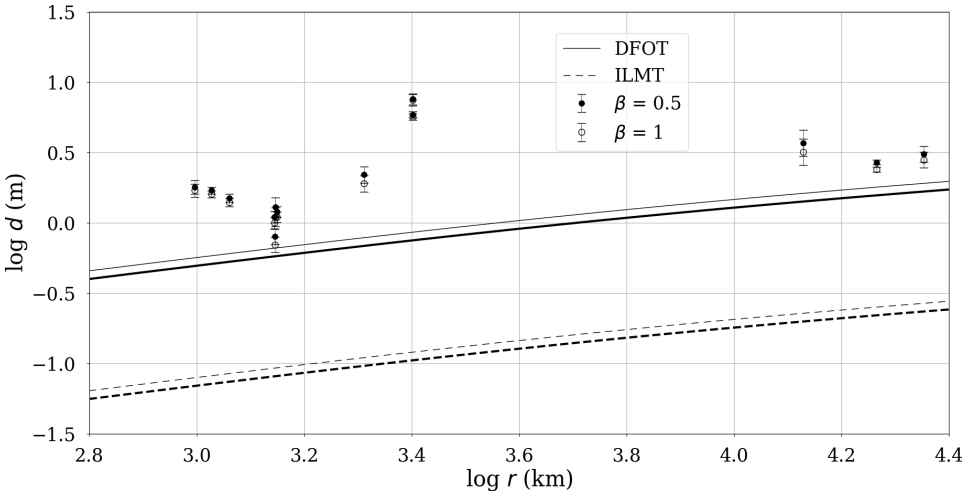

Figure 2.16: Estimated size of the identified debris as detected by DFOT for the β values of 1 (thick lines) and 0.5 (thin lines). The solid lines indicate the minimum detection capability of DFOT. The dashed lines indicate the predicted detection threshold for the ILMT.

In this chapter, we learnt the TDI observation technique used for astronomical surveys. In this test study, the 1.3-m DFOT telescope was operated in the same TDI mode as that of the ILMT. The efficient data reduction technique applicable to the TDI frames provided a photometric precision of 0.04 magnitudes and astrometric precision of approximately 0.1 arcsec for point like objects. 12 objects were successfully detected passing overhead in the form of streaks on the CCD images. Identification of the objects was achieved by cross matching their observed time and direction to those from the TLE. Once the identifications were made, their apparent magnitudes were derived using TLE information on their angular velocity and altitude. The precision of these photometric measurements depends on the velocity and the orientation of the streak. The error associated with the derived magnitudes of the objects are calculated from the noise present in the streak signal. The precision of the detection time of the objects was found to vary between 1 and 23 seconds. However, the uncertainties associated with TLE predictions may also lead to some faulty identification of the objects. If the hybrid diffuse-specular Lambertian sphere is representative of this population of space debris, their estimated diameters range from 0.8 to 7.6 m. Cross-section estimates of 9 out of the 10 identified objects are consistent with the values retrieved from online sources, while one (object 4) seems to differ appreciably. Compatibility of the size estimates can be better addressed in the future thanks to multiple detection of the objects with a dedicated telescope, such as ILMT. The detection threshold of DFOT could be used to set an upper size limit to fainter debris which have crossed the field of view of the DFOT CCD but were not visually detected. The 4-m ILMT telescope, with its 27-arcmin-square field of view and fainter detection threshold, should be able to detect many more space debris, down to a size of approximately 5 cm in low Earth orbits. All these results have been published in the journal 'Acta Atsronautica' (Pradhan et al., 2019). A pipeline has also been developed using Python 2.7 programming with Numpy/Scipy libraries to reduce and calibrate the TDI data automatically. One original contribution in the data reduction has been the noticeable improvement in the quality of the flat fielding of the TDI images based upon the use of the uniform sky background which dominates in the recorded flux of the faintest detected object.

Table 2.1: Log of TDI observations†

Date (YYYYMMDD)	Filter (SDSS)	Observation duration (UT)	Number of science images
20150516	i′	$18^h01^m35^s$ to $21^h01^h32^h$	26
		$21^h14^m03^s$ to $23^h14^m01^s$	
20150517	i′	$15^h41^m14^s$ to $22^h24^m25^s$	33
20150518	g′	$14^h46^m44^s$ to $23^h08^m23^s$	41
20150519	r′	$18^h28^m00^s$ to $23^h04^m30^s$	23
20150520	r′	$16^h09^m36^s$ to $16^h20^m53^s$	26
		$17^h12^m38^s$ to $18^h47^m16^s$	
		$19^h00^m01^s$ to $22^h25^m07^s$	
20150521	i′	$17^h20^m19^s$ to $23^h09^m32^s$	22
20150522	i′	$17^h16^m34^s$ to $23^h06^m01^s$	23
20150523	r′	$14^h51^m57^s$ to $16^h43^m54^s$	09
20150524	r′	$15^h26^m38^s$ to $23^h07^m54^s$	38
20150525	i′	$15^h18^m47^s$ to $15^h30^m04^s$	04
		$15^h48^m09^s$ to $16^h12^m45^s$	
20150526	i′	$17^h59^m35^s$ to $20^h48^m04^s$	14

† Each science image has a dimension of 27952×2048 pixels for a total observing time of 630 seconds.

Table 2.2: Characteristics of the detected objects†

No.	SSN	Date (UT)	Time (UT)		Δt	ϕ (°)		$\Delta\phi$	m_G	r	v	d (m)		φ	Object type
			Pred.	Obs.	(s)	Pred.	Obs.	(°)		(km)	(″/sec)	$\beta = 1$	$\beta = 0.5$	(°)	
1	13070	2015-05-16	20:16:41	20:17:21	40	24.5	24.5 ± 1.0	0.0	11.8 ± 0.1	18423.2	30.0	2.4 ± 0.1	2.7 ± 0.1	54.3	Payload
2*	24827	2015-05-16	23:07:50	23:08:30	40	154.1	152.3 ± 0.6	1.8	5.6 ± 0.2	2525.4	507.0	7.5 ± 0.7	7.6 ± 0.7	81.6	Payload
3	22689	2015-05-17	21:50:14	21:50:42	28	6.7	4.7 ± 0.1	2.0	8.3 ± 0.1	1411.0	1016.0	1.1 ± 0.1	1.2 ± 0.1	67.5	Payload
4	22488	2015-05-17	22:15:29	22:15:58	29	7.2	4.9 ± 0.1	2.1	6.6 ± 0.2	991.2	1446.8	1.7 ± 0.2	1.8 ± 0.2	71.8	Rocket body
5*	29669	2015-05-18	16:20:11	16:20:30	19	20.2	20.2 ± 1.1	0.0	12.0 ± 0.3	22516.3	22.7	2.8 ± 0.4	3.1 ± 0.4	59.0	Rocket body
6	32271	2015-05-18	17:58:57	17:59:07	14	156.4	156.3 ± 0.2	0.1	10.5 ± 0.5	13434.0	54.6	3.2 ± 0.8	3.7 ± 0.8	49.8	Rocket body
7*	4367	2015-05-19	21:05:09	21:05:03	6	12.6	14.6 ± 0.1	2.0	6.7 ± 0.1	1065.4	1376.5	1.6 ± 0.1	1.7 ± 0.1	60.8	Rocket body
8	10539	2015-05-19	21:42:34	21:42:37	3	168.7	167.0 ± 0.7	1.7	7.3 ± 0.1	1151.0	1223.0	1.4 ± 0.1	1.5 ± 0.1	66.5	Payload
9*	17582	2015-05-24	20:34:52	20:35:30	38	6.9	5.6 ± 0.9	1.3	9.3 ± 0.1	1396.3	1027.6	1.0 ± 0.1	1.1 ± 0.1	57.6	Payload
10	22646	2015-05-17	16:01:40	16:02:01	39	175.4	174.8 ± 0.1	0.2	11.2 ± 0.5	1401.2	1024.4	1.1 ± 0.1	1.3 ± 0.1	61.4	Payload
11*	25770	2015-05-18	16:31:44	16:32:27	43	140.4	137.8 ± 0.3	2.2	7.6 ± 0.3	2046.0	660.4	1.9 ± 0.3	2.2 ± 0.3	57.5	Payload
12	24827	2015-05-19	22:36:45	22:37:18	33	154.0	152.4 ± 0.3	1.6	6.0 ± 0.1	2525.6	507.0	5.7 ± 0.3	5.9 ± 0.3	75.8	Payload
13	16759	2015-05-17	20:30:14	20:30:44	30	166.6	164.8 ± 0.1	1.8	8.8 ± 0.1	1399.5	1019.0	0.7 ± 0.1	0.8 ± 0.1	55.9	Payload

† SSN is the catalog number of the object in the database of the US Space Surveillance Network and Δt and $\Delta\phi$ are the absolute differences between the predicted and observed times and directions, respectively. The remaining symbols are described in the text. The asterisk symbol (*) is assigned to the debris having an observed time accuracy of 1 second.

Table 2.3: Estimated and archived debris cross-sections

No.	SSN	Optical cross-section (m^2)		Cross-section from DISCOS (m^2)	
		$\beta = 1$	$\beta = 0.5$	min	max
1	13070	4.5 ± 0.4	5.7 ± 0.4	1.5	13.8
3	22689	0.9 ± 0.2	1.1 ± 0.2	0.5	1.4
4	22488	2.3 ± 0.5	2.5 ± 0.6	4.5	16.4
5	29669	6.2 ± 1.8	7.5 ± 1.9	5.6	10.2
6	32271	8.0 ± 4.0	10.8 ± 4.6	4.2	8.7
7	4367	2.0 ± 0.3	2.3 ± 0.3	1.8	9.6
9	17582	0.8 ± 0.2	1.0 ± 0.2	0.5	1.4
10	22646	1.0 ± 0.2	1.3 ± 0.2	0.5	1.4
11	25770	2.8 ± 0.9	3.8 ± 1.0	0.4	6.8
13	16759	0.4 ± 0.1	0.5 ± 0.1	0.5	0.6

Table 2.4: Upper size limit of the undetected objects†

No.	SSN	Date (UT)	Time (UT)	r (km)	d_{max} (m)	φ (°)	Object type
1	29904	2015-5-16	21:54:05	868.7	0.53	67.5	Satellite debris
2	39321	2015-5-17	21:50:40	704.0	0.48	67.0	Satellite debris
3	18807	2015-5-17	22:15:13	1191.5	0.62	71.0	Satellite debris
4	37704	2015-5-18	21:09:02	1180.1	0.61	60.3	Satellite debris
5	30662	2015-5-18	21:25:57	900.4	0.54	62.9	Satellite debris
6	34683	2015-5-18	22:18:28	735.4	0.49	71.7	Satellite debris
7	27688	2015-5-22	21:37:02	702.6	0.48	64.7	Satellite debris
8	23418	2015-5-24	22:10:49	888.3	0.54	70.0	Satellite debris
9	30079	2015-5-24	22:41:17	896.5	0.54	75.8	Satellite debris
10	27902	2015-5-26	19:36:25	9068.9	1.42	47.1	Satellite debris

† The size information of these objects from online sources is not available.

Table 2.5: Telescope parameters of DFOT and ILMT

	DFOT (Kumar and Shreekar) (Santa Barbara Instrument Group)	ILMT (Kumar et al., 2018)
Primary mirror diameter	1.31-m	4.0-m
Fraction of reflecting area	0.69	0.95
System efficiency in SDSS i'	0.42	0.63

3

Automatic streak detection

The optimal way of detecting an expected feature present in a signal with the highest signal-to-noise ratio (SNR) is to correlate the feature with the signal itself (Helstrom, 1968). In this case, the feature is called the matched filter or correlation filter. A detailed overview of the matched filter technique is presented in Section 3.1.1. We have implemented this concept in Section 3.1.2 in the context of faint streak detection. Numerical simulations to illustrate the effectiveness of this approach are subsequently addressed in Section 3.1.3. A computationally efficient method has also been developed by adopting the matched filter technique in the Fourier space which is discussed in Section 3.2. To validate the proposed detection method, a wavelet based contrast enhancement method is proposed subsequently in Section 3.3. We have also independently tried out few other detection techniques readily available to detect streaks and asserted their efficiency in Section 3.4. One of these techniques, widely known as 'Hough transformation' (Duda and Hart, 1972) is a feature extraction technique in digital images. In our case the feature is of course a debris streak. Another technique we have tried to use is the 'Radon transform' (Radon, 1986) in Fourier space proposed by Hickson, 2018 to detect the streaks in the CCD images and compared its performance to our proposed method.

The matched filter technique demands that an image should be devoid of any signal other than the streak itself for a most accurate detection. So, an efficient image subtraction technique becomes essential. In Section 3.5, a detailed explanation on how image subtraction can be performed thanks to discrete convolution kernels will be explained based on previous work by Bramich, 2008 (DanDia). The DanDia algorithm assumes that the reference image and the target image have the same shape and are roughly

aligned. However, some of the CCD images obtained using DFOT in 2015 are misaligned or rotated with respect to each other depending upon the telescope pointing. After addressing these issues, that section illustrates the application of the DanDia algorithm on a set of TDI images resulting in the detection and characterization of a few faint debris streaks.

3.1 The Matched filter technique for debris streak detection

3.1.1 Matched filter technique

In this section, a detailed overview of the matched filter technique leading to the analytical modeling of a CCD detected streak is described.

Overview

The matched filtering algorithm has been widely used to detect streaks on digital images. The scenario where a streak is formed on an optical detector is investigated to construct the best matched filter. Then the cross-correlation of the streak signal with the matched filter is performed to maximize the SNR of the extracted signal with respect to the noise. Gural et al. (2005) have used this technique to build a software at the disposal of the NASA data services to detect near-Earth asteroids. Levesque (2009) also has implemented this algorithm to achieve a very high accuracy for the detection of satellite streaks on optical images. A significant work also has been done in detecting space debris streaks on optical images by Schildknecht et al. (2015) by modelling matched filters of variable lengths and orientations.

A faint debris can be considered as a point source in a linear motion across the sky. The point source moving across the field of view of the CCD will create a streak on the CCD read-out image as a result of the integration of the point spread function (PSF) along the source's direction of motion. The CCD frames obtained from passive optical observations implementing TDI imaging often contain such streaks. This is also true for classical surveys. Let us consider for the moment that the streak is perpendicular to the CCD columns or the read-out direction. A 2-D analytical PSF described by a circularly symmetric normalized Gaussian function centered on (x_0, y_0) is shown in Figure 3.1, where x and y are the pixel positions along the CCD columns and rows, respectively. The streak formed from the integration of the PSF, perpendicular to the CCD columns is also shown in Figure 3.1. Mathematically, it can be expressed as,

$$PSF_I(x - x_0) = \int PSF(x - x_0, y - y_0)dy.$$

Let us note that the profile $PSF_I(x - x_0)$ is also supposed to be normalized after integration along the x-axis. Considering this case where the streak is characterized by projecting the PSF along a certain direction, the best matched filter for optimizing the SNR of the streak profile is the projected version of the PSF itself.

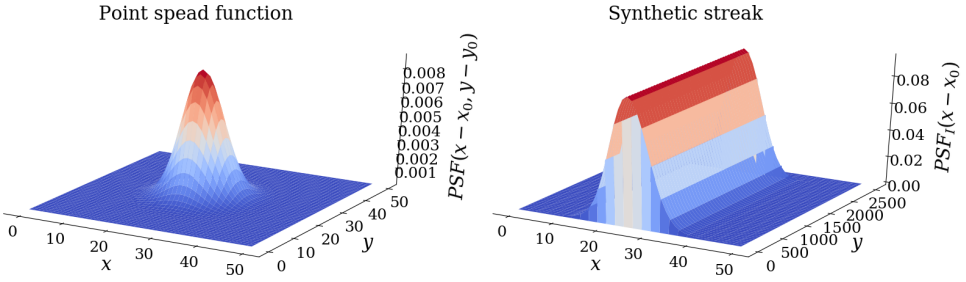

Figure 3.1: A PSF expressed as a normalized two-dimensional Gaussian function (on the left) and a streak created by co-adding the PSF along the y-axis.

The two dimensional synthetic streak profile shown in Figure 3.1 is the replication of the 1-D streak profile $PSF_I(x - x_0)$ along the y-axis. So the whole streak profile can be optimized for detection simply by correlating the 1-D streak shape along its width with the matched filter. The streak signal along the width of the streak can be represented theoretically by

$$S(x) = \alpha \; PSF_I(x - x_0), \tag{3.1}$$

where α is the total number of photons collected by the CCD during the transit of the faint space debris. Following the foregoing discussion, $PSF_I(x)$ is regarded as the matched filter. The SNR of the streak profile will then be maximized by its cross-correlation with the matched filter. We have represented the numerator of the maximized SNR as the peak of the cross-correlation result. The peak occurs at $x = x_0$ and its value is,

$$|S(x) \circledast PSF_I(x)|_{max} = \alpha \; Q, \tag{3.2}$$

where

$$Q = \int PSF_I^2(x)dx. \tag{3.3}$$

We assume here that the dominant factor contributing to the noise associated with a faint debris streak is the sky background. The effect of the cross-correlation with the matched filter on the noise variance (σ^2) along a single CCD row associated with $S(x)$ can be estimated using the property of variance as shown below,

$$\begin{aligned} Var\left[\sum_n S(x)PSF_I(x-n)\right] &= \sigma^2 \sum_n PSF_I(x-n)^2 \\ \Rightarrow \sigma^2_{corr} &= \sigma^2 \; Q, \end{aligned} \tag{3.4}$$

where σ^2_{corr} is the filtered noise variance. Now, the maximized SNR will be the ratio between the peak of the matched filtered streak signal and the square root of the matched filtered signal variance. So, after taking the ratio of the output from Equation 3.2 and the standard deviation or the square root of the output from Equation 3.4, the maximized SNR can be written as,

$$SNR_{max} = \frac{\alpha}{\sigma}\sqrt{Q}. \tag{3.5}$$

We see here the benefit of observing under the best seeing conditions since the Q factor gets higher whenever the PSF tends to be narrower.

Analytical modeling

The total photon counts α from a space debris having a flux density FSD (photon m^{-2} s^{-1}) moving with an angular velocity $AVSD$ (arcsec s^{-1}) across the CCD having a width θ_{CCD} (arcsec) is,

$$\alpha = FSD\frac{\theta_{CCD}}{AVSD\sin(\theta)}\pi\left(\frac{D}{2}\right)^2\epsilon, \tag{3.6}$$

where, D (meters) and ϵ are the diameter of the telescope in use and the overall instrumental efficiency, respectively. θ is the angle subtended by the streak with respect to the CCD columns (for the moment, we have assumed it to be 90°). If the point spread function at the telescope focal plane is represented by a symmetric two-dimensional Gaussian function, then its projection i.e., the matched filter will be a one-dimensional Gaussian function bearing the same full width at half maximum ($FWHM$). So, Q stated in Equation 3.3 can be expressed analytically as,

$$\begin{aligned} Q &= \int PSF_I(x)^2 dx, \\ &= \int \left[\frac{2\sqrt{\ln 2}}{FWHM\sqrt{\pi}}\ exp\left(-x^2\frac{4\ \ln 2}{FWHM^2}\right)\right]^2 dx, \\ &= \frac{\sqrt{2\ \ln 2}}{\sqrt{\pi}\ FWHM}. \end{aligned} \tag{3.7}$$

The sky background detected on the discrete CCD pixels follows a Poisson distribution. Its variance σ^2 over a single pixel row can be approximated as,

$$\sigma^2 = SB\frac{\theta_{CCD}}{AVS\ \cos(\delta)}\pi\left(\frac{D}{2}\right)^2\epsilon\ \theta_{pixel}\theta_{CCD}, \tag{3.8}$$

where SB is the sky brightness expressed in photons m^{-2} s^{-1} $arcsec^{-2}$, AVS is the apparent angular velocity of the stars in arcsec s^{-1} while observing with

a telescope pointed at zenith, θ_{pixel} is the angular size of the square shaped pixels and δ (degree) is the declination at which the TDI observations are being made.

Finally the maximized SNR of the 1D streak profile can be analytically formulated by replacing the mathematical expressions of α, Q and σ from Equations 3.6, 3.7 and the square root of Equation 3.8, respectively in Equation 3.5 :

$$SNR_{max} = \frac{FSD\ D}{AVSD \sin(\theta)} \left(\frac{\pi\ \ln 2}{8} \right)^{\frac{1}{4}} \left(\frac{\epsilon\ AVS\ \cos(\delta)}{FWHM\ SB\ \theta_{pixel}} \right)^{\frac{1}{2}}. \tag{3.9}$$

3.1.2 Streak detection

Detection of a streak in an image is achieved by determining its orientation, location and brightness. A well known method to find the orientation of a feature in an image is by analysing the results after performing convolution with the matched filter aligned at various angles (Freeman and Adelson, 1991; Jacob and Unser, 2004). The angle at which the filter output is maximum happens to be the orientation angle.

The streaks found on CCD frames will have different orientations. Our objective here is to bring the streak to a vertical position so that a simple average of pixel values along the length of the streak will produce a one-dimensional streak signal ready for matched filtering. Figure 3.2 shows different orientations of a synthetic streak on a CCD grid and the average pixel values along the rows. The streaks shown in the subplots of Figures 3.2a, 3.2b and 3.2c are inclined by 60°, 75° and 90° respectively with respect to the CCD columns. The average pixel values obtained from the vertically oriented streak along the pixel rows in Figure 3.2c give the optimal representation of the cross-section of the streak profile.

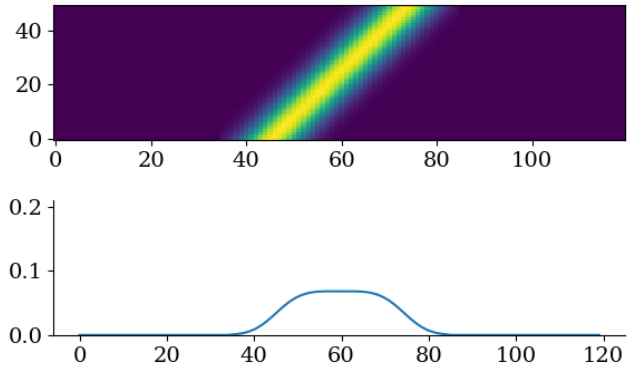

(a)

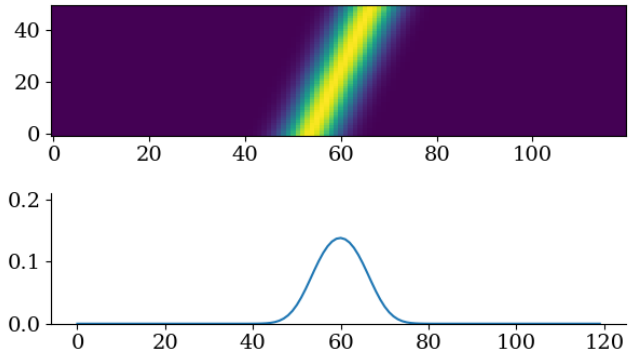

(b)

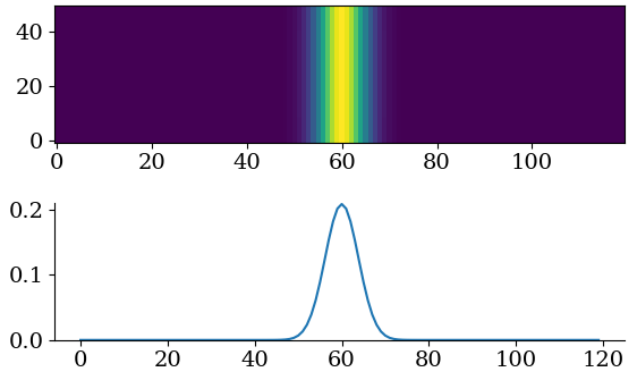

(c)

Figure 3.2: Streaks simulated on a CCD grid by integrating a normalized 2D Gaussian with a FWHM of 10 pixels inclined at different angles with respect to the CCD columns and the average value of all columns. Plots (a), (b) & (c) shows the streaks inclined by 60°, 75° and 90°, respectively with their average pixel columns values.

The rotation of a lengthy frame (such as acquired in the TDI mode) will be computationally expensive. The same qualitative result can be achieved by a faster image shearing technique. In this method, each column is shifted by a value of $n/\tan(\theta)$, where n is a zero-based row number, like in Figure 3.3. Since we do not know the exact orientation of the streak in practical cases, the image is sheared at each iteration by an angular step $\delta\theta$ to sample all possible shearing angle values θ. The value of the angular step is set in such a way that each pixel is shifted from its previous position by at most a single pixel at the bottom of the CCD frame. Mathematically, the angular step can be expressed in degree as

$$\delta\theta = \frac{\theta_{pixel}}{\theta_{CCD}} \frac{180}{\pi}. \tag{3.10}$$

Then the average of the pixel values along the rows for each shearing angle is convolved with the matched filter. The 1D convolution results are stacked one after another in such a manner that a 2D grid is constructed with one axis representing the columns of the frame and the orthogonal axis representing the shearing angle (θ). The location of the peak value of this new 2D maximized intensity map will apparently give the information about the bottom location of the streak and its orientation. The study of such a convolution intensity map has been widely used for pattern recognition or feature detection in noisy images (Hester and Casasent, 1980; Savvides et al., 2002; Diaz-Ramirez et al., 2006; Close et al., 2011).

The peak value in the intensity map (i.e. αQ) represents a streak detection and if divided by σ_{corr} (see Eq. 3.4), also provides the maximized SNR of the streak (see Eq. 3.5). Similarly, dividing the peak value by Q leads to the determination of the flux α of the space debris integrated over the CCD field. Indeed, using Equations 3.2 and 3.7, we obtain,

$$\alpha = |S(x) \circledast PSF_I(x)|_{max} \frac{\sqrt{\pi}\ FWHM}{\sqrt{2\ \ln 2}}. \tag{3.11}$$

A streak with a SNR_{max} of 100 having a $FWHM$ of 9 pixels is shown in Figure 3.4. The transformed intensity map of this image is shown in Figure 3.5. The ratio of the peak of the intensity map and the correlated standard deviation was calculated to be 96.48, i.e. close to 100. The location of the peak on the intensity map was also found to be equal to the known streak orientation and bottom location values. A python implementation of this algorithm takes around 300 seconds to process an image of 6144×2048-pixels size with a CPU speed of 2.10 GHz and 16 Gb memory.

3.1.3 Monte Carlo simulations

To verify the effectiveness of the proposed detection technique, a large number of synthetic frames containing customized streaks have been generated.

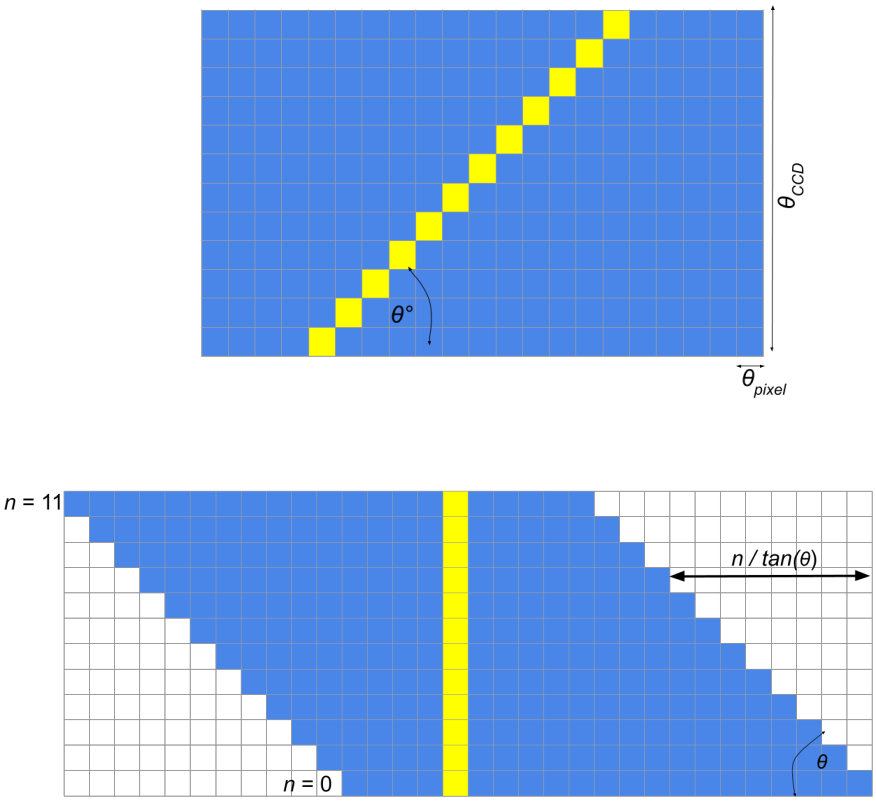

Figure 3.3: Illustration of the shearing of a CCD image (blue) with a streak (yellow) inclined by an angle θ with respect to the columns. The subplot at the top shows the unsheared image and the bottom one shows the image after shearing by an angle θ.

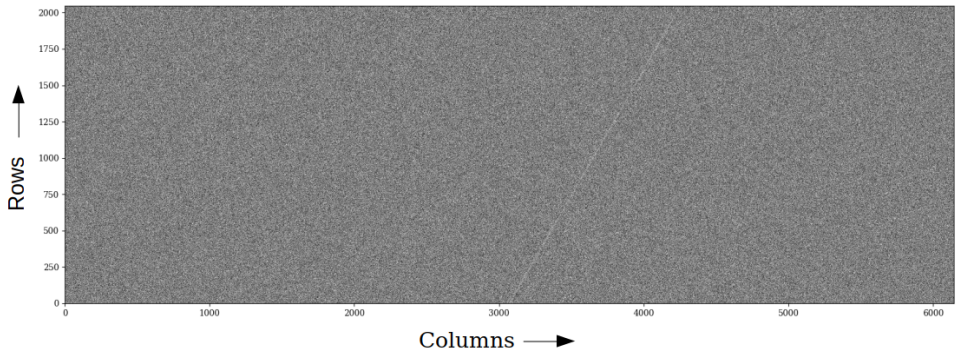

Figure 3.4: A CCD image having a size of 6144×2048-pixels, containing a faint streak with a SNR_{max} of 100, inclination angle (θ) of 60° and $FWHM$ of 9 pixels.

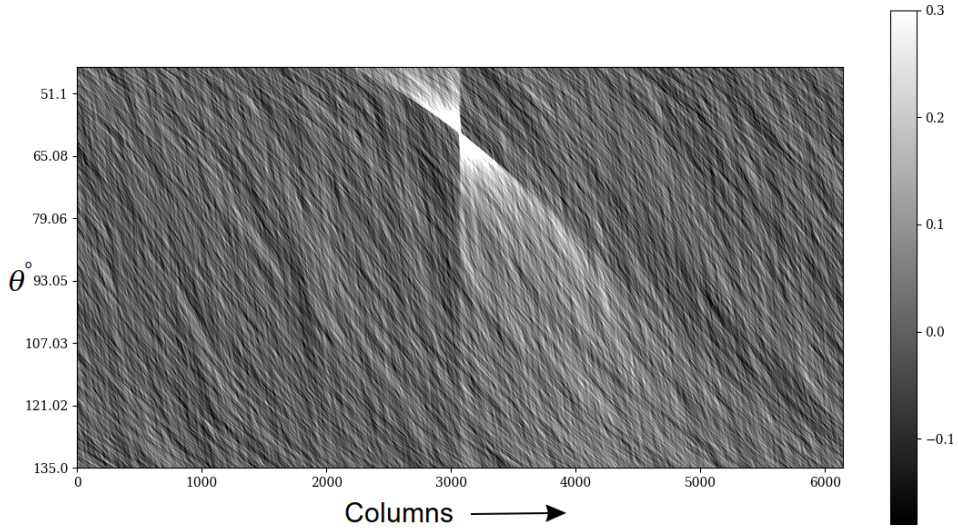

Figure 3.5: The transformed 2D intensity map of the image in Figure 3.4. The peak value in this image corresponds to a streak with SNR_{max} of 100, inclined by 60°(θ) with respect to the CCD columns and the bottom of this streak located at the 3080th pixel along the columns.

The size of each frame is kept to 6144×2048-pixels and each pixel unit has been considered to be 0.3 arcsec. In each frame, the profile of a 1D Gaussian PSF is scaled and replicated along the columns in a fixed direction to generate a streak. Different seeing conditions are used against a fixed Gaussian noise background and the streaks are placed at random positions and orientations on the frame. In total, the free parameters in generating the streaks can be summarized as:

1. The seeing conditions, or $FWHM$ from which Q is determined.

2. The detection SNR_{max}, from which the streak amplitude α is calculated against a fixed noise level.

3. The position of the streak along the columns.

4. The orientation of the streak, i.e. θ.

The synthetic streaks having a SNR_{max} below 30 are not visible to human eyes in 2K×2K or larger images unless they are digitally magnified. So, in our simulations we have kept the value of the free parameter SNR_{max} between 1 to 25 against a Gaussian background noise having a standard deviation $\sigma = 10$ to represent faint streaks. The $FWHM$ has been varied between 1" and 3". The inclination angle of the streaks has been set between 45° and 135° randomly. In total 1100 synthetic frames have been generated considering a uniform distribution for the values of SNR_{max}, $FWHM$, θ and the bottom locations of the streaks.

The streak detection algorithm discussed in Section 3.1.2 has been applied to each synthetic frame. It is to be noted that the output SNR_{max} is determined by dividing the peak value of the intensity map by the correlated standard deviation (σ_{corr}). To evaluate the reliability of the detection technique, we have used the Receiver Operating Characteristic (ROC) curve. The ROC curve does this by plotting the probability of predicting a real detection, or the True Positive Rate (TPR) vs the probability of predicting a false positive, or the False Positive Rate (FPR) for various threshold settings. The TPR and FPR have been calculated as;

$$\mathrm{TPR} = \frac{\mathrm{TP}}{\mathrm{TP} + \mathrm{FN}}, \tag{3.12}$$

$$\mathrm{FPR} = \frac{\mathrm{FP}}{\mathrm{FP} + \mathrm{TN}}, \tag{3.13}$$

where TP (true positive) corresponds to the true detection of a real streak, FP (false positive) refers to the detection of a non real streak, TN (true negative) occurs when there is no detection for a non real streak and FN (false negative) corresponds to the non-detection of a real streak.

To understand this concept, let us consider the output SNR_{max} as the prediction of the detection algorithm. Now we set a certain threshold value for the parameter SNR_{max}. When the actual SNR_{max} value is greater than the threshold and the prediction is equal to the former, then it is called a TP and if the prediction fails, it will be a FN. When the actual SNR_{max} value is less than the threshold, we assume that there is no streak. In this situation, if the prediction is also not accurate, then it is said to be a TN; but if the prediction is accurate, it will be regarded as a FP.

The ROC curve efficiency is measured from the area under the curve (AUC). The AUC is the probability that the detection algorithm will correctly predict the parameter. So for a AUC value close to 1, the detection

technique can be considered as very accurate and for a value of 0.5, the accuracy of the technique is not reliable at all. We have generated the ROC curve for the parameters SNR_{max} shown in Figure 3.6. The AUC for SNR_{max} is calculated to be 0.99, which suggests that the algorithm has an excellent true parameter value prediction probability. It is also evident here that the FPR is minimum for a SNR_{max} above 6. The plots shown in Figures 3.7a, 3.7b and 3.7c also suggest that there is a higher probability of false detection for a streak having $SNR_{max} \leq 6$.

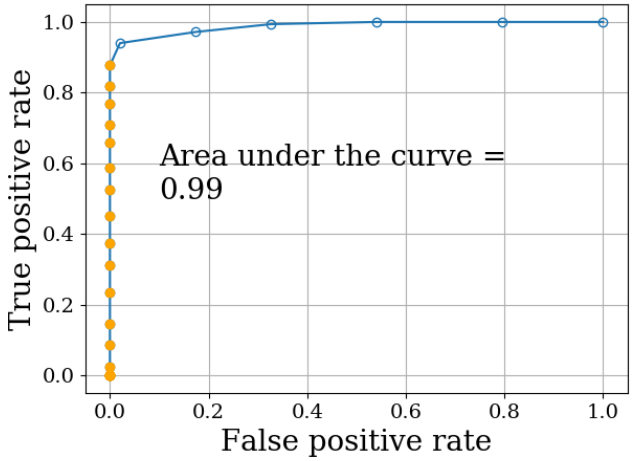

Figure 3.6: ROC curve for predicting SNR_{max}. The filled circles refer to the TPR vs FPR for a $SNR_{max} > 6$.

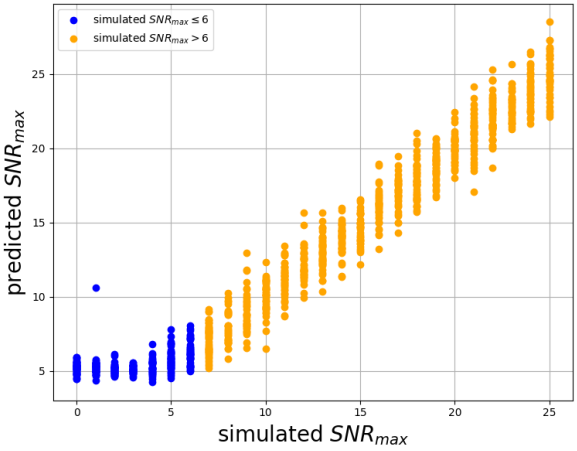

(a)

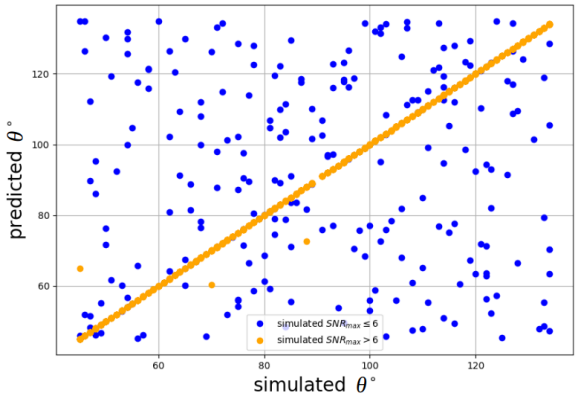

(b)

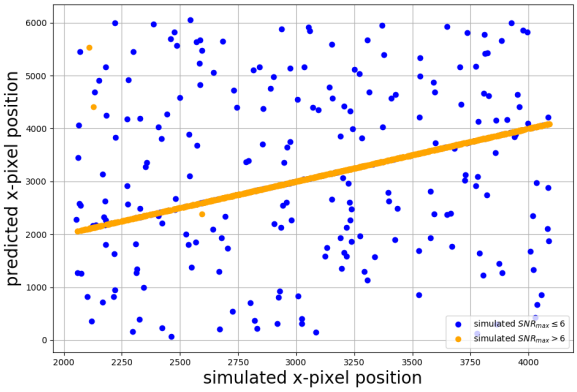

(c)

Figure 3.7: Comparison of simulated SNR_{max}, $FWHM$, inclination angle (θ) and the bottom location of the streaks along the CCD column in the synthetic images with their corresponding estimated values from streak detection.

3.2 Debris streak detection in the Fourier space

Fourier transform is a faster way to perform convolution on two dimensional data. The matched filtering in the frequency domain was first proposed by Dwork (1950). Since then the matched filtering in Fourier space has been adopted widely to detect streaks on digital images. Sanders (1992) used the Fourier matched filter to detect moving point source (satellite) from a sequence of images taken using the Lincoln Laboratory CCD camera. Levesque and Buteau (2007) have demonstrated that faster CPU time can be achieved for streak detection using Fourier space matched filtering. In this chapter, the behaviour of a streak in the Fourier domain has been analyzed and conceptualized. Later it has been tested using simulations and a detection method is proposed. The limitations and possible remedies to this method are also discussed subsequently.

3.2.1 Fourier analysis

Let us first establish the expression of a space debris streak detected on a CCD frame (see streak 1 in Figure 3.8). In terms of the (x', y') coordinates, it takes a very simple form

$$I(x', y') = \alpha\, W(x')\, \frac{1}{\lambda}\, \Pi(\frac{y'}{\lambda}), \tag{3.14}$$

where α represents the integrated flux of the streak, $W(x')$ accounts for the normalized lateral profile of the streak. We have assumed the lateral profile to be a normalized Gaussian function having a width determined by the local seeing conditions and $\Pi(y'/\lambda)/\lambda$ a normalized hat function accounting for the length λ of the streak. Since both the lateral and longitudinal profiles are normalized, we have the obvious relation

$$\int_{-\infty}^{\infty}\int_{-\infty}^{\infty} I(x', y')\, dx' dy' = \alpha. \tag{3.15}$$

Whenever the streak crosses the whole CCD detector from the top (resp. bottom) to the bottom (resp. top; cf. streak 2 in Figure 3.8), we have the relation

$$\lambda = \frac{L}{\cos(\theta)}, \tag{3.16}$$

where L represents the side length of the square CCD camera and θ is the inclination angle of the streak with respect to the $x-$axis. Most of the streaks are characterized by this length λ.

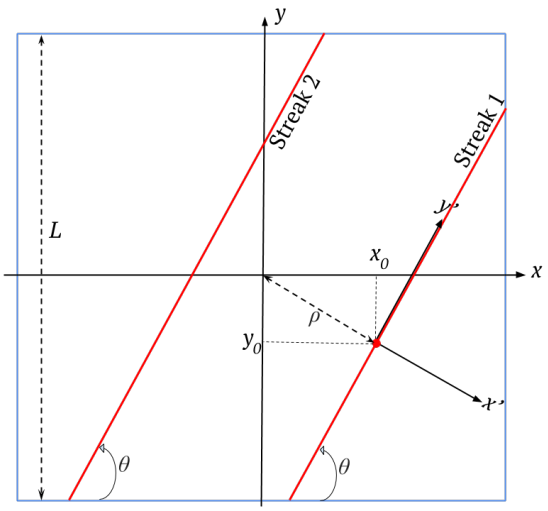

Figure 3.8: A debris streak (1) on a CCD frame looks like the red straight line centered at the (x_0, y_0) position, having a length λ and inclined by the angle θ with respect to the x axis. Another streak (2) is illustrated on the left part of the figure.

Making use of the coordinate transformation

$$\begin{aligned} x' &= (x - x_0)\sin\theta - (y - y_0)\cos\theta, \\ y' &= (x - x_0)\cos\theta + (y - y_0)\sin\theta, \end{aligned} \tag{3.17}$$

the expression of $I(x, y)$ in terms of the (x, y) coordinates takes the form

$$I(x,y) = \alpha\, W[(x-x_0)\sin\theta - (y-y_0)\cos\theta]\,\frac{1}{\lambda}\,\Pi[\frac{(x-x_0)\cos\theta + (y-y_0)\sin\theta}{\lambda}]. \tag{3.18}$$

In the absence of any other contribution (cf. sky background, stars, cosmic rays), the Fourier transform of the light distribution is simply given by

$$FT[I(x,y)](p,q) = \int_{-\infty}^{\infty}\int_{-\infty}^{\infty} I(x,y)\,\exp[-2i\pi(xp+yq)]dxdy. \tag{3.19}$$

Making use of Eq.3.17 and of the converse coordinate transformation

$$\begin{aligned} x &= x_0 + x'\sin\theta + y'\cos\theta \\ y &= y_0 - x'\cos\theta + y'\sin\theta, \end{aligned} \tag{3.20}$$

the previous Fourier transform can be successively rewritten as follows

$$FT[I(x,y)](p,q) = \int_{-\infty}^{\infty}\int_{-\infty}^{\infty} I(x',y')\ \exp[-2i\pi(px_0 + x'\sin\theta + y'\cos\theta) \\ +q(y_0 - x'\cos\theta + y'\sin\theta)]dx'dy', \tag{3.21}$$

or,

$$FT[I(x,y)](p,q) = \int_{-\infty}^{\infty}\int_{-\infty}^{\infty} I(x',y')\ \exp[-2i\pi(x'(p\sin\theta - q\cos\theta) + \\ y'(p\cos\theta + q\sin\theta))]dx'dy'\ \exp[-2i\pi(px_0 + qy_0)], \tag{3.22}$$

and finally

$$FT[I(x,y)](p,q) = FT[I(x',y')](p',q')\ \exp[-2i\pi(px_0 + qy_0)], \tag{3.23}$$

with (see Figure 3.9)

$$\begin{aligned} p' &= p\sin\theta - q\cos\theta \\ q' &= p\cos\theta + q\sin\theta. \end{aligned} \tag{3.24}$$

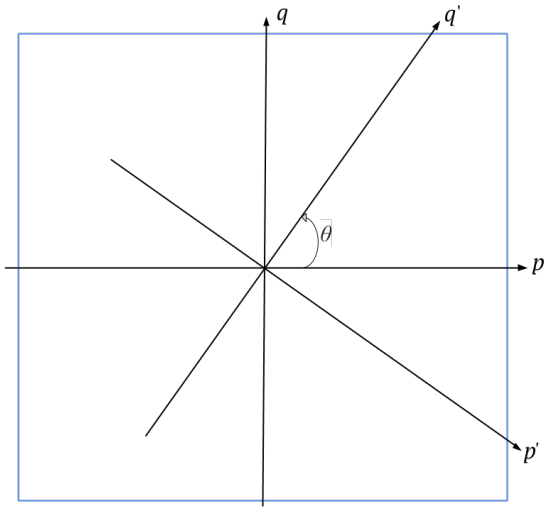

Figure 3.9: Representation of the spatial frequencies p, q and p', q' in the Fourier space.

Let us now evaluate the expression $FT[I(x',y')](p',q')$ appearing in Eq.3.23 for a normalized Gaussian lateral profile

$$W(x') = \frac{\sqrt{\ln 2}}{2FWHM\sqrt{\pi}} \exp(\frac{-4\ln(2)x'^2}{\mathrm{FWHM}^2}), \tag{3.25}$$

where $FWHM$ represents its full width at half maximum. Making use of Eqs. 3.14 and 3.19, we find

$$FT[I(x',y')](p',q') = \alpha\, FT[W(x')](p')\,\frac{1}{\lambda}\,FT[\Pi(\frac{y'}{\lambda})](q'), \tag{3.26}$$

with

$$\frac{1}{\lambda}\,FT[\Pi(\frac{y'}{\lambda})](q') = \frac{\sin(\pi\lambda q')}{\pi\lambda q'} \tag{3.27}$$

and

$$FT[W(x')](p') = \exp\left(\frac{-\pi^2 p'^2 \mathrm{FWHM}^2}{4\ln(2)}\right). \tag{3.28}$$

We notice that narrower is the width of the streak, broader is its Fourier transform in the frequency space.

In Section 3.1, we have been using the matched-filtered technique to detect at best the presence of space debris streaks. To perform a similar action in the Fourier space, we should take the Fourier transform of the convolution product ($\otimes$) of the streak signal $I(x,y)$ and the normalized point spread function $PSF(x,y)$ which is the same expression as $I(x,y)$ but for the case of $\alpha = 1$ and for a chosen angular orientation ϕ on the CCD frame. We thus find

$$FT[I(x,y)\otimes PSF(x,y)](p,q) = FT[I(x,y)](p,q)\,FT[PSF(x,y)](p,q). \tag{3.29}$$

For the case of W(x') being the normalized Gaussian function

$$\begin{aligned} FT[I(x,y)\otimes PSF(x,y)](p,q) = \alpha \exp[\frac{-\pi^2(p\sin\theta - q\cos\theta)^2 FWHM^2}{4\ln(2)}] \\ \frac{\sin[\pi\lambda(p\cos\theta + q\sin\theta)]}{\pi\lambda(p\cos\theta + q\sin\theta)} \exp[\frac{-\pi^2(p\sin\phi - q\cos\phi)^2 FWHM^2}{4\ln(2)}] \\ \frac{\sin[\pi\lambda(p\cos\phi + q\sin\phi)]}{\pi\lambda(p\cos\phi + q\sin\phi)} \exp[-2i\pi(px_0 + qy_0)]. \end{aligned} \tag{3.30}$$

It should then be easy to find out the orientation θ of the streak by integrating the absolute value of $FT[I(x,y) \otimes PSF(x,y)](p,q)$ over the coordinates (p,q) for typically 180 values of the angle ϕ. The proper orientation of the streak corresponds to the value of ϕ for which that quantity shows a real maximum.

The maximum value taking place for $\phi = \theta$ is

$$\int_{-\infty}^{\infty}\int_{-\infty}^{\infty} |FT[I(x,y) \otimes PSF(x,y)](p,q)|dpdq = \alpha \frac{\sqrt{2\ln 2}}{\sqrt{\pi} FWHM} \frac{1}{\lambda}, \quad (3.31)$$

or, by substituting the value of Q from Equation 3.7, the above expression can be re-written as,

$$\int_{-\infty}^{\infty}\int_{-\infty}^{\infty} |FT[I(x,y) \otimes PSF(x,y)](p,q)|dpdq = \frac{\alpha Q}{\lambda}. \quad (3.32)$$

The position (x_0, y_0) of the streak can then be derived from the real and/or complex representation of $FT[I(x,y)]$ in the Fourier space as in Eq.(3.23).

In case of truncated streaks appearing on the CCD frames (cf. streak number 2, 5, 7, 9, 11 in Fig. 2.13), one can first perform some image segmentation (i.e., partitioning the image into several sub-images) and then perform the aforementioned matched filtering. Another way would be to use an appropriate PSF having a similar shape as that of the streak.

3.2.2 Discrete Fourier transform test

In the previous sub-section, we have proposed a strategy to determine the orientation (θ) and the position (x_0, y_0) of a streak using the continuous Fourier transform (CFT). In a pixelized CCD image, a discrete Fourier transform (DFT) better approximates the CFT. We have used the highly efficient algorithm called Fast Fourier Transform (FFT) to evaluate all the DFTs.

At first, a 40×40 pixels image was constructed containing a streak of the form described by Equation 3.14, set perpendicularly to the $x-$axis at $x_0 = 20$. The lateral profile is considered to be a normalized Gaussian function with a $FWHM$ of 5 pixels and the total integrated flux (α) is 10 units. This image and its DFT are shown in Figure 3.10.

Several PSFs are then simulated for different values of ϕ starting from 0° to 180°. The convolution in the Fourier space is achieved from the product of the Fourier transforms of $I(x,y)$ and $PSF(x,y)$ for each value of ϕ and then the absolute values of these products are integrated. The plot between ϕ and the respective results from the integration shown in Figure 3.11 displays a peak at $\phi = 90°$, hence perfectly corresponds to the orientation of the streak.

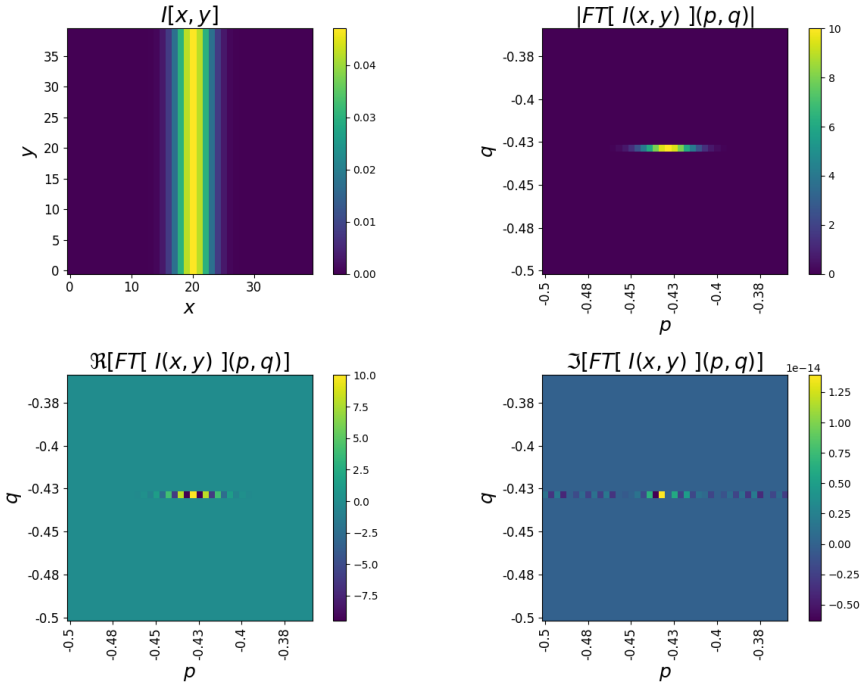

Figure 3.10: Discrete Fourier transform of a streak. The simulated streak (top-left), the absolute (top-right), real (bottom-left) and imaginary (bottom-right) part of the image's DFT are shown.

To determine the position of the simulated streaks we have chi-square fitted the sum of the real and imaginary parts of the image's Fourier transform to their theoretical expression;

$$\begin{aligned} \Re\{(FT[I(x',y')](p',q')\} + \Im\{FT[I(x',y')](p',q')\} = \\ |FT[I(x',y')](p',q')|\ (\ \cos(2\pi[px_0+qy_0]) + \sin(2\pi[px_0+qy_0])\ ), \end{aligned} \tag{3.33}$$

and found out x_0 and y_0. Figure 3.12 shows the sum of the real and imaginary part of the Fourier transform of the simulated streak and the best fitted theoretical curve.

Effect of noise

After a CCD image goes through the cleaning process to get rid of dark noise average, flat field variations and sky background, the noise per pixel can be described by a Gaussian distribution with zero mean and a certain standard deviation σ. The DFT of such a noisy frame produces another Gaussian distributed complex noise frame (Richards, 2014).

Several 2048×2048 pixels images were synthesized keeping a background noise at the level $\sigma = 5$. A streak similar to that shown in Figure 3.10 was

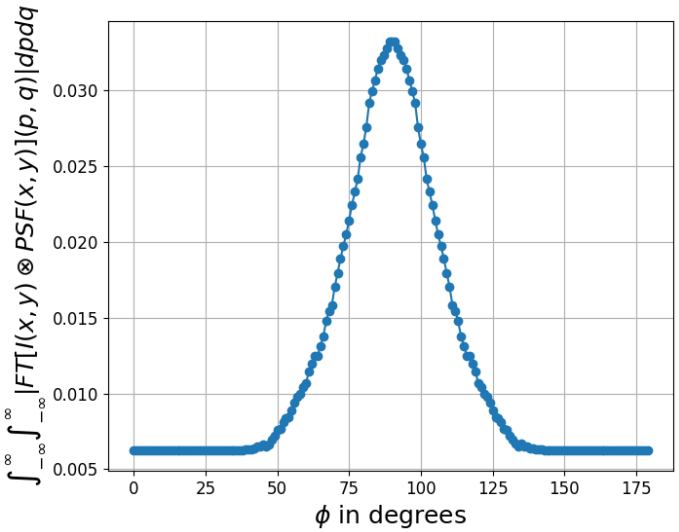

Figure 3.11: Plot between the PSF's inclination angle ϕ and the integrated values of the convolution product in the Fourier space.

then added to each image, but the flux α was varied such that the SNR_{max} (cf. Equation 3.5) takes values from 1 to 25 and the inclination angle θ was varied from 45 to 135 degrees. The values of θ and α were generated from uniform distributions.

For each image, the Fourier analysis was done. From the graph between the values of the integration of the convolution product (described by Eq. 3.31) and ϕ, the inclination angle of the streak was determined. Subsequently the locations of the streaks were also determined using the real and imaginary parts of the Fourier transformed image.

The chi-square fit method to find the streak's position proposed in the previous section was found to be inefficient for faint streaks having $SNR_{max} \leq 20$, where the streak signal per pixel becomes comparable to the rms noise level in the image. So, once the inclination angle ϕ was estimated from the Fourier analysis, we followed the faint streak detection method described in Section 3.1.2 to estimate the bottom position of the streak along the CCD column as well as its SNR_{max}. The processing time for a python implementation of the complete Fourier analysis of a single frame is 10 times faster than the matched filtered technique in the original physical space.

The TPR and FPR were calculated for different threshold values of SNR_{max} and a ROC curve was generated (see Figure 3.13). The area under the curve was estimated to be 0.99, which suggests that the Fourier analysis is as good as the analysis in the original physical space (refer to Figure 3.6). The FPR of the filled circles in the ROC curve belongs to the streaks with

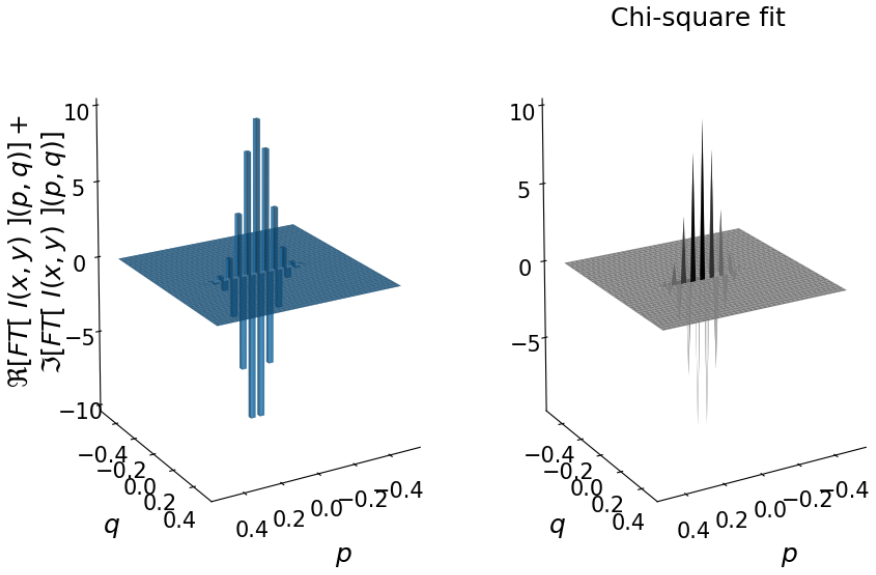

Figure 3.12: Image on the left is the 3-D view of $\Re[FT[I(x', y')](p', q')] + \Im[FT[I(x', y')](p', q')]$ and the best fitted theoretical curves from Equation 3.33 is shown on the right.

$SNR_{max} \geq 6$, which shows the least false positive detection. The graphs between the simulated and predicted values of SNR_{max}, inclination angles and streak positions shown in Figures 3.14a, 3.14b and 3.14c, respectively also support the conclusion derived from the ROC curve.

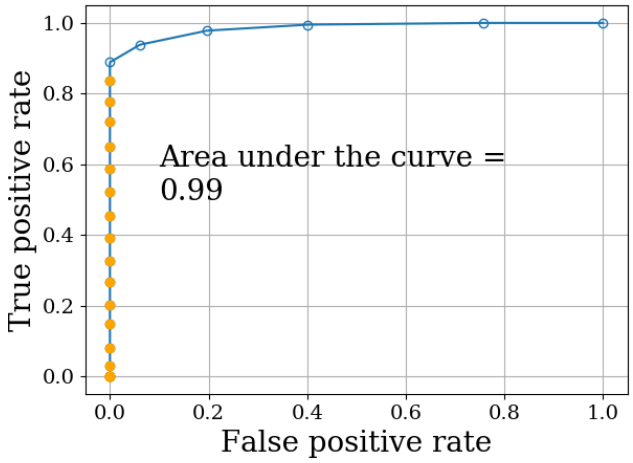

Figure 3.13: ROC curve for predicting SNR_{max} in the Fourier space. The filled circles represent the TPR vs FPR values for $SNR_{max} > 6$.

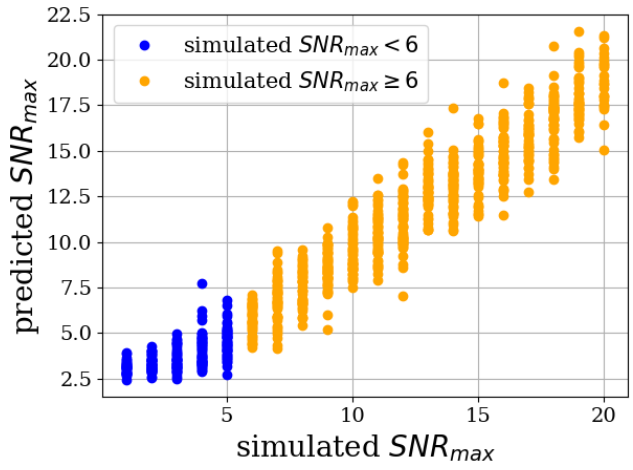

(a)

Figure 3.14: Comparison of input SNR_{max}, inclination angle (θ) and position of the streaks along the columns in the synthetic image with their corresponding estimated values from the streak detection in the Fourier space. (cont.)

.

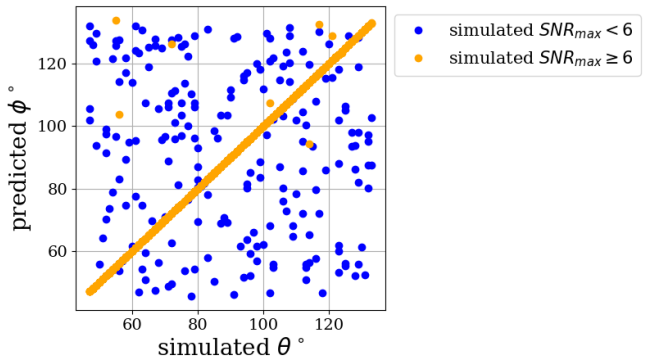

(b)

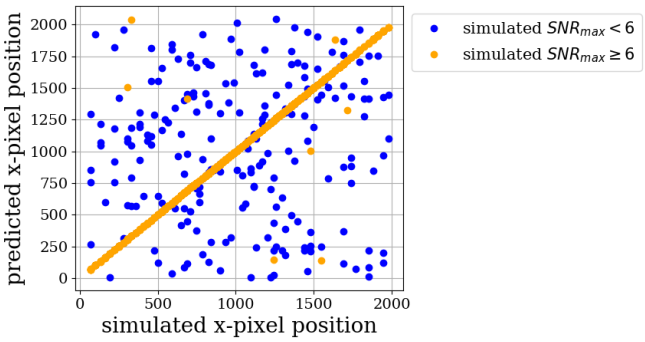

(c)

Figure 3.14: Comparison of simulated SNR_{max}, $FWHM$, inclination angle (θ) and position of the streaks along the columns in the synthetic image with their corresponding estimated values from the streak detection in the Fourier space.

3.3 Streak contrast enhancement in the wavelet domain

3.3.1 Wavelet transformation

One of the approaches to validate the streak detection can also be achieved by increasing the contrast of the CCD frames, so that the invisible streaks become visible to the naked eye. The discrete wavelet transform (DWT) has been recognized as a powerful digital-image-processing tool for image enhancement in recent years. The wavelet transform is defined as follows,

$$W_k^j = \int f(x)\psi\left(\frac{x}{2^j} - k\right)\, dx, \tag{3.34}$$

where ψ is the transforming function and is called the mother wavelet, $f(x)$ is the original signal (Tsai and Lee, 2004). The indices j and k are scale and translation parameters, respectively. Bi-orthogonal wavelets can be considered as a good choice to detect edges in an image (Prasad et al., 2016). So, in the current analysis we have considered the bi-orthogonal wavelet to perform all the operations.

In 2-D DWT, a filter bank is used composed of a mother wavelet (ψ) as well as a scaling filter (Ψ) acting as high-pass and low-pass filters, respectively. The high-pass filter preserves the finer details of the image, whereas the low pass filter gives a coarse approximation of the image. The 2-D DWT is then estimated by performing high-pass and low-pass filtering on the image pixels along the rows and columns. The output at the end of each filtering is down-sampled by a factor 2 ($\downarrow 2$). The filtering separates an image into wavelet high frequency components along the horizontal (${W^1}_H$), vertical (${W^1}_V$) and diagonal (${W^1}_D$) directions as well as a low frequency low resolution approximation of the image (S^1) as shown in Figure 3.15.

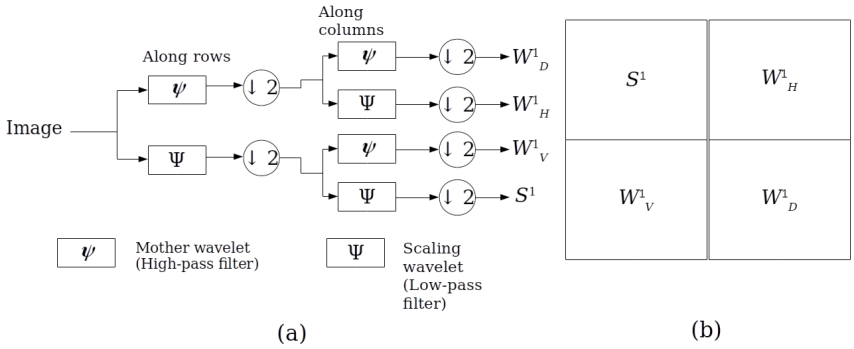

Figure 3.15: Diagrams of 2D DWT image decomposition (Hsia et al., 2011). (a) DWT image decomposition process, (b) decomposed DWT components. The notation of ($\downarrow 2$) refers to down-sampling of the output coefficients by a factor two.

This process can also be repeated on the low resolution approximations to compute multiple wavelet decomposition at different scales (j). Figure 3.16 shows a layer representation of the 2D DWT for an image. ${W^j}_H$, ${W^j}_V$, ${W^j}_D$ represent the detailed components in the vertical, horizontal and diagonal directions at level j, respectively. S^j refers to the scaling approximation of the image at level j. A level 2 decomposition of a gray-scale image is shown in Figure 3.17.

If an image is decomposed to level j, level 1 contains the component of the highest frequency inherent to the image, and level j contains the component of low frequency inherent to the image. The conventional image enhancement techniques take a DWT of an image, modify the DWT coefficients and transform back the coefficients.

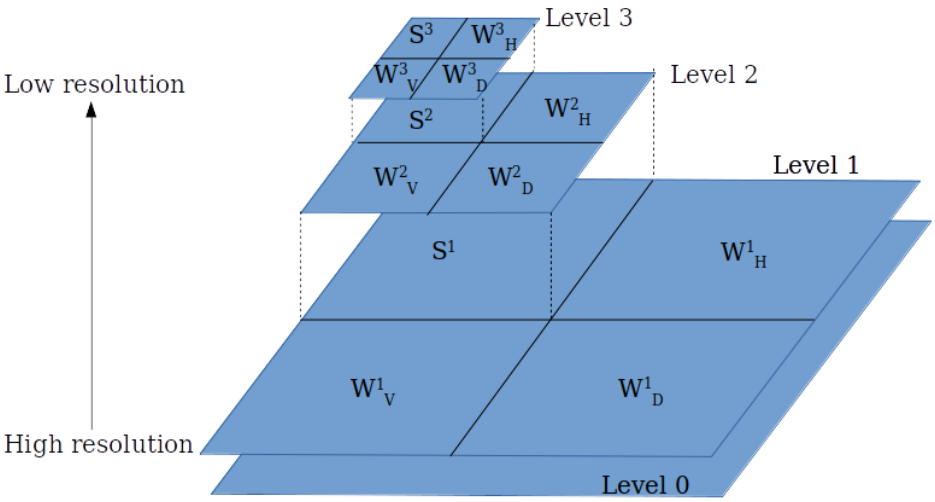

Figure 3.16: Layer presentation of 2-D wavelet transform (Tsai and Lee, 2004).

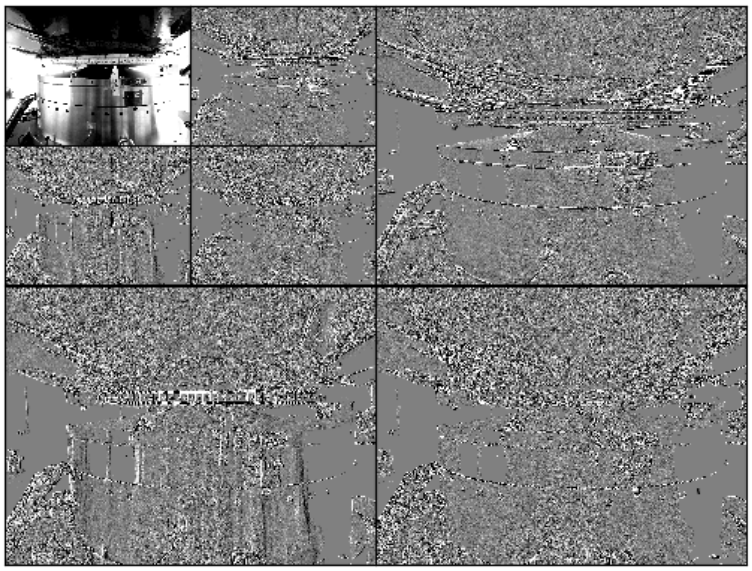

Figure 3.17: 2-D wavelet transform of an image up-to two levels using bi-orthogonal wavelets. The test image used here is a gray scale image of the 4-m ILMT air-bearing.

3.3.2 Contrast enhancement

After multi level wavelet transformation, a thresholding is applied to the wavelet coefficients to reduce the noise and then modified according to a weighing scheme. This operation results in contrast enhancement of the low frequency component of the image. The flow diagram of this method is shown in Figure 3.18.

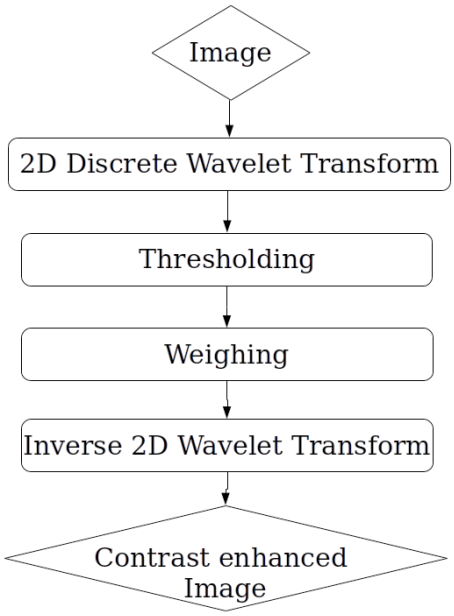

Figure 3.18: Flow chart of contrast enhancement using 2D discrete wavelet transform.

In the wavelet domain, the actual signal is coherent and concentrated within a few coefficients having high amplitudes. But the incoherent noise is represented by a higher number of coefficients with smaller amplitudes. Thus the noise can be suppressed by applying a threshold to the wavelet coefficients. In our analysis we have applied the level dependent thresholds (Johnstone and Silverman, 1997) $\lambda_j = \sigma_j \sqrt{2log_2 N_j}$, where N_j is the length of the j^{th} detailed component and σ_j is an estimate of the r.m.s. noise at level j. Then a soft thresholding (Donoho and M. Johnstone, 1999) function described below is applied to the wavelet coefficients to reduce the noise:

$$W^j_{out}(m,n) = \begin{cases} W^j_{in}(m,n) - \lambda_j & \text{if } W^j_{in}(m,n) \geq \lambda_j \\ W^j_{in}(m,n) + \lambda_j & \text{if } W^j_{in}(m,n) \leq \lambda_j \\ 0 & \text{if } |W^j_{in}(m,n)| < \lambda_j, \end{cases}$$

where $W^j_{in}(m,n)$ and $W^j_{out}(m,n)$ are the wavelet coefficients of level j at position (m,n) before and after thresholding, respectively.

The faint streaks in the simulated frames produce the low frequency components in the wavelet domain. So, in the weighing scheme, the DWT coefficients at the highest level containing the low frequency coefficients are enhanced more than the subsequent lower level coefficients. The scaling coefficients at the highest level are not manipulated to prevent image distortion.

The wavelet coefficients after thresholding, i.e. $W^j_{out}(m,n)$ are weighed as

$$\widehat{W}^j_{out}(m,n) = \exp(j - j_{max}) \cdot W^j_{in}(m,n), \tag{3.35}$$

where $\widehat{W}^j_{out}(m,n)$ is the coefficient after weighing and j_{max} is the maximum decomposition level. Figure 3.19 shows a synthesized CCD frame and its processed frame.

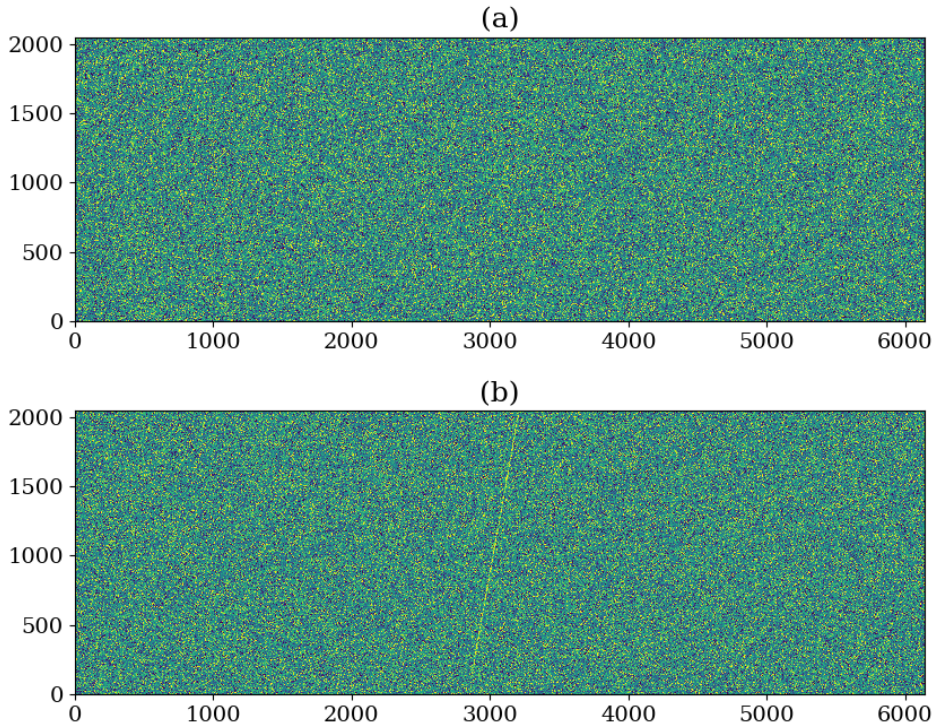

Figure 3.19: (a) Synthesized CCD frame containing an invisible streak having a SNR_{max} of 25 with an inclination angle ϕ of 80°, (b) Processed image using the wavelet denoising technique

Wavelet based denoising can further be improved, thanks to the translation-invariant denoising proposed by Coifman and Donoho (1995). The orthogonal wavelet transform of an image is not translation invariant. It means that a shifted version of the image undergoing denoising may give a different result. The wavelet based denoiser can be made translation invariant by making several shifted copies of the image, then perform denoising, shift back the

image and at the end, take an average of all the results. We have adapted this procedure and asserted its superior performance than the conventional denoising (see Figure 3.20). Several synthetic frames having streaks of different SNR_{max} are denoised using both techniques. A Normalized-Mean-Square-Error (NMSE) is calculated for each case as follows,

$$\text{NMSE} = \frac{\frac{1}{n}\sum_{i=1}^{n}(I_{o_i} - I_{dn_i})^2}{max(I_o)},$$

where, I_o and I_{dn} are the noise free image and denoised image, respectively each having n number of pixels. The normalization factor $max(I_o)$ is the maximum pixel value present in the noise free image.

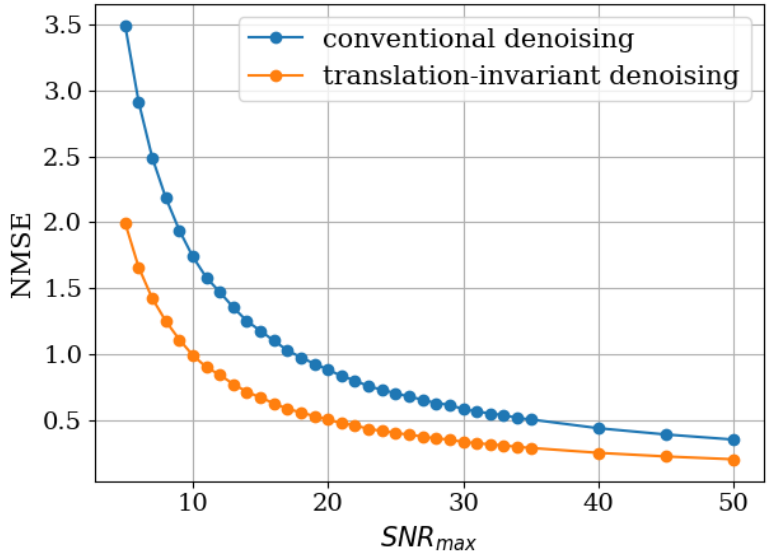

Figure 3.20: Comparison between conventional denoising and translation invariant denoising. The $FWHM$ and ϕ of all streaks are kept fixed 5 pixels and 80°, respectively.

Looking at Figure 3.20, there is a sharp rise in NMSE for $SNR_{max} \leq 10$. At this transition only 35% fraction of the denoised streaks could be visually detected and the visual detection probability is expected to decrease further for fainter streaks. This implies that the proposed technique becomes inefficient for streaks having $SNR_{max} \leq 10$. We have also analysed the effect of denoising on the automatic streak detection performance, by applying the method described in Section 3.2 to several denoised frames. The respective ROC curve is estimated and compared to the curve previously shown in Figure 3.13. The AUC estimations for both curves suggest that, wavelet

based denoising has hardly any effect on the automatic streak detection capability (see Figure 3.21).

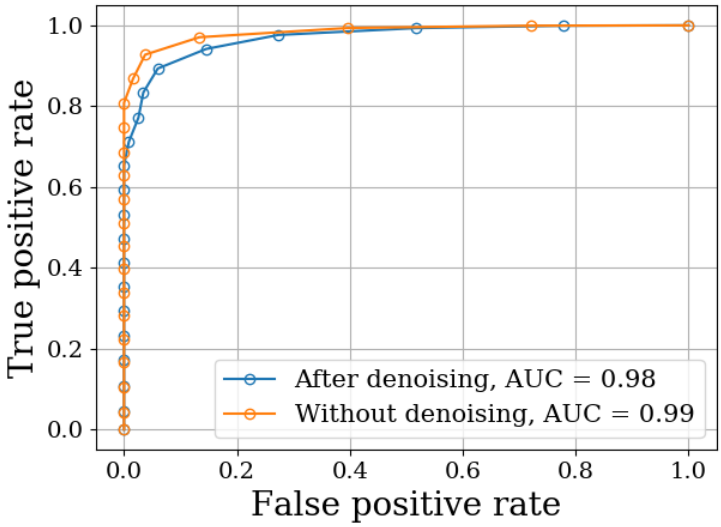

Figure 3.21: A comparison between the ROC curves predicting the streak detection in noisy and wavelet based denoised frames.

3.4 Other detection techniques for detecting debris streaks

3.4.1 Hough transformation

The basics of the Hough transformation is to find connected pixels in an image which create a line of a particular shape. Generally this technique is used on binary preprocessed images which are themselves the products of the application of an edge detection algorithm. The purpose of the edge detection algorithm is to highlight sharp features in an image due to the presence of an intensity gradient. Singh and Datar, 2013 have shown that the 'Canny edge detection' algorithm (Canny, 1986) along with the Hough transformation works better in noisy images than many other detection techniques. Bhawna and Shukla, 2011; Sona et al., 2017 have also demonstrated that the Canny edge detection technique followed by Hough transformation is very effective in detecting features of different shapes in a gray scale digital image. The Canny edge detector algorithm is as follows :

- Gaussian smoothing : A Gaussian filter is convolved with the image to remove any spurious noise (e.g. cosmic ray hits, bad pixels, etc.). In

our case, a filter size of 5×5 pixels with the standard deviation of the Gaussian profile being 1.5 pixels was used.

- Intensity gradient estimation of the image : The smoothed image is then filtered with a Sobel kernel to estimate the first derivative at each pixel which represents a pixel intensity variation (see Sobel and Feldman 1968 to know the details about the Sobel operator).

- Non-maximum suppression : After the intensity gradient magnitude and direction from the previous step are obtained, the whole image is scanned to remove any unwanted pixel that does not belong to the edge. It is done by comparing each pixel with its neighbouring pixels along the gradient direction. If the pixel forms a local maximum, it is kept for the next step, otherwise set to zero. A binary image is obtained at the end of this step.

- Hysteresis thresholding : This stage distinguishes between the real edges and the false ones which are discarded subsequently. This is done by setting an upper and a lower threshold values. Pixel values higher than the upper threshold are kept and the pixels below the lower threshold are discarded. The values falling between both thresholds are verified as a real edge or not, based on their connectivity. We have considered the upper threshold to be 0.6 times the maximum pixel value in the image after smoothing and the lower threshold is kept at 0.5 times that of the upper threshold value.

We are interested in detecting the debris streak, which is a set of adjacent parallel straight lines. The straight line can be represented in parametric form as,

$$\rho = x \sin\theta + y \cos\theta, \tag{3.36}$$

where x and y are pixel indexes along the CCD columns and CCD rows, respectively. ρ is the distance of the line from the origin and θ is the inclination angle of the line with respect to the CCD columns (see Figure 3.22). Hence, each point (x, y) on the straight line in the real image can be converted into the (ρ, θ) space, also known as the Hough-space. The transformation of (x, y) to the (ρ, θ) space is regarded as the Hough transformation. The location of the peak in the (ρ, θ) space determines the location and orientation of the streak. Figure 3.23 demonstrates the algorithm applied to a simulated CCD frame. We have found out that, this technique becomes inefficient for fainter streaks (i.e. $SNR_{max} \leq 50$) and also takes enormous computation time for 4K×4K pixels images.

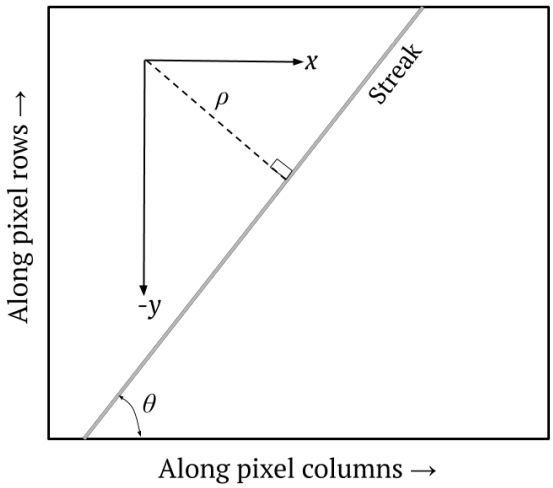

Figure 3.22: Representation of a straight line on a CCD plane.

3.4.2 Radon transformation

Integrating all pixel values along all possible lines in an image is called the Radon transform, where each point in the Radon-space represents the sum of the pixels in the original image along a line with a particular slope and intercept (Radon, 1917; Radon, 1986). The Hough transform and the Radon transform are mathematically equivalent when applied to gray-scale images (Illingworth and Kittler, 1988). However, there exits a faster way to perform the Radon transform in the Fourier space using the Fourier Slice Theorem (Bracewell, 1956). Hickson (2018) has demonstrated that the Radon transform in the Fourier space can be used to detect faint debris streaks in optical astronomical images. Figure 3.24 shows the Radon transform of the CCD image shown in Figure 3.23(a). We have used this method to detect the debris streaks on several simulated CCD images. All the streaks with $SNR_{max} > 15$ were successfully detected, but the success rate of the detection started decreasing for fainter streaks. In fact, less than half of the streaks with $SNR_{max} = 10$ could be detected successfully. Hence, we did not implement this approach to detect faint debris streaks.

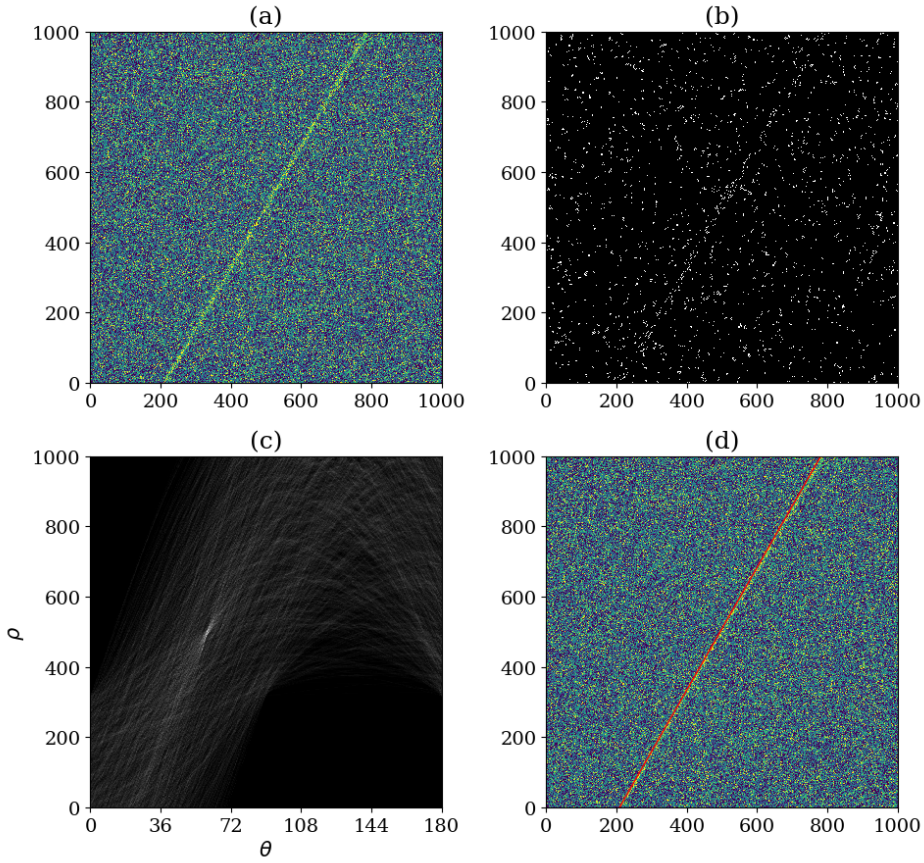

Figure 3.23:
(a) 1000×1000 CCD image with a synthetic streak having $SNR_{max} = 100$, $FWHM = 9$ pixels, inclined at 60° with respect to the CCD columns.
(b) Canny edge detector output.
(c) Hough space obtained from the Hough transformation performed on the output of the Canny edge detector
(d) The detected trajectory of the streak from Hough transformation, plotted over the original image.

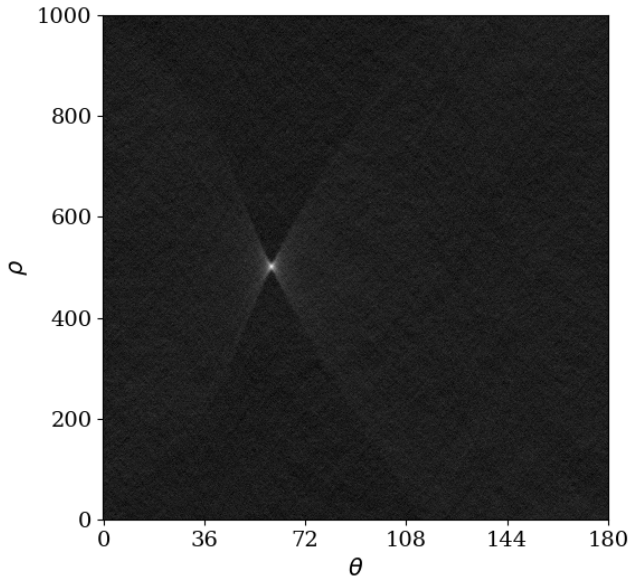

Figure 3.24: Radon transformation of the CCD image shown in Fig. 3.23(a).

3.5 Image subtraction

If a CCD image contains background sources other than the streak due to the presence of stars, galaxies, etc., then the streak detection techniques discussed above may not work optimally due to contamination. Image subtraction is an effective way to remove all the invariable background sources. When the same region of the sky is scanned several times, then a high signal to noise frame can be constructed by co-adding all the best seeing individual CCD frames. This frame can be considered as a reference image. After making adjustments for the seeing, background level and intensity variations to the reference image, it is ready to be subtracted from the individual frames. This particular method is called difference image analysis (DIA). Bramich (2008) has proposed a very efficient image subtraction technique known as 'DanDia' which uses a discrete convolution kernel to perform DIA.

3.5.1 DanDia algorithm

Let us consider the following model for a given pixel:

$$M_{ij} = (R \circledast K)_{ij} + B_0, \tag{3.37}$$

where R is the reference image, i and j are pixel indices, K is the convolution kernel and B_0 is an assumed constant background value.

By noting that the convolution here is a discrete operation, we can rewrite Equation 3.37 as,

$$M_{ij} = \sum_{lm} K_{lm} R_{ij}^{lm} + B_0, \tag{3.38}$$

where $R_{ij}^{lm} = R_{(i+l)(j+m)}$.

In order to optimize the kernel, we will consider the following linear least-squares problem:

$$\begin{aligned} \chi^2 &= \sum_{ij} \left(\frac{I_{ij} - M_{ij}}{\sigma_{ij}} \right)^2, \\ &= \sum_{ij} \left(\frac{r_{ij}}{\sigma_{ij}} \right)^2, \end{aligned} \tag{3.39}$$

where I is the image we want to fit from the reference image and σ_{ij} is the noise associated with pixel i, j.

In order to minimize the χ^2, we must have $\nabla\chi^2 = \vec{0}$. So, by taking the partial derivatives with respect to $K_{l'm'}$ and B_0, we will have:

$$\begin{aligned}\frac{\partial\chi^2}{\partial K_{l'm'}} &= 2\sum_{ij}\frac{r_{ij}}{\sigma_{ij}^2}\frac{\partial r_{ij}}{\partial K_{l'm'}} \\ &= -2\sum_{ij}\frac{r_{ij}}{\sigma_{ij}^2}\frac{\partial M_{ij}}{\partial K_{l'm'}} \\ &= -2\sum_{ij}\frac{r_{ij}}{\sigma_{ij}^2}R_{ij}^{l'm'} \\ &= -2\sum_{ij}\frac{I_{ij}R_{ij}^{l'm'}}{\sigma_{ij}^2} + 2\sum_{lm}\sum_{ij}\frac{R_{ij}^{lm}R_{ij}^{l'm'}}{\sigma_{ij}^2}K_{lm} + 2\sum_{ij}\frac{R_{ij}^{l'm'}}{\sigma_{ij}^2}B_0,\end{aligned} \tag{3.40}$$

$$\begin{aligned}\frac{\partial\chi^2}{\partial B_0} &= -2\sum_{ij}\frac{r_{ij}}{\sigma_{ij}^2}\frac{\partial M_{ij}}{\partial B_0} \\ &= -2\sum_{ij}\frac{r_{ij}}{\sigma_{ij}^2} \\ &= -2\sum_{ij}\frac{I_{ij}}{\sigma_{ij}^2} + 2\sum_{lm}\sum_{ij}\frac{R_{ij}^{lm}}{\sigma_{ij}^2}K_{lm}, +2\sum_{ij}\frac{1}{\sigma_{ij}^2}B_0.\end{aligned} \tag{3.41}$$

Setting these derivatives equal to zero and rearranging leads to

$$\begin{aligned}\sum_{lm}\sum_{ij}\frac{R_{ij}^{lm}R_{ij}^{l'm'}}{\sigma_{ij}^2}K_{lm} + \sum_{ij}\frac{R_{ij}^{l'm'}}{\sigma_{ij}^2}B_0 &= \sum_{ij}\frac{I_{ij}R_{ij}^{l'm'}}{\sigma_{ij}^2}, \\ \sum_{lm}\sum_{ij}\frac{R_{ij}^{lm}}{\sigma_{ij}^2}K_{lm} + \sum_{ij}\frac{1}{\sigma_{ij}^2}B_0 &= \sum_{ij}\frac{I_{ij}}{\sigma_{ij}^2}.\end{aligned} \tag{3.42}$$

The expression above is a system of linear equations that can be represented in matrix form. Considering the kernel with dimensions $-L \leq l \leq L$ and $-M \leq m \leq M$;

$$A\mathbf{x} = \mathbf{b}$$

where

$$A = \sum_{ij} \begin{bmatrix} \frac{(R_{ij}^{-L-M})^2}{\sigma_{ij}^2} & \cdots & \frac{R_{ij}^{-L-M} R_{ij}^{00}}{\sigma_{ij}^2} & \cdots & \frac{R_{ij}^{-L-M} R_{ij}^{LM}}{\sigma_{ij}^2} & \frac{R_{ij}^{-L-M}}{\sigma_{ij}^2} \\ \vdots & & \vdots & & \vdots & \vdots \\ \frac{R_{ij}^{00} R_{ij}^{-L-M}}{\sigma_{ij}^2} & \cdots & \frac{(R_{ij}^{00})^2}{\sigma_{ij}^2} & \cdots & \frac{R_{ij}^{00} R_{ij}^{LM}}{\sigma_{ij}^2} & \frac{R_{ij}^{00}}{\sigma_{ij}^2} \\ \vdots & & \vdots & & \vdots & \vdots \\ \frac{R_{ij}^{LM} R_{ij}^{-L-M}}{\sigma_{ij}^2} & \cdots & \frac{R_{ij}^{LM} R_{ij}^{00}}{\sigma_{ij}^2} & \cdots & \frac{(R_{ij}^{LM})^2}{\sigma_{ij}^2} & \frac{R_{ij}^{LM}}{\sigma_{ij}^2} \\ \frac{R_{ij}^{-L-M}}{\sigma_{ij}^2} & \cdots & \frac{R_{ij}^{00}}{\sigma_{ij}^2} & \cdots & \frac{R_{ij}^{LM}}{\sigma_{ij}^2} & \frac{1}{\sigma_{ij}^2} \end{bmatrix}, \tag{3.43}$$

$$\mathbf{x} = \begin{bmatrix} K_{-L-M} \\ \vdots \\ K_{00} \\ \vdots \\ K_{LM} \\ B_0 \end{bmatrix}, \tag{3.44}$$

and

$$\mathbf{b} = \sum_{ij} \begin{bmatrix} \frac{I_{ij} R_{ij}^{-L-M}}{\sigma_{ij}^2} \\ \vdots \\ \frac{I_{ij} R_{ij}^{00}}{\sigma_{ij}^2} \\ \vdots \\ \frac{I_{ij} R_{ij}^{LM}}{\sigma_{ij}^2} \\ \frac{I_{ij}}{\sigma_{ij}^2} \end{bmatrix}. \tag{3.45}$$

These matrices can also be represented in terms of the Jacobian matrix system $J^T W J\ \mathbf{x} = J^T W \mathbf{I}$, where

$$J = \begin{bmatrix} R_{00}^{-L-M} & \cdots & R_{00}^{00} & \cdots & R_{00}^{LM} & 1 \\ \vdots & & \vdots & & \vdots & \vdots \\ R_{ij}^{-L-M} & \cdots & R_{ij}^{00} & \cdots & R_{ij}^{LM} & 1 \\ \vdots & & \vdots & & \vdots & \vdots \\ R_{IJ}^{-L-M} & \cdots & R_{IJ}^{00} & \cdots & R_{IJ}^{LM} & 1 \end{bmatrix} \tag{3.46}$$

is the Jacobian matrix,

$$W = \begin{bmatrix} \frac{1}{\sigma_{00}^2} & \cdots & 0 & \cdots & 0 \\ \vdots & \ddots & \vdots & \ddots & \vdots \\ 0 & \cdots & \frac{1}{\sigma_{ij}^2} & \cdots & 0 \\ \vdots & \ddots & \vdots & \ddots & \vdots \\ 0 & \cdots & 0 & \cdots & \frac{1}{\sigma_{IJ}^2} \end{bmatrix} \tag{3.47}$$

is the weight matrix and

$$\mathbf{I} = \begin{bmatrix} I_{00} \\ \vdots \\ I_{ij} \\ \vdots \\ I_{IJ} \end{bmatrix} \tag{3.48}$$

is the image matrix. Finally the solution $\mathbf{x}$ will be given by

$$\mathbf{x} = (J^T W J)^{-1} J^T W \mathbf{I}. \tag{3.49}$$

$(J^T W J)$ is a positive-definite and Hermitian matrix, so its inverse can be determined using a Cholesky decomposition for numerical efficiency.

3.5.2 The noise model

Considering the following model for pixel i, j of a raw image:

$$X_{ij} = B + g(Y_{ij}) \tag{3.50}$$

where

- B is the associated master bias,
- Y_{ij} is the pixel value obtained from the following model,

  $$Y_{ij} = D_{ij} + F_{ij} M_{ij} \ ,$$

- D_{ij} is the associated master dark pixel (scaled by exposure time),
- F_{ij} is the associated normalized master flat field pixel (considered as noiseless since it should have a high S/N),
- M_{ij} is the model for the calibrated image pixel,
- g is a given non-linearity relationship for the CCD

  i.e, $g(Y) = aY^3 + bY^2 + cY + d$,

we can represent the noise within a pixel by:

$$\begin{aligned}\sigma^2_{X_{ij}} &= \sigma^2_0 + \sigma^2_{g(Y_{ij})},\\ &= \sigma^2_0 + \left(\frac{\partial g(Y_{ij})}{\partial Y_{ij}}\sigma_{Y_{ij}}\right)^2,\end{aligned} \tag{3.51}$$

where σ^2_0 is the CCD readout noise.

If we set $H_{ij} = \frac{\partial g(Y_{ij})}{\partial Y_{ij}}$ and since $\sigma^2_{Y_{ij}}$ obeys the laws of Poissonian statistics, we have $\sigma^2_{Y_{ij}} = Y_{ij}$ and so:

$$\sigma^2_{X_{ij}} = \sigma^2_0 + H^2_{ij} Y_{ij}. \tag{3.52}$$

The model for the raw image pixel can be inverted to yield the model for the calibrated image pixel as follows:

$$\begin{aligned}X_{ij} &= B + g(D_{ij} + F_{ij}M_{ij}) \text{ , from Eq. 3.50}\\ X_{ij} - B &= g(D_{ij} + F_{ij}M_{ij}),\\ g^{-1}(X_{ij} - B) &= D_{ij} + F_{ij}M_{ij},\\ \frac{g^{-1}(X_{ij} - B) - D_{ij}}{F_{ij}} &= M_{ij}.\end{aligned} \tag{3.53}$$

Noise propagation of $\sigma^2_{X_{ij}}$ (Eq. 3.52) using the relationship between X_{ij} and M_{ij} (Eq. 3.53), yields the standard CCD noise model for $\sigma^2_{M_{ij}}$ in the following way:

$$\begin{aligned}\sigma^2_{M_{ij}} &= \left(\frac{\sigma_{g^{-1}(X_{ij}-B)}}{F_{ij}}\right)^2,\\ &= \frac{1}{F^2_{ij}}\left(\frac{\partial g^{-1}(X_{ij} - B)}{\partial X_{ij} - B}\sigma_{X_{ij}}\right)^2.\end{aligned} \tag{3.54}$$

By noting that $Y_{ij} = g^{-1}(X_{ij} - B)$ and that $g(Y_{ij}) = X_{ij} - B$, we have $\frac{\partial g^{-1}(X_{ij}-B)}{\partial X_{ij}-B} = \frac{\partial Y_{ij}}{\partial g(Y_{ij})} = \frac{1}{H_{ij}}$, and thus

$$\begin{aligned}\sigma^2_{M_{ij}} &= \frac{\sigma^2_{X_{ij}}}{H^2_{ij}F^2_{ij}},\\ &= \frac{\sigma^2_0 + H^2_{ij}Y^2_{ij}}{H^2_{ij}F^2_{ij}},\\ &= \frac{\sigma^2_0}{H^2_{ij}F^2_{ij}} + \frac{Y_{ij}}{F^2_{ij}},\\ &= \frac{\sigma^2_0}{H^2_{ij}F^2_{ij}} + \frac{D_{ij} + F_{ij}M_{ij}}{F^2_{ij}}.\end{aligned} \tag{3.55}$$

It is to be noted that the pixel variance $\sigma^2_{M_{ij}}$ depends on the image model M_{ij} and hence both can be fitted iteratively. During the initial guess to derive $\sigma^2_{M_{ij}}$, we have set M_{ij} as the reference image $R_{i,j}$. In the next iterations, 3σ clipping has been used to remove outlier pixel values. The clipping is done at the end of each iteration, by creating a normalized residual image ($nr_{ij} = |(I_{ij} - M_{ij})/\sigma_{ij}|$) for all pixel values and any pixel having $nr_{ij} > 3$ is ignored in the subsequent iteration.

3.5.3 Algorithm demonstration

For illustration purpose, a background image has been simulated on a 50×50 grid using Equation 3.50 considering a linear CCD response, uniform flat field, unit CCD gain and a read out noise of $10e^-$. Then a reference image was constructed by generating 3 Gaussian point spread functions (PSF) on the background image with a *FWHM* of 4 pixels and signal-to-noise ratios of 12, 18 and 20. A target image was also created in a similar fashion but with a broader *FWHM* (= 5 pixels). The DanDia algorithm discussed in the previous subsection was applied and the residual image, convolution kernel and the difference background were estimated (see Figure 3.25). The implementation of the algorithm on archived real observations of a Type Ib supernova (PS15bgt, Djupvik and Andersen, 2010) also confirms its efficiency (see Figure 3.26).

Image alignment

In astronomical observations, the field of view in each CCD frame taken with a certain telescope set up may not remain necessarily the same based on various factors, for instance, inaccurate telescope pointing model, telescope flexure, instrument flexure, change in focal length due to temperature changes, etc. For an efficient DIA application, all the images should be perfectly aligned. In TDI images, the relative angular velocity of the passing stellar objects will change in case of a slight change in the focal length of the telescope which introduces an extra amount of complexity while trying to align the images. Images taken with the 4-m ILMT will be naturally perfectly aligned as there will be no change in the telescope structure and TDI rate. But during the observations with the DFOT, the pointing of the telescope towards zenith was not constant and the TDI rate also was varied in order to compensate for the focal length variation from one night to another.

The usual way to deal with such a problem is first to make astrometry of all the images (i.e., mapping physical coordinates to the world coordinate system [WCS]). One can then correlate each image and apply the geometric transformations (such as translation, rotation or scaling) in order to recover a same field of view with a same pixel scale. This process is called ‘image

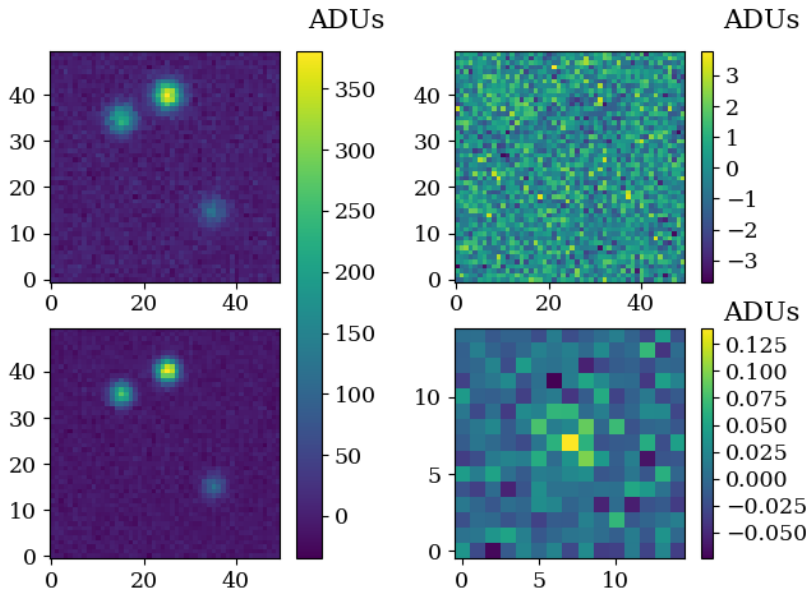

Figure 3.25: Demonstration of the DanDia algorithm: The images on the upper left and lower left are the target image and the reference image. The residual image is displayed on the upper right and the convolution kernel is displayed on the lower right. The difference background B_0 is estimated to be 1.1 ADUs.

registration'. We have implemented our own python interface to well known software SCAMP (Bertin, 2006) and SWARP (Bertin et al., 2002) for an efficient astronomical image registration.

We have considered two TDI images taken with the same filter ($\sim$ SDSS i') which have got the best overlapping region for further demonstration. The first image was acquired on 17^{th} of May 2015 with starting exposure time 20h23m27s (UT) and the second image was acquired on 22^{nd} of May 2015 with the beginning of its exposure at 20h24m27s (UT). The declination at the epoch of observation (J2015.4) corresponding to the center of the 1st image and 2nd image differs by $\sim$ 32 arc-seconds. The 1st image also happens to have the faintest streak observed corresponding to the debris no 13 (refer to Figure 2.13 and Table 2.2). In Figure 3.27, the difference in the centroids of the sources detected in both frames are shown. The difference along the x-pixel positions (Δx) shows a gradient due to separate TDI rates used for both frames. The read out rates were 44.254 and 44.383 CCD rows per second for the 1st and 2nd image, respectively. The plots corresponding to Δy suggest that the strange gradient present in Δy is because of an instability in the telescope pointing possibly due to temporary telescope flexures.

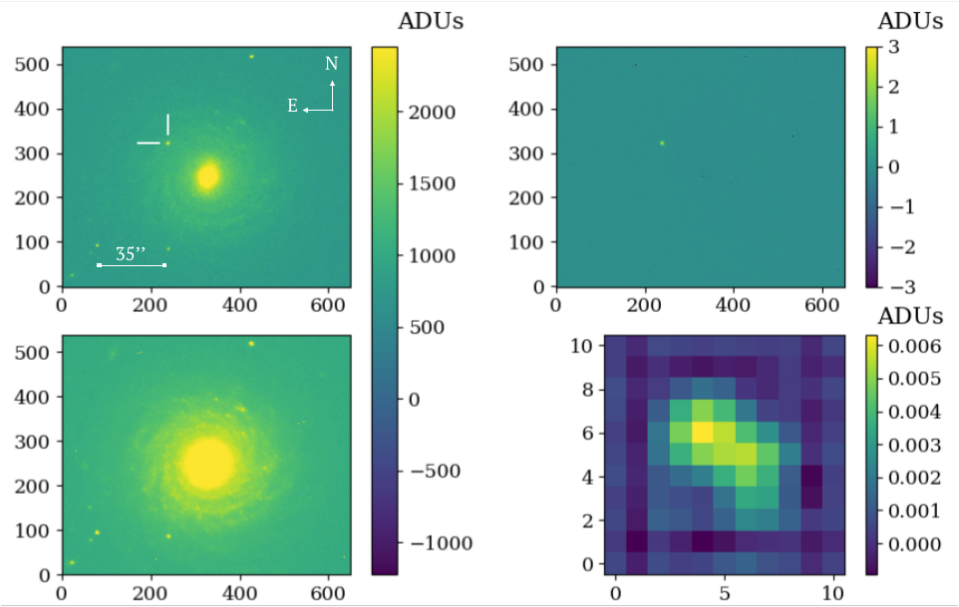

Figure 3.26: DanDia algorithm applied to NGC 7371 during a supernova event (PS15bgt): The images on the upper left and lower left are the target image (with a supernova) and the reference image (without any supernova). The residual image is displayed on the upper right and the convolution kernel is displayed on the lower right. The reference and the target images displayed are centered at ra = 22h 46m 4s and dec = -11° 00' 4".

A segment of the 1st image containing the faintest streak is now considered as the target image and its overlapping region in the 2nd image is then taken as the reference image for the image registration (see Figure 3.28). After running SCAMP and SWARP through both the image slices, we could improve their alignment to within 1 pixel (see the plots in Figure 3.29).

As both the image segments are aligned, they are ready for the difference image analysis to be applied. The discrete convolution kernel (i.e., K_{lm} from Equation 3.42) is constructed from the linear least squares fitting of the reference image to the target image. So, an image with a larger number of sources will approximate a better kernel solution. During TDI observations with the 4m ILMT, a certain portion of the acquired frames will be recorded at high galactic latitude and hence the imaged fields will have comparatively sparse stellar population. The same situation can be seen in the images shown in Figure 3.28. We have developed a procedure that allows us to determine a better convolution kernel even for astronomical images with few

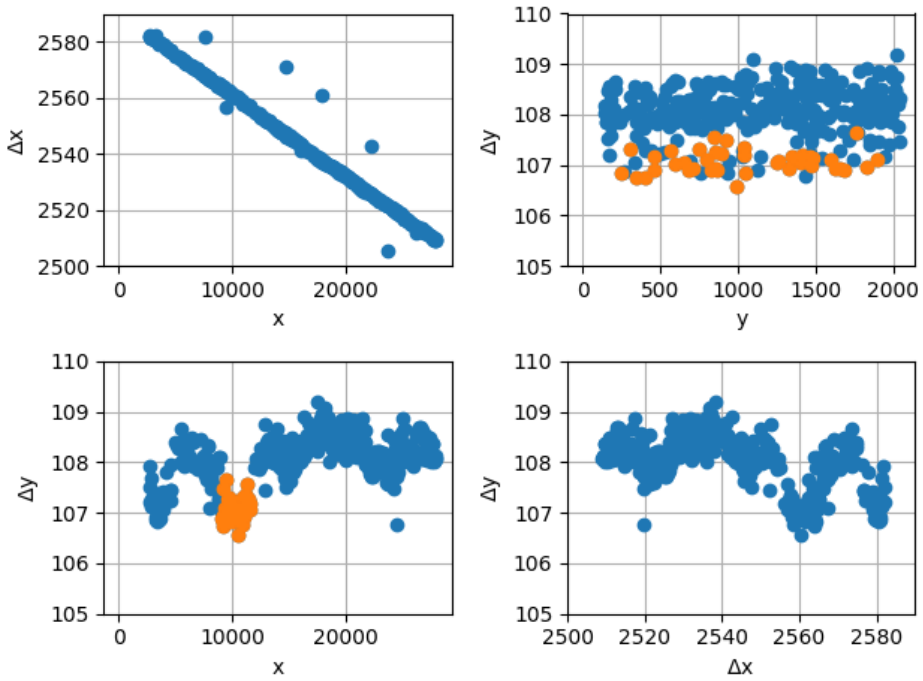

Figure 3.27: Analysis of the astrometric positions of the detected sources in two different TDI frames not perfectly aligned to each other: Δx is the difference in the centroids of the detected sources along the x axis or the CCD column. Δy is the difference in the centroids of the detected sources along the y axis or the CCD row. The scatter plots in orange color seen in the upper-right and lower-left subplots belong to the sources detected between the readout of CCD row number 9000 and 12000. The telescope had probably undergone some transient mechanical flexure during this period due to heavy wind flow or any other unknown cause.

stars. Both the target and reference images should be properly background subtracted, registered and aligned for this approach to be effective. At first, based on the astrometric and photometric information, bright sources are chosen which are common to both images. A fixed region around the selected sources are then copied and joined together to form a new image (see Figure 3.30). These new set of images with a high stellar density can then be used to construct a better kernel solution. After applying DanDia to the newly formed high stellar population images, we see that the normalized residuals in Figure 3.30 still do not look optimal. This is due to the fact that the reference image has neither sharper PSF profiles nor higher signal-to-noise ratio sources compared to those of the target image. Another factor is the TDI distortion, which arises due to the absence of an optical corrector for

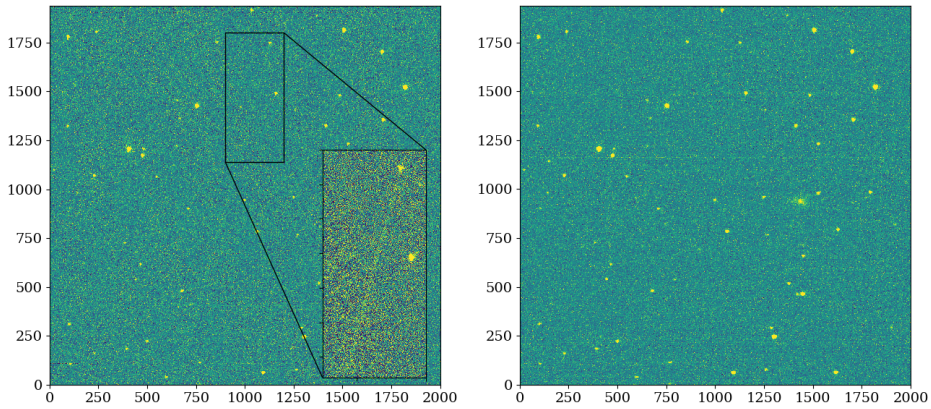

Figure 3.28: Sub-images selected from two different TDI frames having a common field of view. The image on the left has been considered as the target image and the right one is considered as the reference image for DIA. A certain portion of the target image is zoomed which shows a faint streak.

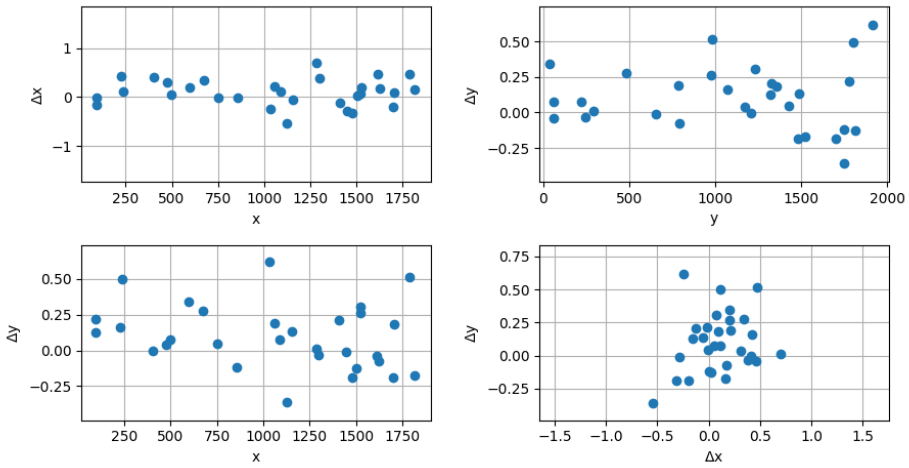

Figure 3.29: Analysis of the astrometric positions of the detected sources from two different TDI frames aligned with respect to each other: Δx is the difference between the centroids of the detected sources along the CCD column. Δy is the difference between the centroids of the detected sources along the CCD row.

DFOT. Without the optical corrector, the shape of the PSFs changes along the declination due to a gradient in their angular velocities. By looking at the images (c) and (d) in Figure 3.30, one can say that the target image has got sharper PSFs. So we have repeated our analysis by exchanging the target image for the reference image and vice versa. We have also tried to take the

sources along a constant declination so that the PSF profile does not change significantly. The results of this analysis are shown in Figure 3.31. We can now clearly see that the residual images look better.

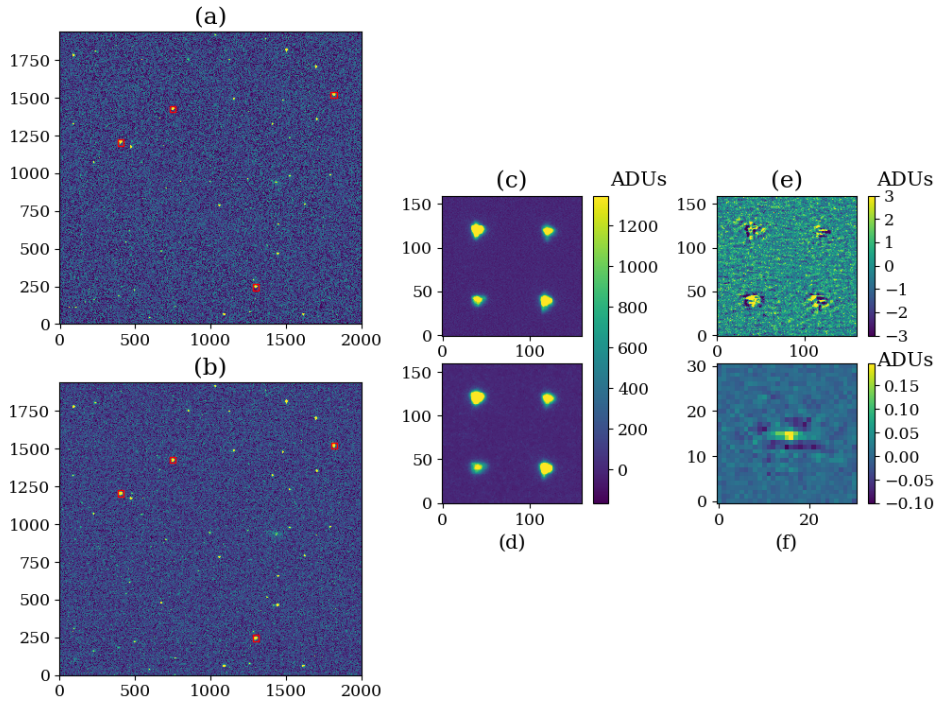

Figure 3.30: Construction of a dense stellar image out of a sparse field image in order to apply the difference image analysis. Images (a) and (b) are the target and reference image, respectively. The small red squares on these images are highlighting the sources selected for constructing the dense stellar field images (c) and (d) from (a) and (b), respectively. Image (e) shows the normalized residuals and Image (f) shows the kernel solution.

The target image shown in Figure 3.28 contains the faintest streak (streak no. 13 in Figure 2.13) and this offered a good opportunity to test our automatic detection algorithm using the matched-filter technique (refer to Section 3.1.1) on this image. So ultimately, the kernel solution shown in Figure 3.30 (f) was convolved with the reference image shown in Fig. 3.30 (b) and a constant background value estimated from the DanDia algorithm was added to form the model image (see Equation 3.37). The difference image was obtained by subtracting the model image from the target image (see Figure 3.32) and finally the automatic detection technique was applied to it. For a comparison, the parameters obtained with the visual detection (explained in Section 2.3.1) and the automatic detection are presented in Table 3.1.

For a 2K×2K raw TDI frame, if the CCD dark frames and the corresponding high signal-to-noise ratio reference frame are available, the image

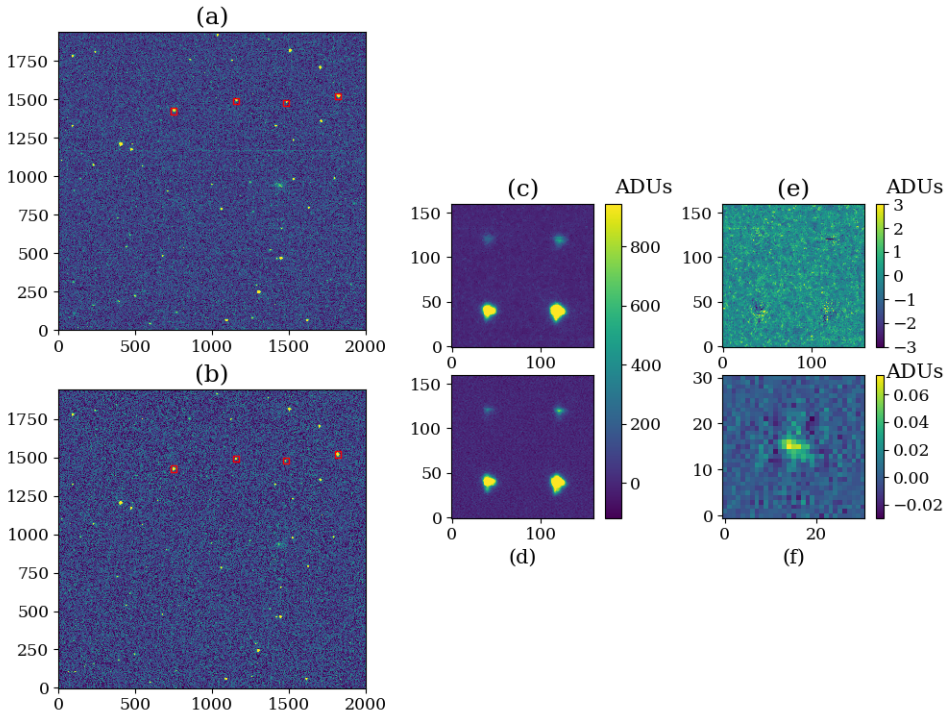

Figure 3.31: Construction of a dense stellar image out of a sparse field image in order to apply the difference image analysis. Images (a) and (b) are the target and reference image, respectively. The small red squares on these images are highlighting the sources selected for constructing the dense stellar field images (c) and (d) from (a) and (b), respectively. Image (e) shows the normalized residuals and Image (f) shows the kernel solution.

processing time for a complete streak detection analysis in the Fourier space on a computer with 64 Gb memory at 2.3 GHz clock-speed is ∼140 seconds. In the context of the 4-m ILMT, a computer with same configuration would take ∼290 seconds to process a 4K×4K raw image. We have planned to use the high performance computer clusters maintained by Consortium des Equipements de Calcul Intensif (CECI, http://www.ceci-hpc.be) for parallel processing of multiple raw CCD frames each night obtained with the 4-m ILMT survey. This will facilitate a real time streak detection or even transient detection in general.

A flowchart highlighting the post processing steps for a raw CCD image leading to the detection of a debris streak is shown in Figure 3.33. All the steps surrounded by the dashed blue square have been discussed in Chapter 2. The components of the flowchart surrounded by the red dashed square are elaborated in the current chapter (Ch. 3). In Section 3.1, we understood

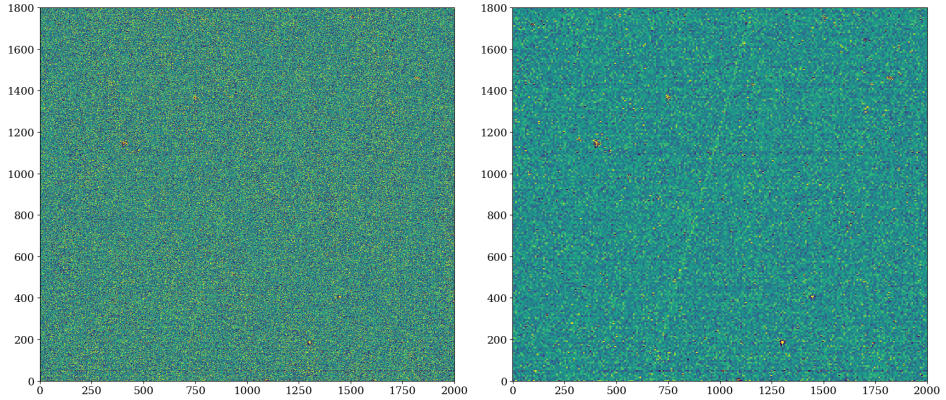

Figure 3.32: The image on the left is the residual image obtained after applying the DanDia algorithm on the target image shown in Figure 3.28. The image on the right is the wavelet based denoising (discussed in Section 3.3) applied to the residual image, hence showing the contrast enhanced faint streak.

Table 3.1: Comparison of the characteristics of the streak no. 13 from the visual detection and the automatic detection.

	t_{bottom} (UT)	ϕ (°)	m_G
visual detection	20:30:38	164.8	8.8 ± 0.1
matched filter detection	20:30:39	164.7	8.8 ± 0.1

† t_{bottom} is the UT corresponding to the bottom location of the streak.

the process of the formation of a debris streak on a CCD image and theoretically modelled the streak. In the same section, we demonstrated the usage of matched filtering to detect the debris streak and its effectiveness in detecting faint streaks invisible to human eyes was assessed with the help of Monte Carlo simulations. The processing time of executing the automatic streak detection can be dramatically improved without compromising the sensitivity of the detection, thanks to the discrete Fourier transformation. This has been discussed and illustrated in Section 3.2. In the subsequent section (Sec. 3.3), we have implemented image contrast enhancement techniques to confirm the debris detection visually using the Wavelet transformation. However, we could not succeed in making the debris streak typically having $SNR_{max} \leq 10$, visible to the naked eyes. We have also used well known techniques such as the Hough transformation and the Radon transformation

for streak detection in Section 3.4. The Hough transformation was found not only less efficient in detecting faint streaks, but also computationally expensive. On the other hand, the Radon transformation in the Fourier space was found to be better than the Hough transformation, but its sensitivity for faint streak detection was not as good as our proposed matched filtering technique. All the demonstrations in this thesis have been carried out straight away by using Python 2.7 and its associated Numpy and Scipy libraries. From Section 3.5, we understood that, for the matched filtering to be effective, one needs to perform difference image analysis to remove any sort of light sources other than space debris. We took inspiration from ROBONET, 2019 to code DANDIA algorithm in Python language. To make the algorithm computationally efficient, we introduced a new approach where instead of choosing all sources in the image, only a few bright sources are selected to construct the kernel solution. In the process of making DIA, several issues related to the alignment of the TDI images and their potential solutions were also discussed in that section.

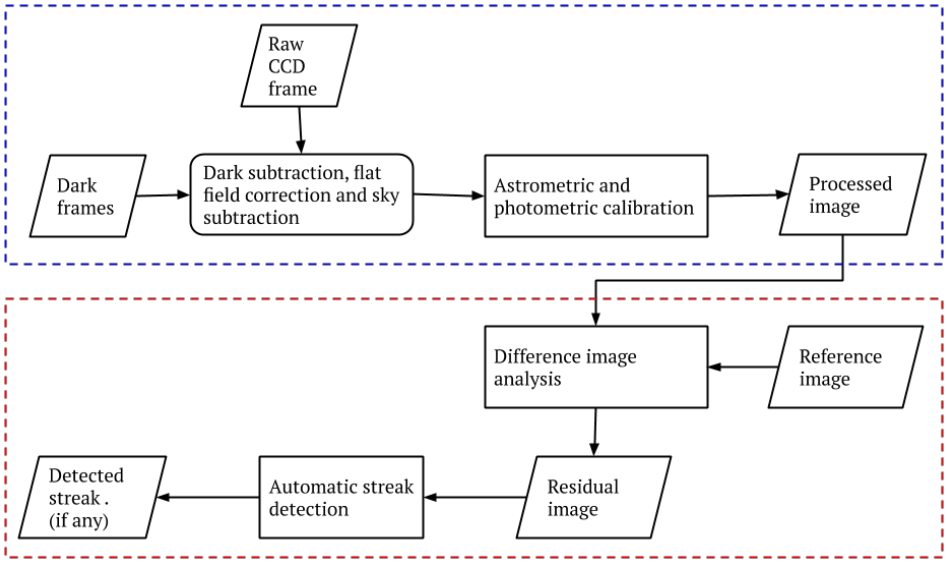

Figure 3.33: Flowchart of a raw image processing leading to a streak detection.

4

Prospects of space debris detection and characterization with the ILMT

The size determination of space debris depends on their apparent magnitude (Eq. 1.12), which in turn depends on their angular velocity (Eq. 1.13). Till now, we have been completely dependent on the TLE catalogue to obtain the angular velocity of every detected object. There has been a substantial amount of studies on the limitations of the SGP4/SDP4 algorithm for TLE orbit determination limited by the accuracy of the mathematical model put in practice (Hartman, 1993; Boyce, 2004; Kelso, 2007; Vallado and Cefola, 2012). So the orbit determination from real-time observations, independent of or in coordination with the TLE catalogue, could produce more accurate object size estimations. Moreover, a real-time orbital parameter estimation can also be used to refine and update the TLEs (Vallado and Agapov, 2010; Thomas et al., 2019).

4.1 Strategy and theoretical developments

In the classical mode of optical observations (i.e. without TDI mode), several methods have been adopted to measure the angular velocity of a passing object over the field of view of the camera. Africano et al., 1999 have used sequences of CCD images with the 3-m NASA LMT, captured at a short time interval to derive the speed of the passing debris in LEO. Choi et al., 2018 have used a chopper system to measure the angular velocities of the satellites in LEO from a single CCD frame. We propose an observation strategy that can be applicable to the TDI mode observation with a CCD

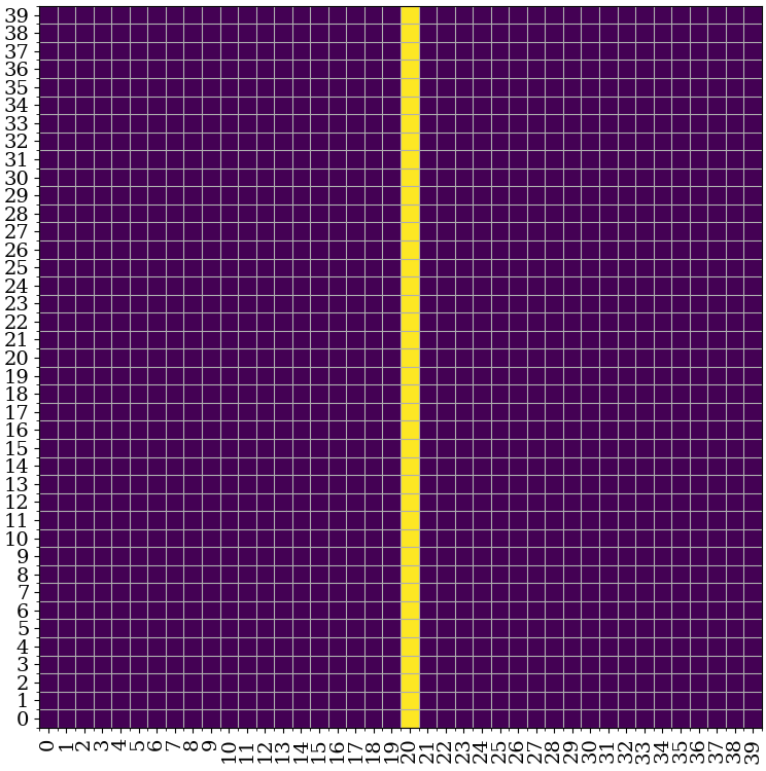

Figure 4.1: Schematic of a 40×40 pixels CCD image. The yellow squares show the trajectory of a passing object over the CCD in a conventional TDI mode at sidereal rate.

to determine the angular velocity of an object passing overhead. The basic principle here is to make the charge transfer between the CCD rows in such a way that a streak will be segregated into two separate dashed ones. Then by establishing a linear relationship between the length of each dash and the charge transfer time, one can determine the angular velocity of the passing objects.

Indeed, let us assume that the debris moves N pixels per second along the vertical direction from bottom to top and the rows of electronic charges are transferred from left to right by one pixel every P sec., corresponding to the integration time between two charge transfers. A schematic is shown in Figure 4.1 illustrating a streak that would be imprinted on a CCD operated in TDI mode, from the passing debris. If the object entering the CCD field of view is moving by N = 4 pixels per second oriented at 90° with respect to the CCD columns, then it will take 10 seconds to cross the 40×40 pixels CCD.

If we transfer all the rows of electronic charges by M+1 pixels to the right at time t = 0 sec., then integrate during P seconds, then move the

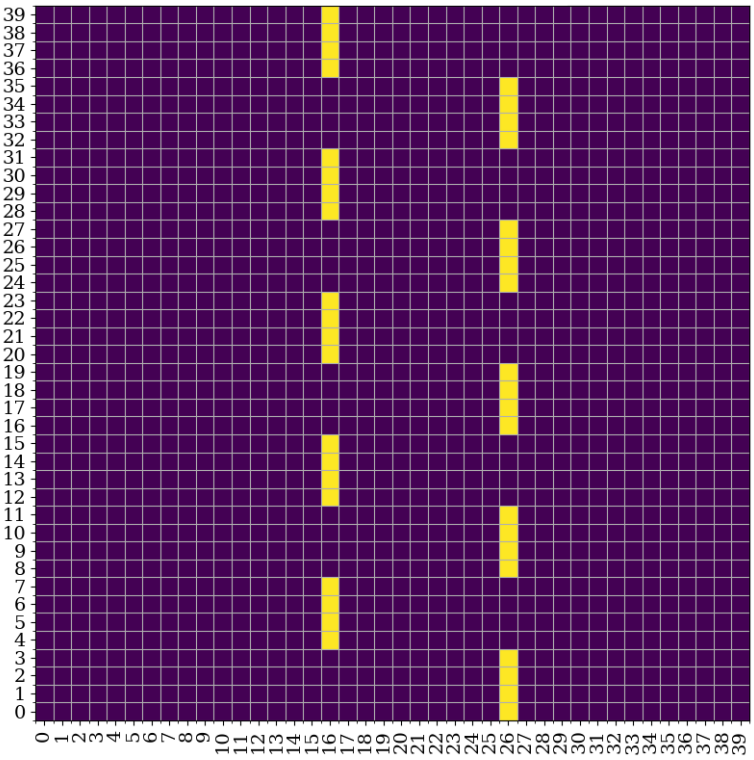

Figure 4.2: Schematic of the trajectory of a space debris on a 40×40 pixels CCD image after the angular velocity determination strategy is implemented. The debris is assumed to have a linear velocity of 4 pixels per second. The values of M and P adopted here are 10 pixels and 1 second, respectively.

charges to the left by M-1 pixels, then integrate P seconds, and repeat this process indefinitely, the debris streak will appear as shown in Figure 4.2, composed of two parallel and vertical streak trajectories, separated by M pixels. We could then measure the length of the dashes and dividing it by the integration time (P) will determine the angular velocity of the moving debris.

4.1.1 Analytical modeling of a double dashed streak

Assuming an infinitely thin vertical dashed streak along the vertical (y) direction (cf. Figure 4.3), the equation representing it is merely given by

$$P_1(y) = \frac{\alpha}{2}\frac{1}{(2N+1)\Lambda}\sum_{n=0}^{2N}\Pi\left(\frac{y-(n-N)2\Lambda}{\Lambda}\right), \tag{4.1}$$

where the number of dashes is being supposed to be equal to 2N + 1. As usual Π represents the top-hat or door function (described in Section 3.2)

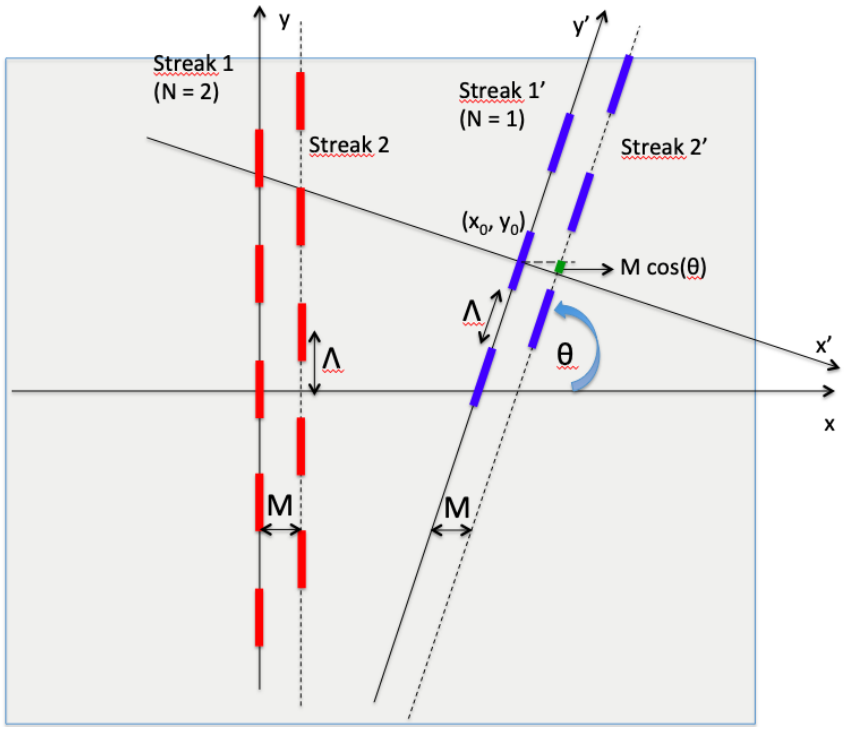

Figure 4.3: Illustration of a double vertical dashed streak (in red) due to a passing space debris for the case $N = 2$ (at left) and a double dashed streak with an inclination angle θ (in blue) centered at (x_0, y_0) for the case $N = 1$.

and $\alpha/2$ is half of the total flux of the space debris integrated along one of the dashed streaks. Integration of $P_1(y)$ along the y axis leads of course to $\alpha/2$.

If we take the Fourier transform of $P_1(y)$, we find

$$FT[P_1(y)](q) = \frac{\alpha}{2}\frac{1}{(2N+1)\Lambda}\sum_{n=0}^{2N}\int_{-\infty}^{\infty}\Pi(\frac{y-(n-N)2\Lambda}{\Lambda})\exp^{-2i\pi qy}\,dy, \tag{4.2}$$

and after making use of the change of variables $z = \frac{y-(n-N)2\Lambda}{\Lambda}$

$$\begin{aligned} FT[P_1(y)](q) &= \sum_{n=0}^{2N}\int_{-\infty}^{\infty}\Pi(z)\exp^{-2i\pi q\Lambda z}\,dz\,\Lambda\exp^{-2i\pi q(n-N)2\Lambda}, \\ &= \frac{\alpha}{2}\frac{\sin(\pi q\Lambda)}{\pi q\Lambda}\frac{2\pi q\Lambda}{\sin(2\pi q\Lambda)}\frac{\sin((2N+1)2\pi q\Lambda)}{(2N+1)2\pi q\Lambda}. \end{aligned} \tag{4.3}$$

A discrete Fourier transform of the 'Streak 1' in Fig. 4.3 is shown in Figure 4.4 which resembles the analytical expression derived above. We can

also see that two secondary peaks appear on both sides of the main central peak. Theoretically the positions of these peaks are at $\pm\frac{1}{2\Lambda}$. We may utilized this property to derive the angular velocity of the space debris.

If the expression in Eq. 4.3 characterizes the first dashed streak, we would similarly find from the function $P_2(y) = P_1(y - \Lambda)$ characterizing the second dashed streak, that its Fourier transform is merely given by

$$FT[P_2(y)](q) = FT[P_1(y - \Lambda)](q) = FT[P_1(y](q) \exp^{-2i\pi q\Lambda} . \tag{4.4}$$

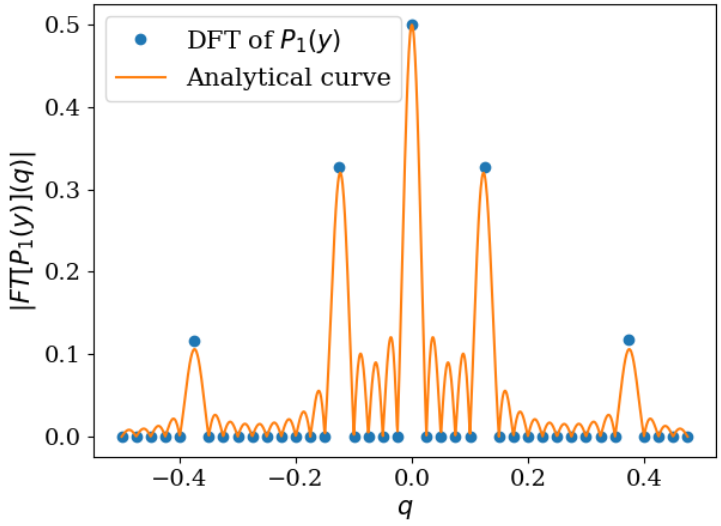

Figure 4.4: Discrete Fourier transform of the streak 1 characterized by $\alpha = 1$, $N = 2$ and $\Lambda = 4$ pixels. The analytical curve generated using Eq. 4.3 perfectly passes through each DFT values.

Of course, we should now take into account the width of the streak along the x axis. Assuming that its profile $Q_1(x)$ is characterized by a $1-D$ Gaussian function with $FWHM$ representing its full width at half maximum, we have

$$Q_1(x) = \frac{2\sqrt{\ln(2)}}{FWHM\sqrt{\pi}} \exp(\frac{-4\ln(2)x^2}{\text{FWHM}^2}), \tag{4.5}$$

while its Fourier transform is easily found to be

$$FT[Q_1(x)](p) = \exp\left(\frac{-\pi^2 p^2 \text{ FWHM}^2}{4\ln(2)}\right), \tag{4.6}$$

and we notice again that narrower is the dashed streak, broader is its width in the Fourier space.

Assuming that the second dashed streak is offset along the x direction by M pixels with respect to the first one, we would similarly find that

$$FT[Q_2(x)](p) = FT[Q_1(x-M)](p) = FT[Q_1(x)](p)\exp^{-2i\pi pM}\,. \tag{4.7}$$

What we directly obtain after the Fourier transformation of the observed CCD frame is of course

$$\begin{aligned}
&FT[Q_1(x)P_1(y)+Q_2(x)P_2(y)](p,q)\\
&\quad= FT[Q_1(x](p)FT[P_1(y](q) + FT[Q_2(x](p)FT[P_2(y](q),\\
&\quad= FT[Q_1(x](p)FT[P_1(y](q) + FT[Q_1(x](p)FT[P_1(y](q)\\
&\qquad\exp^{-2i\pi pM}\exp^{-2i\pi q\Lambda},\\
&\quad= FT[Q_1(x](p)FT[P_1(y](q)[1+\exp^{-2i\pi pM}\exp^{-2i\pi q\Lambda}],\\
&\quad= FT[Q_1(x](p)FT[P_1(y](q)[\exp^{i\pi(pM+q\Lambda)}+\exp^{-i\pi(pM+q\Lambda)}]\\
&\qquad\exp^{-i\pi(pM+q\Lambda)},\\
&\quad= FT[Q_1(x](p)FT[P_1(y](q)\,2\cos\pi(pM+q\Lambda)\exp^{-i\pi(pM+q\Lambda)},\\
&\quad= \alpha\exp\left(\frac{-\pi^2p^2\ \mathrm{FWHM}^2}{4\ln(2)}\right)\frac{\sin(\pi q\Lambda)}{\pi q\Lambda}\frac{2\pi q\Lambda}{\sin(2\pi q\Lambda)}\frac{\sin((2N+1)2\pi q\Lambda)}{(2N+1)2\pi q\Lambda}\\
&\qquad\cos\pi(pM+q\Lambda)\exp^{-i\pi(pM+q\Lambda)}\,.
\end{aligned} \tag{4.8}$$

We see here some nice modulation of the signal. In principle, we could fit the observed signal with the above function while determining the parameters N and Λ and subsequently derive the corresponding angular velocity of the space debris. Such a synthetic streak generated according to the expressions in Equations 4.1 and 4.5 is shown in Figure 4.5. The 2-D discrete Fourier transformation of this image and its corresponding theoretical chi-square fit according to Eq. 4.8 is shown in Figure 4.6.

However, in practical scenario, the probability of observing a space debris with a vertical trajectory and passing through $x = 0$ is very unlikely. Therefore, let us generalize this approach to the case of a double dashed streak inclined by an angle θ with respect to the x direction and centered at x_0, y_0 (see Figure 4.3, right). We may write for the expression of the first dashed streak $(1')$ centered at $(x' = 0, y' = 0)$ that its flux distribution on the CCD is merely given by the expression $Q_1(x')P_1(y')$ (see Eqs. 4.1 & 4.5). Considering the second dashed streak $(2')$, because of the inclination angle θ, its center position is offset along the x' direction by $M\sin(\theta)$ pixels and along the y' direction by $M\cos(\theta)$ pixels. Consequently, the expression of its flux distribution is easily found to be $Q_1(x' - M\sin(\theta))P_1(y' - M\cos(\theta) - \Lambda)$ (see Figure 4.3, right). Finally, in accordance with Eq. 3.23, the Fourier

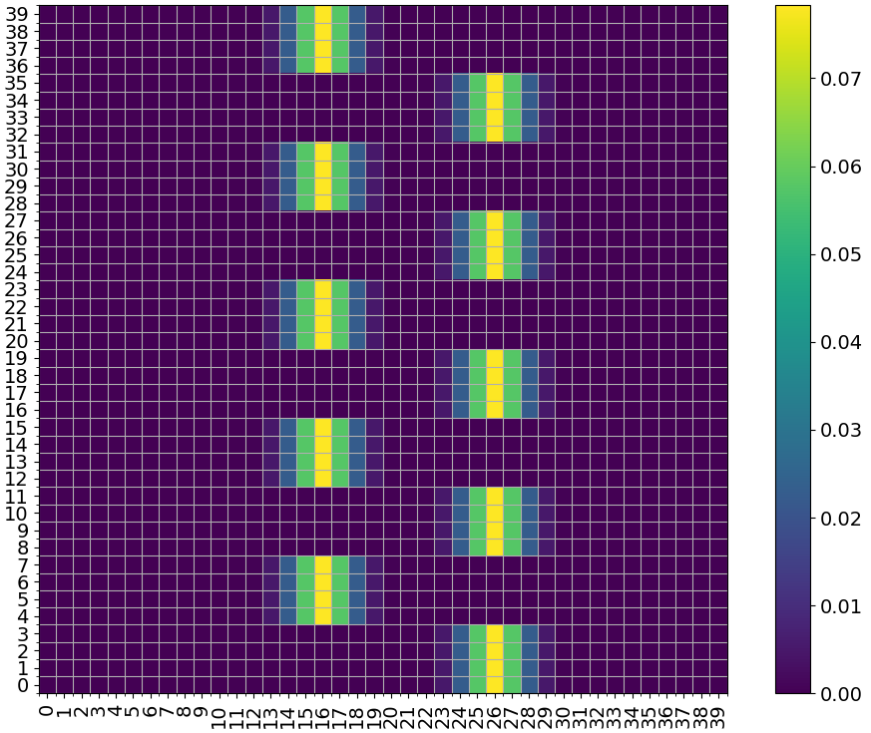

Figure 4.5: A synthetic 40×40 pixels CCD image showing a double dashed streak oriented vertically due to a passing point source. The velocity of the source is 4 pixels/second. The values of α, $FWHM$, M and P are equal to 10 ADUs, 3 pixels, 10 pixels and 1 second, respectively.

transform of this inclined double dashed streak light distribution $I(x', y')$ may be derived as follows

$$
\begin{aligned}
&FT[I(x', y')](p, q) \\
&= FT[Q_1(x')P_1(y') + Q_1(x' - M\sin\theta)P_1(y' - M\cos\theta - \Lambda))](p, q) \\
&= FT[Q_1(x')P_1(y') + Q_1(x' - M\sin\theta)P_1(y' - M\cos\theta - \Lambda))](p', q') \\
&\quad \exp^{-2i\pi(px_0+qy_0)} \\
&= 2\,FT[Q_1(x')P_1(y')](p', q')\cos\pi[M\sin\theta\ p' + (M\cos\theta + \Lambda)q'] \\
&\quad \exp^{-i\pi[M\sin\theta\ p'+(M\cos\theta+\Lambda)q']}\exp^{-2i\pi(px_0+qy_0)}.
\end{aligned}
\tag{4.9}
$$

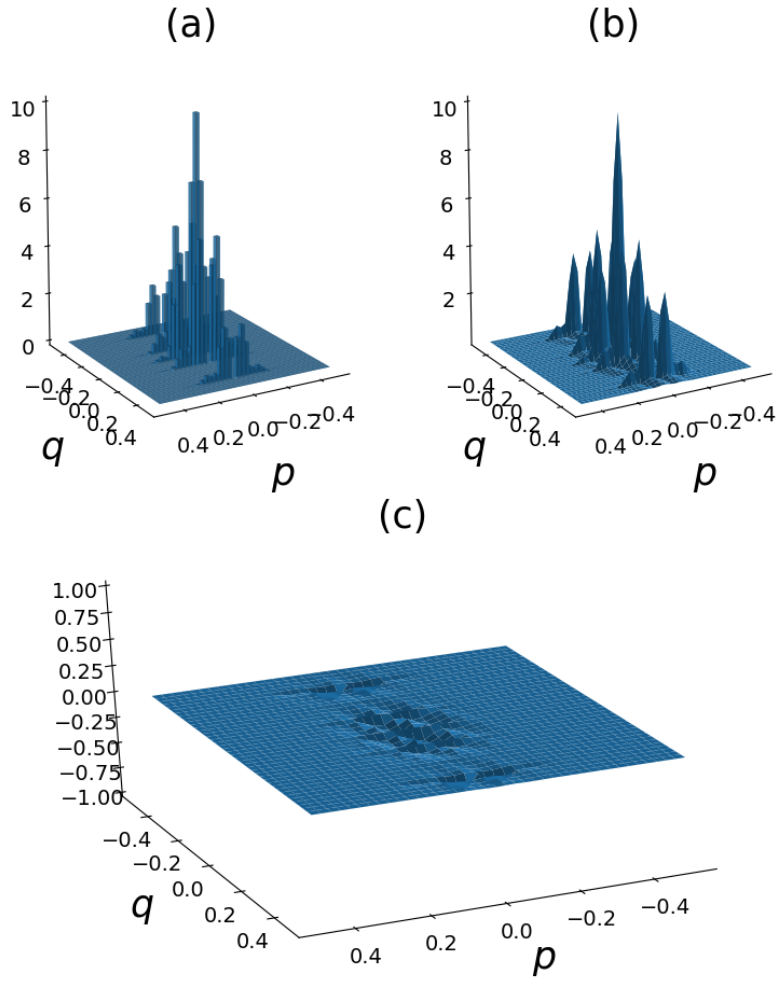

Figure 4.6: 3D representations of (a) the absolute values obtained from the discrete Fourier transform of the CCD image shown in Fig. 4.5, (b) the best fit theoretical curve according to Eq. 4.8 and (c) the residuals obtained after subtracting the pixel values shown in plot (a) from their respective pixel values in plot (b).

Replacing in the latter equation, the expression of $FT[Q_1(x')P_1(y')](p',q') = FT[Q_1(x')](p')FT[P_1(y')](q')$ by those given in Eqs. 4.3, 4.6 & 3.24

$$
\begin{aligned}
&FT[I(x,y)](p,q) \\
&= \alpha \exp\left(\frac{-\pi^2(p\sin\theta - q\cos\theta)^2 \mathrm{FWHM}^2}{4\ln(2)}\right) \\
&\frac{\sin(\pi(p\cos\theta + q\sin\theta)\Lambda)}{\pi(p\cos\theta + q\sin\theta)\Lambda} \frac{2\pi(p\cos\theta + q\sin\theta)\Lambda}{\sin(2\pi(p\cos\theta + q\sin\theta)\Lambda)} \\
&\frac{\sin((2N+1)2\pi(p\cos\theta + q\sin\theta)\Lambda)}{(2N+1)2\pi(p\cos\theta + q\sin\theta)\Lambda} \\
&\cos\pi[M\sin\theta(p\sin\theta - q\cos\theta) + (M\cos\theta + \Lambda)(p\cos\theta + q\sin\theta)] \\
&\exp^{-i\pi[M\sin\theta(p\sin\theta - q\cos\theta) + (M\cos\theta+\Lambda)(p\cos\theta+q\sin\theta) + 2(px_0+qy_0)]}.
\end{aligned}
\tag{4.10}
$$

4.1.2 Streak detection using the matched filter

As per our previous discussions in Chapters 3.1 & 3.2, the best matched filter is the intensity normalized version of $I(x, y)$, i.e. the PSF. So the expression of the Fourier transform of the corresponding PSF for an inclination angle ϕ is directly obtained by setting $\alpha = 1$, $x_0 = 0, y_0 = 0$ and $\theta = \phi$ in Eq. 4.10. We thus find

$$
\begin{aligned}
&FT[PSF(x,y)](p,q) = \\
&\exp\left(\frac{-\pi^2(p\sin\phi - q\cos\phi)^2 \mathrm{FWHM}^2}{4\ln(2)}\right) \\
&\frac{\sin(\pi(p\cos\phi + q\sin\phi)\Lambda)}{\pi(p\cos\phi + q\sin\phi)\Lambda} \frac{2\pi(p\cos\phi + q\sin\phi)\Lambda}{\sin(2\pi(p\cos\phi + q\sin\phi)\Lambda)} \\
&\frac{\sin((2N+1)2\pi(p\cos\phi + q\sin\phi)\Lambda)}{(2N+1)2\pi(p\cos\phi + q\sin\phi)\Lambda} \\
&\cos\pi[M\sin\phi(p\sin\phi - q\cos\phi) + (M\cos\phi + \Lambda)(p\cos\phi + q\sin\phi)] \\
&\exp^{-i\pi[M\sin\phi(p\sin\phi - q\cos\phi) + (M\cos\phi + \Lambda)(p\cos\phi + q\sin\phi)}.
\end{aligned}
\tag{4.11}
$$

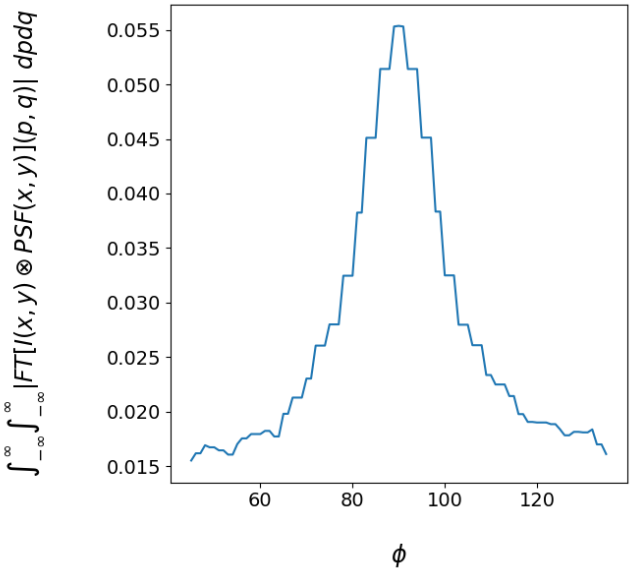

Figure 4.7: Plot of the integrated value of the Fourier transform of the modulus of the convolution product $I(x, y) \otimes PSF(x, y)$ in the Fourier space versus the PSF inclination angle ϕ. $I(x, y)$ corresponds to the debris streak shown in Fig 4.5. As expected, we see that the maximum is reached for $\phi = \theta = 90°$

Following the case of a single debris streak, we are now ready to make use of Eq. 3.29 to derive the parameters of a double streak. In Chapter 3.2, we have been using the matched-filtered technique in the Fourier space to detect at best the presence of space debris streaks. Here also, we should take the Fourier transform of the convolution product ($\otimes$) of the streak signal $I(x, y)$ and the normalized point spread function $PSF(x, y)$ (cf. Eq. 3.29). We find

$$
\begin{aligned}
&FT[I(x,y) \otimes PSF(x,y)](p,q) \\
&= \alpha \, \exp\left(\frac{-\pi^2 (p\sin\theta - q\cos\theta)^2 \; FWHM^2}{4\ln(2)}\right) \\
&\exp\left(\frac{-\pi^2 (p\sin\phi - q\cos\phi)^2 \; FWHM^2}{4\ln(2)}\right) \\
&\frac{\sin(\pi(p\cos\theta + q\sin\theta)\Lambda)}{\pi(p\cos\theta + q\sin\theta)\Lambda} \frac{\sin(\pi(p\cos\phi + q\sin\phi)\Lambda)}{\pi(p\cos\phi + q\sin\phi)\Lambda} \\
&\frac{2\pi(p\cos\theta + q\sin\theta)\Lambda}{\sin(2\pi(p\cos\theta + q\sin\theta)\Lambda)} \frac{2\pi(p\cos\phi + q\sin\phi)\Lambda}{\sin(2\pi(p\cos\phi + q\sin\phi)\Lambda)} \\
&\frac{\sin((2N+1)2\pi(p\cos\theta + q\sin\theta)\Lambda)}{(2N+1)2\pi(p\cos\theta + q\sin\theta)\Lambda} \\
&\frac{\sin((2N+1)2\pi(p\cos\phi + q\sin\phi)\Lambda)}{(2N+1)2\pi(p\cos\phi + q\sin\phi)\Lambda} \\
&\cos\pi[M\sin\theta(p\sin\theta - q\cos\theta) + (M\cos\theta + \Lambda)(p\cos\theta + q\sin\theta)] \\
&\cos\pi[M\sin\phi(p\sin\phi - q\cos\phi) + (M\cos\phi + \Lambda)(p\cos\phi + q\sin\phi)] \\
&\exp^{-i\pi[M\sin\theta(p\sin\theta - q\cos\theta) + (M\cos\theta+\Lambda)(p\cos\theta+q\sin\theta) + 2(px_0+qy_0)]} \\
&\exp^{-i\pi[M\sin\phi(p\sin\phi - q\cos\phi) + (M\cos\phi+\Lambda)(p\cos\phi+q\sin\phi)]} .
\end{aligned}
\tag{4.12}
$$

It should then be easy to find out the orientation θ of the streak by integrating the absolute value of $FT[I(x, y) \otimes PSF(x, y)](p, q)$ over the coordinates (p, q) for typically 180 different values of the angle ϕ. The proper orientation of the double dashed streak corresponds to the value of ϕ for which that quantity shows a real maximum. As expected, the maximum value must be reached for $\phi = \theta$ (cf. Fig. 4.7). The integrated value of the Fourier transform of the modulus of the convolution product $I(x, y) \otimes PSF(x, y)$ in

the Fourier space for $\theta = \phi$ is then found to be

$$\begin{aligned}
&\int_{-\infty}^{\infty}\int_{-\infty}^{\infty} |FT[I(x,y) \otimes PSF(x,y)]|(p,q)dpdp \\
&= \int_{-\infty}^{\infty}\int_{-\infty}^{\infty} |FT[I(x,y)](p,q)\, FT[PSF(x,y)](p,q)|dpdp \\
&= \alpha \int_{-\infty}^{\infty}\int_{-\infty}^{\infty} |FT[PSF(x,y)](p,q)\, FT[PSF(x,y)](p,q)|dpdp \\
&= \alpha \int_{-\infty}^{\infty}\int_{-\infty}^{\infty} |FT[PSF(x,y)](p,q)|^2 dpdp.
\end{aligned} \tag{4.13}$$

Making use of the Parseval theorem, we may write

$$\begin{aligned}
&\int_{-\infty}^{\infty}\int_{-\infty}^{\infty} |FT[I(x,y) \otimes PSF(x,y)]|(p,q)dpdp \\
&= \alpha \int_{-\infty}^{\infty}\int_{-\infty}^{\infty} |FT[PSF(x,y)](p,q)|^2 dpdp \\
&= \alpha \int_{-\infty}^{\infty}\int_{-\infty}^{\infty} PSF^2(x,y)dxdy.
\end{aligned} \tag{4.14}$$

For the case of a double dashed streak, the corresponding expression of the $PSF(x,y)$ may be written as follows

$$\begin{aligned}
&PSF(x,y) \\
&\qquad = PSF_1(x,y) + PSF_2(x,y) \\
&\qquad = PSF_1(x,y) + PSF_1(x-M, y-\Lambda\sin(\theta)),
\end{aligned} \tag{4.15}$$

Equation 4.14 may then be transformed as

$$\begin{aligned}
&\int_{-\infty}^{\infty}\int_{-\infty}^{\infty} |FT[I(x,y) \otimes PSF(x,y)]|(p,q)dpdp \\
&= \alpha \int_{-\infty}^{\infty}\int_{-\infty}^{\infty} PSF^2(x,y)dxdy \\
&= \alpha \int_{-\infty}^{\infty}\int_{-\infty}^{\infty} \{PSF_1^2(x,y) + PSF_1^2(x-M, y-\Lambda\sin\theta) \\
&\quad + 2PSF_1(x,y)PSF_1(x-M, y-\Lambda\sin\theta)\}dxdy \\
&= \alpha \int_{-\infty}^{\infty}\int_{-\infty}^{\infty} \{PSF_1^2(x,y) + PSF_1^2(x-M, y-\Lambda\sin\theta)\}dxdy \\
&= 2\alpha \int_{-\infty}^{\infty}\int_{-\infty}^{\infty} PSF_1^2(x,y)dxdy = 2\alpha \int_{-\infty}^{\infty}\int_{-\infty}^{\infty} PSF_1^2(x',y')dx'dy'.
\end{aligned} \tag{4.16}$$

Indeed, a look at Fig. 4.3 clearly shows that because of the shifting of the electronic charges by $\pm M$ pixels along the x direction, the product $PSF_1(x,y)\,PSF_1(x-M, y-\Lambda\sin\theta) = 0$.

The expression of $PSF_1(x',y')$ is simply given by

$$PSF_1(x',y') = Q_1(x')P_1(y'), \tag{4.17}$$

with $Q_1(x')$ and $P_1(y')$ given by Eqs. 4.5 and 4.1, respectively, for the value $\alpha = 1$. Equation 4.16 may thus be re-written as

$$\begin{aligned}
&\int_{-\infty}^{\infty}\int_{-\infty}^{\infty} |FT[I(x,y)\otimes PSF(x,y)]|(p,q)dpdp \\
&= 2\alpha\int_{-\infty}^{\infty}\int_{-\infty}^{\infty} PSF_1^2(x',y')dx'dy' = 2\alpha\int_{-\infty}^{\infty} Q_1^2(x')dx'\int_{-\infty}^{\infty} P_1^2(y')dy' \\
&= 2\alpha\int_{-\infty}^{\infty}\{\frac{2\sqrt{\ln(2)}}{FWHM\sqrt{\pi}}\}^2\exp(\frac{-8\ln(2)x^2}{\mathrm{FWHM}^2})dx' \\
&\quad\int_{-\infty}^{\infty}\{\frac{1}{2}\frac{1}{(2N+1)\Lambda}\}^2\sum_{n=0}^{2N}\Pi^2(\frac{y-(n-N)2\Lambda}{\Lambda})dy' \\
&= \alpha\frac{\sqrt{2\ln(2)}}{\sqrt{\pi}FWHM}\frac{1}{2(2N+1)\Lambda}.
\end{aligned} \tag{4.18}$$

Since we have $\lambda = 2(2N+1)\Lambda$ (see Eq. 3.16) and given the expression of Q (see Eq. 3.7), the final result established in Eq. 4.18 is quite analogous to the result previously derived for the case of a single continuous streak (see Eq. 3.32). Hence we also namely find here that

$$\int_{-\infty}^{\infty}\int_{-\infty}^{\infty} |FT[I(x,y)\otimes PSF(x,y)]|(p,q)dpdp = \frac{\alpha Q}{\lambda}$$

In the current PSF, Λ and N are unknown parameters which means that we do not know a priori the length of each dash and their numbers. So we propose to use a double continuous streak as the convolution PSF and remain independent of Λ or N while detecting a debris streak.

Adopting for the light distribution of the double streak of the space debris, the expression $\alpha PSF(x,y)$ with $PSF(x,y)$ given by Eq. 4.15 but for the point spread function the expression $\frac{1}{2}[Q_1(x') + Q_1(x' - M\sin(\theta))]\Pi(y'/\lambda)/\lambda$ which corresponds to a double continuous streak. Let us first consider the case of a double continuous streak at $\theta = 90°$. It is then easy to show that

the double continuous streak can be generated using four dashed streaks as follows:

$$\begin{aligned}&\frac{1}{2\lambda}[Q_1(x)+Q_1(x-M)]\Pi(y/\lambda)\\&=\frac{1}{2}[PSF_1(x,y)+PSF_1(x,y-\Lambda)+\\&PSF_1(x-M,y-\Lambda)+PSF_1(x-M,y)].\end{aligned}\tag{4.19}$$

Convolving $\alpha PSF(x,y)$, which represents the debris streak (see Eq. 4.15) with the above expression, we obtain

$$\begin{aligned}&\alpha PSF(x,y)\otimes\\&\frac{1}{2}[PSF_1(x,y)+PSF_1(x,y-\Lambda)+PSF_1(x-M,y-\Lambda)+PSF_1(x-M,y)]\\&=\frac{\alpha}{2}[PFS_1(x,y)\otimes PFS_1(x,y)+\\&PFS_1(x-M,y-\Lambda)\otimes PFS_1(x-M,y-\Lambda)],\end{aligned}\tag{4.20}$$

If we use the dashed double streak as the PSF, we would obtain,

$$\begin{aligned}&\alpha PSF(x,y)\otimes[PSF_1(x,y)+PSF_1(x-M,y-\Lambda)]\\&=\alpha[PFS_1(x,y)\otimes PFS_1(x,y)+\\&PFS_1(x-M,y-\Lambda)\otimes PFS_1(x-M,y-\Lambda)].\end{aligned}\tag{4.21}$$

By comparing Equations 4.20 and 4.21, we observe that the convolution results will be halved for the case of the double continuous streak PSF. Hence the integration of the modulus of the Fourier transform of the convolution product of $I(x,y)$ and the double continuous PSF will be

$$\begin{aligned}&\int_{-\infty}^{\infty}\int_{-\infty}^{\infty}|FT[I(x,y)\otimes PSF(x,y)]|(p,q)dpdp\\&=\frac{\alpha}{2}\frac{\sqrt{2\ln(2)}}{\sqrt{\pi}FWHM}\frac{1}{2(2N+1)\Lambda}.\end{aligned}\tag{4.22}$$

This is numerically confirmed in Figure 4.8.

By iterating over different orientations of the continuous double streak PSF (typically ϕ ranging from 0° to 180°) and calculating the integration result of the modulus of the convolution product with the CCD image containing the double dashed debris streak in the Fourier space, the inclination of the debris streak will be easily determined from the maximum observed in the integration result. Once the orientation of the debris streak (ϕ) is determined, shearing the image by an amount of ϕ (cf. Figure 3.3) will situate the dashed double streaks perpendicular to the CCD columns. It is very

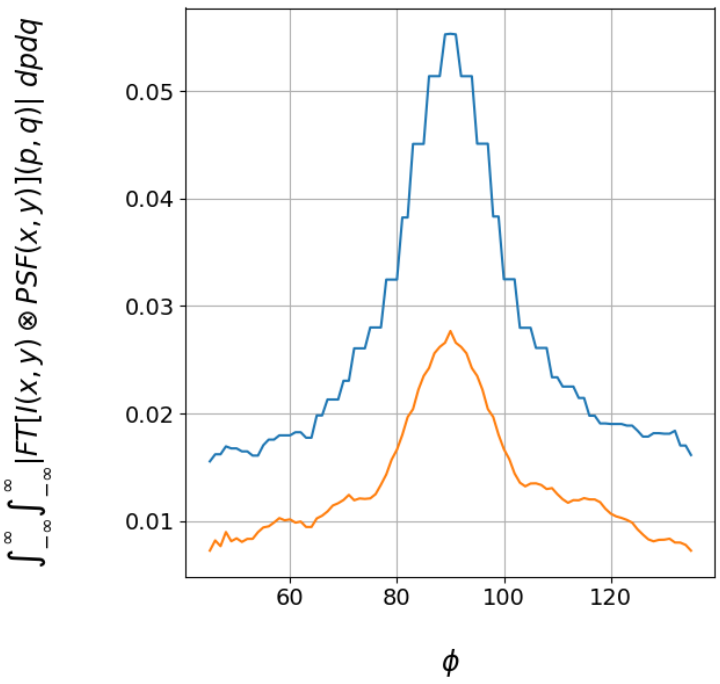

Figure 4.8: Plot of the integrated value of the Fourier transform of the modulus of the convolution product $I(x,y) \otimes PSF(x,y)$ in the Fourier space versus the PSF inclination angle ϕ. I(x,y) corresponds to the debris streak shown in Fig. 4.5. The blue plot is obtained by using the dashed double streak as $PSF(x,y)$. When a continuous double streak is used in place of the dashed one, we obtain the orange color plot. The ratio between the maximum value of the blue and that of the orange plot is 2.

convenient now to construct a 1-D profile of the streak by co-adding all the CCD columns. This 1-D profile can be written as,

$$I(x) = \frac{\alpha}{2}(PSF_1(x) + PSF_1(x - M)), \tag{4.23}$$

where $PSF_1(x)$ or $PSF_1(x - M)$ are the 1D representations of $PSF_1(x, y)$ and $PSF_1(x - M, y)$, respectively.

The bottom location of the debris streak can immediately after be found by convolving the 1D profile in Eq. 4.23 with a normalized double 1-D PSF separated by M pixels and finding out the location of the maximum of the convolution product. The maximum of the convolution product $I(x) \otimes PSF(x - x_0)$ will occur at $x = x_0$, where x_0 is the bottom location of the debris streak and its value for the case of a Gaussian intensity distribution (cf. Eq. 4.5) will be,

$$\int_{-\infty}^{\infty} \frac{\alpha}{4}(PSF_1(x) + PSF_1(x - M))^2 dx = \frac{\alpha}{2}\frac{\sqrt{2\ \ln(2)}}{\sqrt{\pi}FWHM} \tag{4.24}$$

This is numerically confirmed by the results shown in Figure 4.9.

In the presence of random noise in the CCD image characterized by σ^2 variance, the standard deviation of the 1D convolution product will be $\sigma^2 Q/2$ (as given in Eq. 3.4). Following the conventions in Eq. 3.5, the maximized signal-to-noise ratio of the double streak detection is expected to be,

$$SNR^d_{max} = \frac{\alpha}{\sigma}\sqrt{\frac{Q}{2}}. \tag{4.25}$$

4.1.3 Sensitivity of the streak detection

In this section we have tried to understand the effectiveness of the debris streak detection in the presence of random noise when considering a single streak as discussed in Chapt. 3 or a double dashed streak.

Equations 3.5 and 4.25 show the maximized signal-to-noise ratio of a debris streak after matched filtering is performed on a single continuous streak and a double dashed streak. We took several uniformly distributed random SNR_{max} values between 1 and 30. Given a fixed noise background of $\sigma = 100$ and $FWHM = 3$ pixels, the streak brightness α were calculated using Eqs. 3.5 and 3.7. For each α value, a single continuous debris streak and a double dashed debris streak was generated on a 1000 $\times$ 1000 pixels CCD grid oriented parallel to the CCD rows. Each dash was having a fixed Λ of 100 pixels and the separation between both streaks in a double dashed streak were kept at 10 pixels apart. Then a Gaussian noise having a standard deviation of 100 ADUs was added to each pixel which finally represents the case of very faint debris streaks.

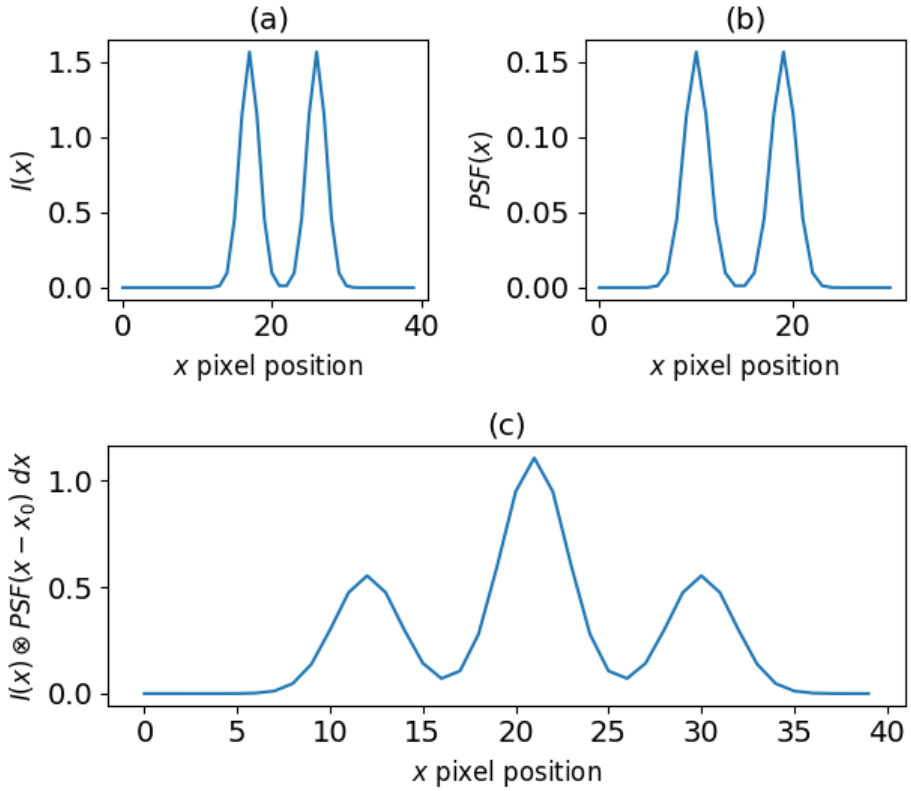

Figure 4.9: (a) The 1D double streak profile after co-adding all the CCD columns of the image shown in Fig. 4.5, (b) the 1D double filter profile or $PSF(x)$ to be convolved with $I(x)$, (c) the convolution product of $I(x)$ and $PSF(x - x_0)$ showing a peak at the central pixel position along x with respect to the double streak shown in Fig. 4.5.

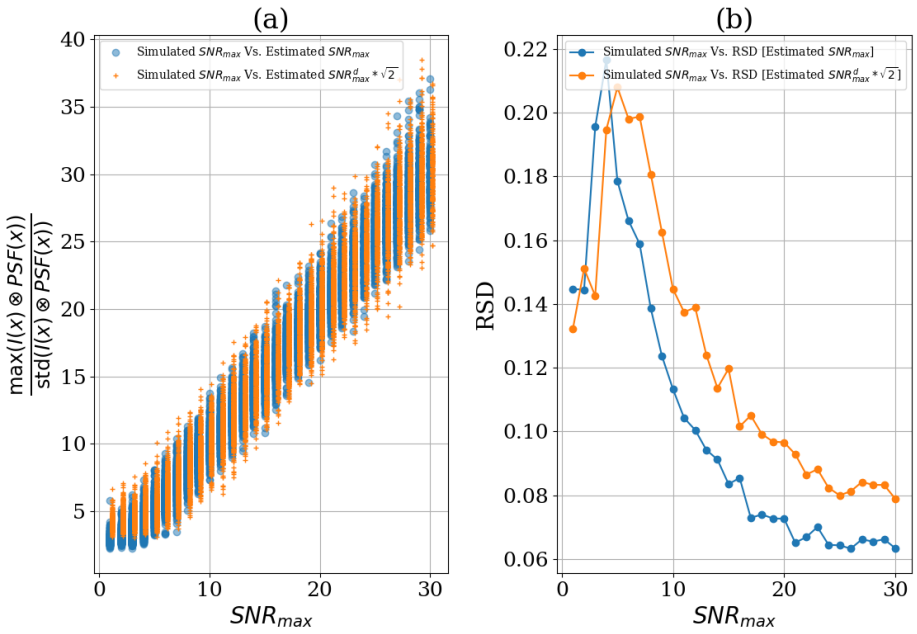

Figure 4.10: a) Comparison between theoretical maximized SNR (SNR_{max}) and numerically calculated maximized SNR. For a double dashed streak the numerical values are scaled up by a factor of $\sqrt{2}$, so as to make them comparable to the numerical values obtained from the single continuous streaks. b) Plot of the relative-standard deviation (RSD) versus SNR_{max}, i.e., for a simulated SNR_{max}, RSD is the standard deviation of the estimated SNR_{max}s divided by their mean value.

Each synthetic image was convolved with a normalized single continuous PSF or a double continuous PSF according to the simulated debris streak type. Subsequently the numerical maximum of each convolution product and associated standard deviation were determined. The ratio between these two represents the numerical maximized signal-to-noise ratio. A comparison between the numerical and the theoretical maximized SNRs is shown in Figure 4.10. It can be noticed that the numerical values obtained for the double dashed streaks are slightly more dispersed than those for the single continuous streaks as the simulated SNR_{max} value increases. This is expected because while constructing the 1-D profile of the streaks (cf. Equation 4.23) one encounters more noise for the case of a double dashed streak.

4.1.4 Estimating the angular velocity of the detected space debris

It has already been discussed that, the streak can be positioned perpendicularly to the CCD columns very easily after the orientation of the debris streak is determined. The idea now is to use several synthetic CCD frames each containing a vertically oriented normalized dashed double streak as PSFs to perform the convolution operation on the CCD image and calculate the integration of the modulus of their Fourier transform. If the length of Λ value is varied in each PSF, then a maximum will appear in the integration results when the length of each dash in the PSF matches the length of each dash in the debris streak (see Figure 4.11). Of course, the value of the maximum will be theoretically equal to the expression given in Equation 4.16. We can also take advantage of the information on the location of the debris streak and apply our proposed Fourier analysis on the specific region of the CCD image that only contains the streak. By doing so we minimize the effect of the high frequency noise and enhance the prediction of the Λ value. Subsequently, the estimated Λ value directly leads to the determination of the angular velocity (ω in arc-seconds per second) of the space debris , i.e.,

$$\omega = \frac{\Lambda}{P}\ sc, \tag{4.26}$$

where sc is the pixel scale (in arc-seconds per pixel).

Other methods to estimate the angular velocity

When the double dashed streak is oriented vertically and its location is determined, each single dashed streak from the double dashed debris streak can be extracted. Then by co-adding all the CCD rows, a one-dimensional streak profile can be generated which resembles the analytical expression given in Eq. 4.1. After taking the DFT of this profile we expect to produce a pattern that resembles Eq. 4.3 (also see Figure 4.4). By determining the locations of the secondary peaks in the DFT samples which are essentially separated by $1/\Lambda$, one can derive the angular velocity of the debris streak.

When the debris streak is oriented vertically, we also know that both single dashed streaks will be shifted from each other along the y-direction by an amount of Λ pixels. So, another approach to find the Λ value is to cross-correlate one of the 1D single dashed streak with respect to the other. By doing so, the maximum of the cross-correlation result will occur at Λ, corresponding to the complete overlapping between both 1D streaks.

Figure 4.12 shows the demonstration of these two techniques on a double dashed debris streak. We have found that both these approaches are much

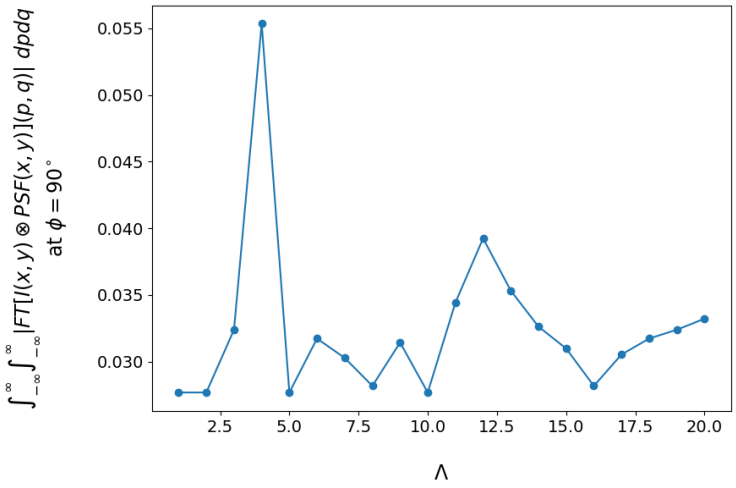

Figure 4.11: Integration of the absolute values of the Fourier transform of the convolution product of $I(x, y)$ and $PSF(x, y)$ oriented at $\phi = 90°$. The values of Λ have been varied from 1 pixel to half the size of the CCD image shown in Fig. 4.5. The maximum of the integration is achieved for $\Lambda = 4$ pixels which is the length of each dash seen in Fig. 4.5.

faster than the first one to determine the parameter Λ, but becomes ineffective for fainter streaks (streaks with $SNR_{max} \leq 20$). So we propose to adapt one of these techniques only if the estimated SNR_{max} is larger than 25.

4.2 Simulation results

A large fraction of the catalogued space debris population lies in LEO and their orbit inclination with respect to the Earth's equatorial plane is concentrated around 90° (Council, 1995; Liou et al., 2013; Johnson, 2011). So we have considered that the altitude of the debris population ranges from 400 km to 1000 km and their inclination (i.e., ϕ) to be between 45° and 135° in the following analysis. Here we also have assumed that the debris orbits are stable and circular.

Several debris altitudes and inclination angles were generated from uniform distributions of the aforementioned altitude and ϕ ranges, respectively. Applying simple Newtonian mechanics, the angular velocity of each debris was calculated from the respective altitude value. Then the value of Λ is estimated using Eq. 4.26. A pixel scale of ∼0.4 arc-second per pixel for the ILMT CCD camera and an integration time P of ∼0.027 second on each CCD pixel row in between two subsequent charge transfers were used to derive all Λ values.

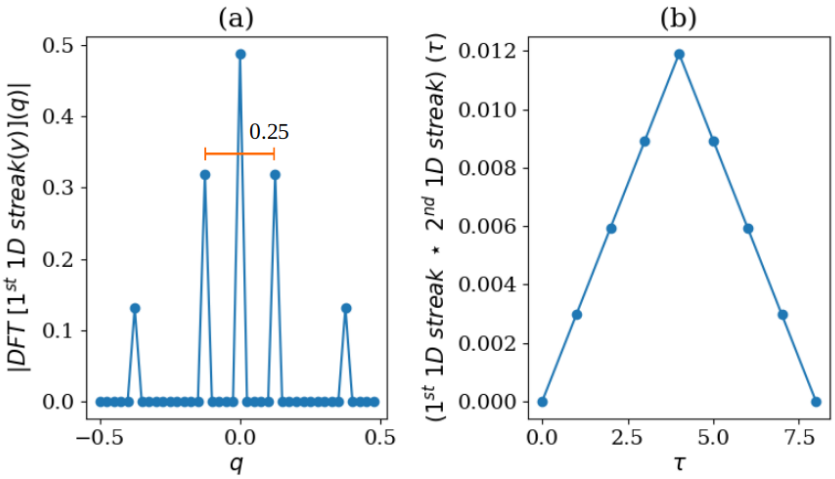

Figure 4.12: Λ estimation technique for bright debris streaks:
The debris streak has the same features as that of shown in Figure 4.6 i.e, $\Lambda = 4$, $FWHM = 3$ pixels, $\theta = 90°$.
a) The discrete Fourier transform of one of the double dashed streak. The distance between the secondary peaks is 0.25 which is essentially $1/\Lambda$.
b) The cross-correlation between both the single dashed streaks, showing a peak at $\tau = 4$.

The $FWHM$ corresponding to each debris streak was drawn from a uniform distribution of 3 to 9 pixels from which Q was calculated (cf. Eq. 3.7). The value of M was kept 3 times that of the $FWHM$ to make sure that both components of the double streaks are well separated from each other. Considering an image size of 4096×4096 pixels and SNR_{max} ranging from 1 to 25, dashed double streaks were generated on each image against a Gaussian noise having σ of 100 ADUs. Applying our proposed strategy leading to the detection of debris streaks on each image was achieved in ∼120 seconds on a machine having 64Gb of RAM at 2.3GHz clock speed.

The ROC curve, estimating the probability of true SNR_{max}, ϕ and bottom position of the streaks is shown in Figure 4.13. The area under the curve (AUC) is 0.87, which suggests that the detection method is quite effective. After looking at the plots in Figure 4.14, we are convinced that a much better detection probability is achieved for the streaks having $SNR_{max} \geq 9$ with the exception for the prediction of the Λ values. Fig. 4.14d(d) shows that a debris streak has to be brighter, specifically $SNR_{max} \geq 15$, in order to achieve a reliable prediction for Λ.

In this chapter, we have proposed and demonstrated a potential new observation technique to derive the angular velocities of space debris independent of TLE information. We have come up with the idea of modifying the charge transfer strategy in TDI imaging, resulting in the formation of

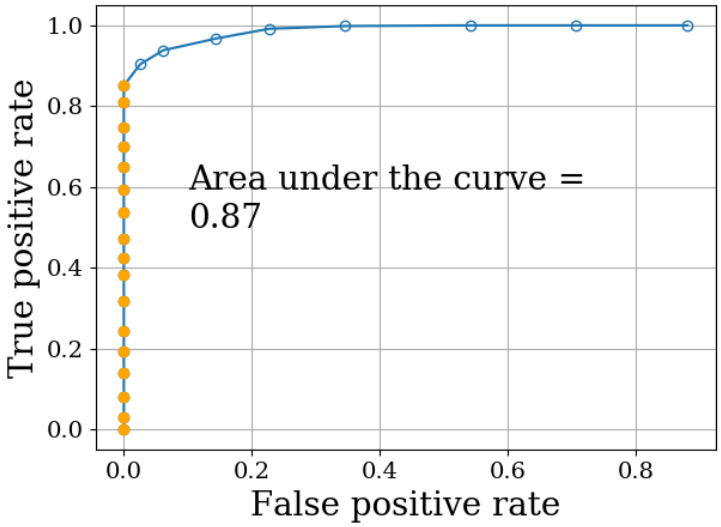

Figure 4.13: ROC curve for the detection of the debris streaks. The filled circles refer to the TPR vs FPR for a $SNR_{max} \geq 9$.

dashed debris streaks where each dash is correlated to the angular velocity of the detected debris. Several methods to estimate the length of each dash have also been discussed, among which matched filtering has shown a superior performance. Using the 4-m ILMT, the objects at LEO or MEO can be characterized. If we consider the TDI observations carried out with DFOT (see Tab. 2.2) as a reference, the angular velocity of 10 over 13 cases could be conveniently calculated using our proposed technique (see the table below).

Table 4.1: Probable statistical numbers for the characterization of space debris with the ILMT

Approximate angular speed ("/sec)	N° of space debris	Λ (pixels)
30	3	2.3
500	3	38
1000	5	76
1500	2	115

The values of the 'Approximate angular speed' of the space debris have been arbitrarily assumed. The values in 'N° of space debris' have been taken from Table 2.2 where each value corresponds to the number of detected debris having angular speed (v) close to the respective 'Approximate angular speed' value. The values for Λ have been calculated by multiplying the integration time P for the ILMT with the 'Approximate angular speed' and dividing the result by the pixel scale (sc) of the ILMT CCD camera.

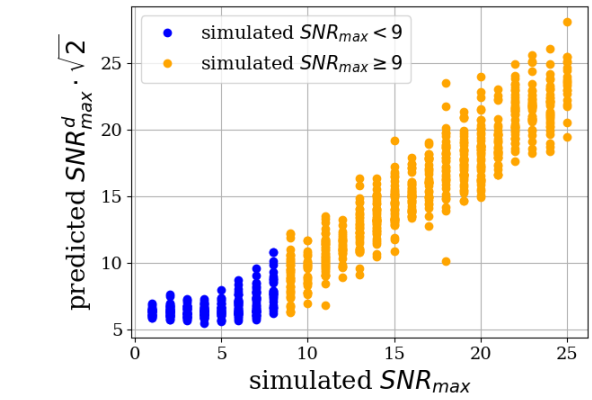

(a)

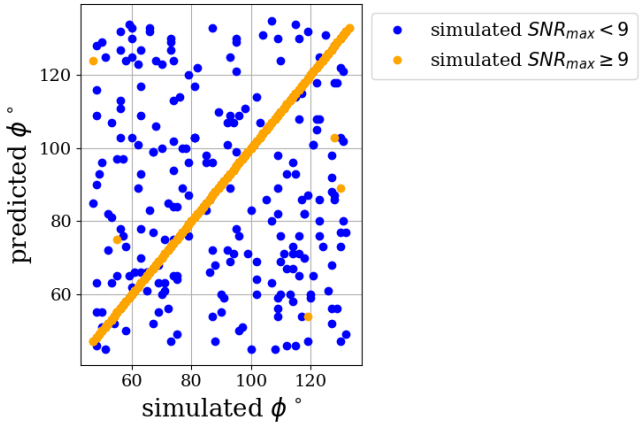

(b)

Figure 4.14: Comparison of simulated SNR_{max}, $FWHM$, inclination angle (ϕ), the bottom location of the streaks along the CCD columns and streak dash length (Λ) in the synthetic images with their corresponding estimated values from streak detection. It is to be noted that the predicted SNR^d_{max} is multiplied by $\sqrt{2}$ to make it comparable to the corresponding simulated SNR_{max}. (cont.)

.

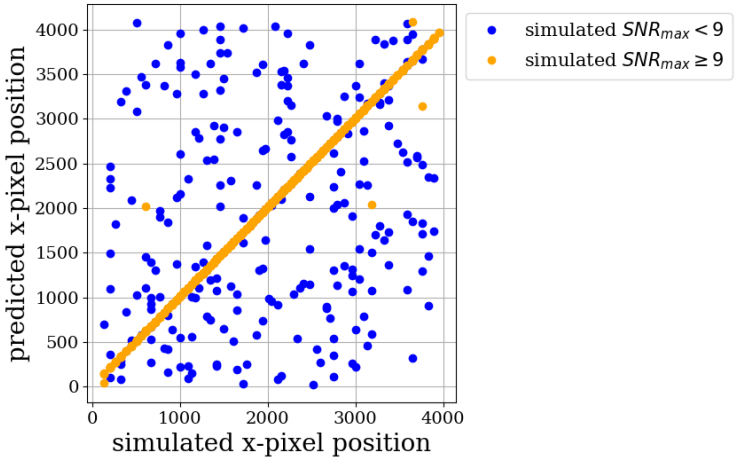

(c)

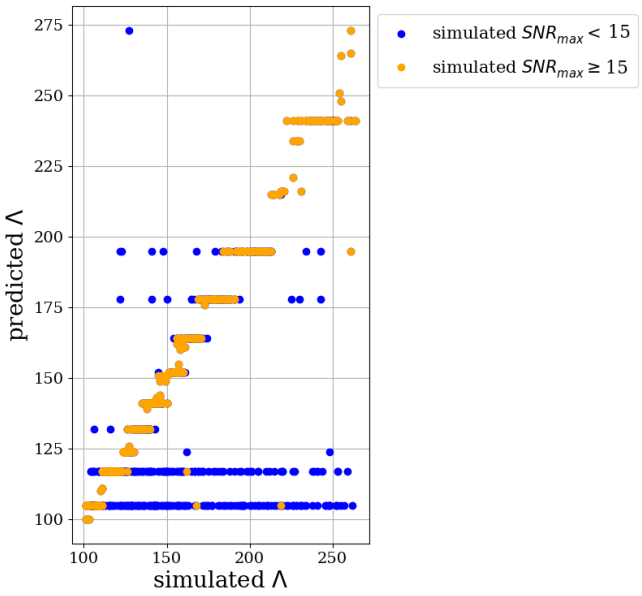

(d)

Figure 4.14: Comparison of simulated SNR_{max}, $FWHM$, inclination angle (ϕ), the bottom location of the streaks along the CCD columns and streak dash length (Λ) in the synthetic images with their corresponding estimated values from streak detection.

5

ILMT CONSTRUCTION AND FIRST LIGHT

The 4-m International Liquid Mirror Telescope (ILMT) is in its final stage of construction on the ARIES site in Devasthal (Uttarakhand, India). We describe and illustrate hereafter its different components. The ILMT will be used in the Time Delayed Integration (TDI) mode to carry out a deep survey and high S/N photometric and astrometric observations of solar system, galactic and extra-galactic objects within a narrow (24') strip of sky. It will also detect numerous space debris (Pradhan et al., 2019).

The infrastructure of the ILMT building primarily consists of a telescope room, a data/control room and a compressor room (see Figure 5.1). The telescope dome hosts a 4-m primary mirror, the mechanical structure supporting the prime focus with a corrector lens + CCD camera setup, an air-bearing and a mercury handling system. Inside the data/control room, all the observatory control system is present which comprises an electric cabinet for the control of the air-bearing rotation, a filter-sensor module which ensures a proper air supply to the air bearing and several industrial computers operating all the electronic components related to the ILMT. The compressor room hosts two compressors along with two storage tanks and two air filter-drier modules.

In the framework of this PhD thesis, we have monitored and participated in the installation of all the components of the ILMT which includes the assembling of the metallic pillars inside the telescope building to hold the prime focus, the fitting of the air-bearing and the 4-m primary mirror on top of it, the installation of the air-flow system from the compressors to the air-bearing, the corrector lens positioning with the CCD camera, the setting up

of the observatory control system and the building operation safety mechanism. The operational period of the ILMT will be 6 to 7 months per year for five years. Though the observation will only be carried out during the night, the mirror will remain functional continuously to avoid the Hg-surface formation at the starting of the mirror rotation which typically takes ∼4 hours. The state-of-the-art telescope system requires least human involvement and will allow a person to operate the whole observatory remotely.

Figure 5.1: View of the ILMT telescope room, data/control room and compressor room.

5.1 Mirror and corrector lens alignment

According to the telescope design, the rotation axis of the mirror should pass through the center of the corrector lens setup, both these components should be perfectly horizontal and the azimuth of the corrector lens setup should be aligned along the N-S direction. In this section, the details on the actions performed to achieve the desired settings are discussed.

Before making any adjustment to the alignment of the mirror or the corrector, we set the proper distance between them. Theoretically, the distance between the bottom of the first lens (the biggest one) of the optical corrector and the center of the primary mirror is 7200 mm. So, the metallic structures

holding the prime focus were lowered and the desired distance between the mirror and the first optical lens of the corrector was properly achieved.

5.1.1 Positioning of the 4-m primary mirror

For a safe operation of the system driven by an air-bearing, it has to have hydrostatic stability. The 4 meter primary mirror structure of the ILMT rests on the air-bearing with the help of two stainless-steel interface plates (one attached to the mirror structure and another lying directly on the air-bearing, see Figures 5.2 and 5.3). The steel interface plates with an interface radius of 10 cm, helps the 4 meter primary mirror (∼300 Kg) to rest on the air-bearing and prevents any kind of physical damage to the aluminum body of the air-bearing. The interface radius is well within the tilt capacity of the air-bearing but it does not have a perfect ground flat finishing. So a slight misalignment between the two steel plates may raise concern about the proper functioning and safety of the rotating mirror which will carry about 550 Kg of mercury during the operational period.

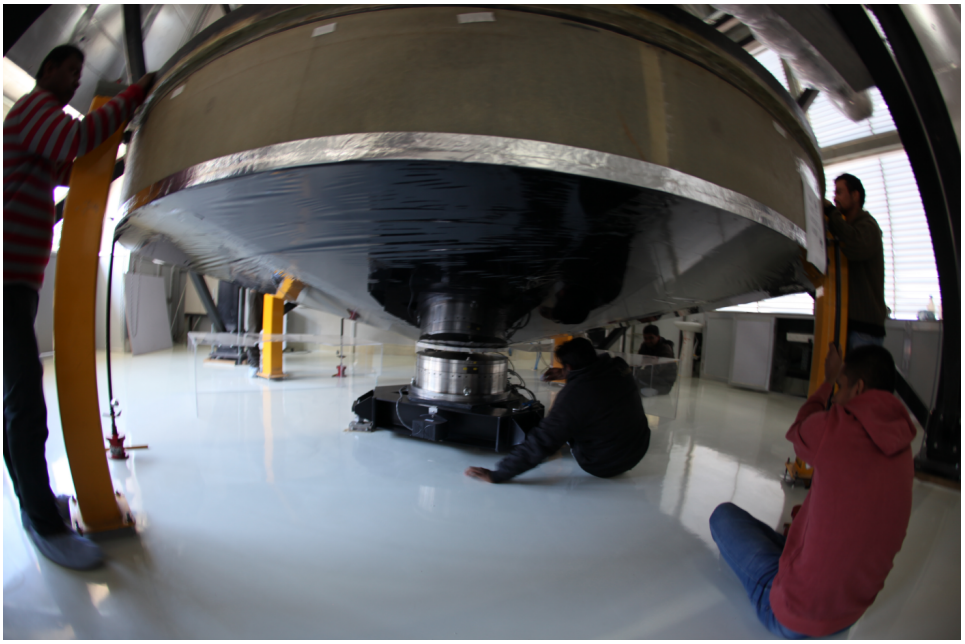

Figure 5.2: Fish eye side view of the 4 meter primary mirror resting on the air-bearing. The four yellow pillars are the safety pillars to protect the primary mirror from tilting.

The mirror and the air-bearing were shipped to Devasthal, India and it was lying idle for a few years. This situation encouraged us to check for the current physical impact of the mirror structure on the air-bearing (tilt stiffness), surface level variations of the mirror (vertical run out) and edge

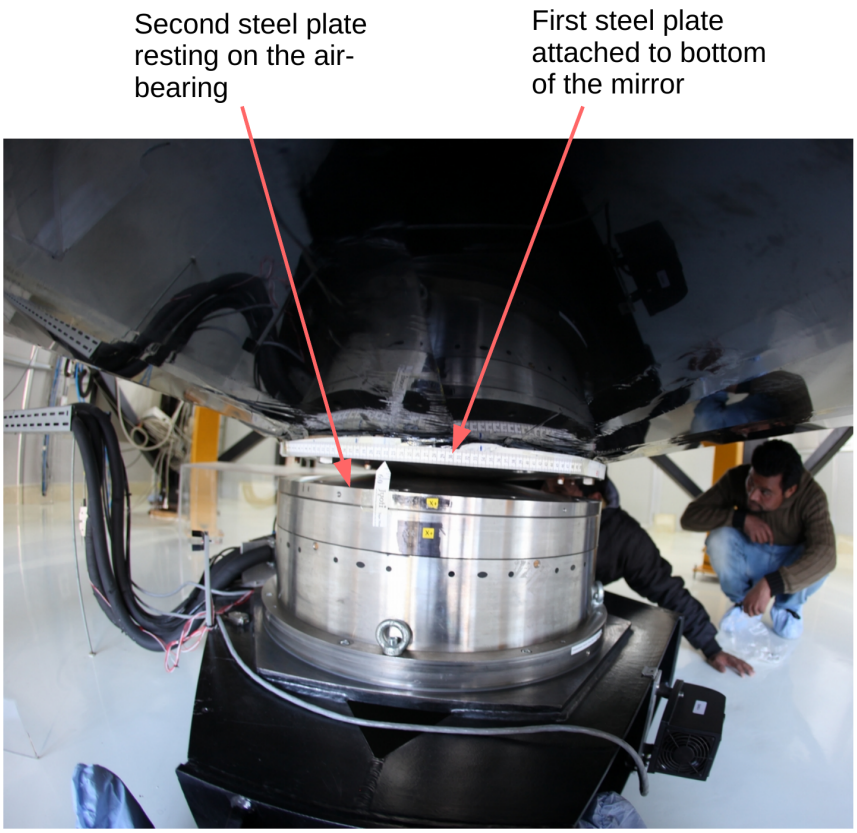

Figure 5.3: Arrangement of the stainless steel interface plates between the primary mirror and the air-bearing. The $X+$ and $X-$ symbols are printed on the steel plates in yellow to know their relative orientation. The alignment of $X+$ of the upper steel plate to $X+$ of the lower steel plate is considered as the 0° alignment.

variation of the mirror periphery (lateral run out). The arrangement of the air-bearing and the primary mirror achieved by aligning the $X+$ marks (see Figure 5.3) on both the steel plates was considered as 0° alignment. We lifted and aligned the mirror at different orientations (e.g. +180°, +90°, +5°, -4.8°, -3°, +2.6°, +1.4°, -1°) with respect to the air-bearing with the help of car jacks. The primary mirror was marked with numbers 1 to 24 representing 24 sectors with each sector covering 15°. We took several measurements of the tilt stiffness, vertical run out and lateral run out for each different orientation of the two interface plates and at each sector to find the best alignment. For a reliable operation, the tilt stiffness of the primary mirror system has to be safely above a critical tilt stiffness (∼1.677 Nm/μ rad for the ILMT in fully operational mode). The stiffness at a particular place of the mirror can be calculated by applying a load at that place and then measuring its

vertical displacement due to tilting. We put a weight of ∼9 kilograms at different points on the peripheral rim of the mirror and measured the tilt with the help of two micrometers placed at the extreme ends (for a clear idea refer to the schematic representation shown in Figure 5.4). These kinds of measurements were done for different orientations of the air-bearing and the mirror. For the 0° or 180° alignment, the estimated stiffness readings were found to be the best. However, we could see no significant difference in the stiffness readings for slightly different orientations, for example, see Figure 5.5.

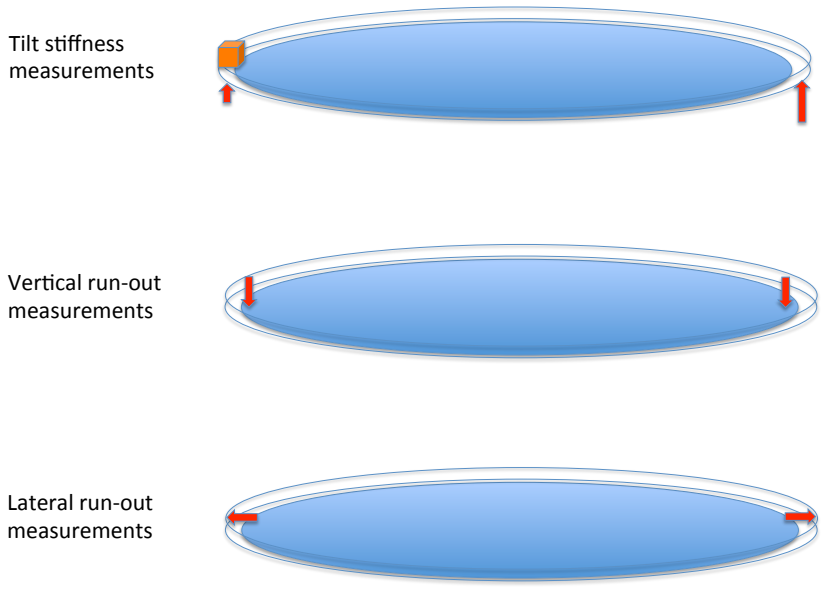

Figure 5.4: A schematic representation of tilt-stiffness, vertical run out and lateral run out measurements. The orange cube represents a weight and the red arrows represents the orientation of the pointer of analog micrometers.

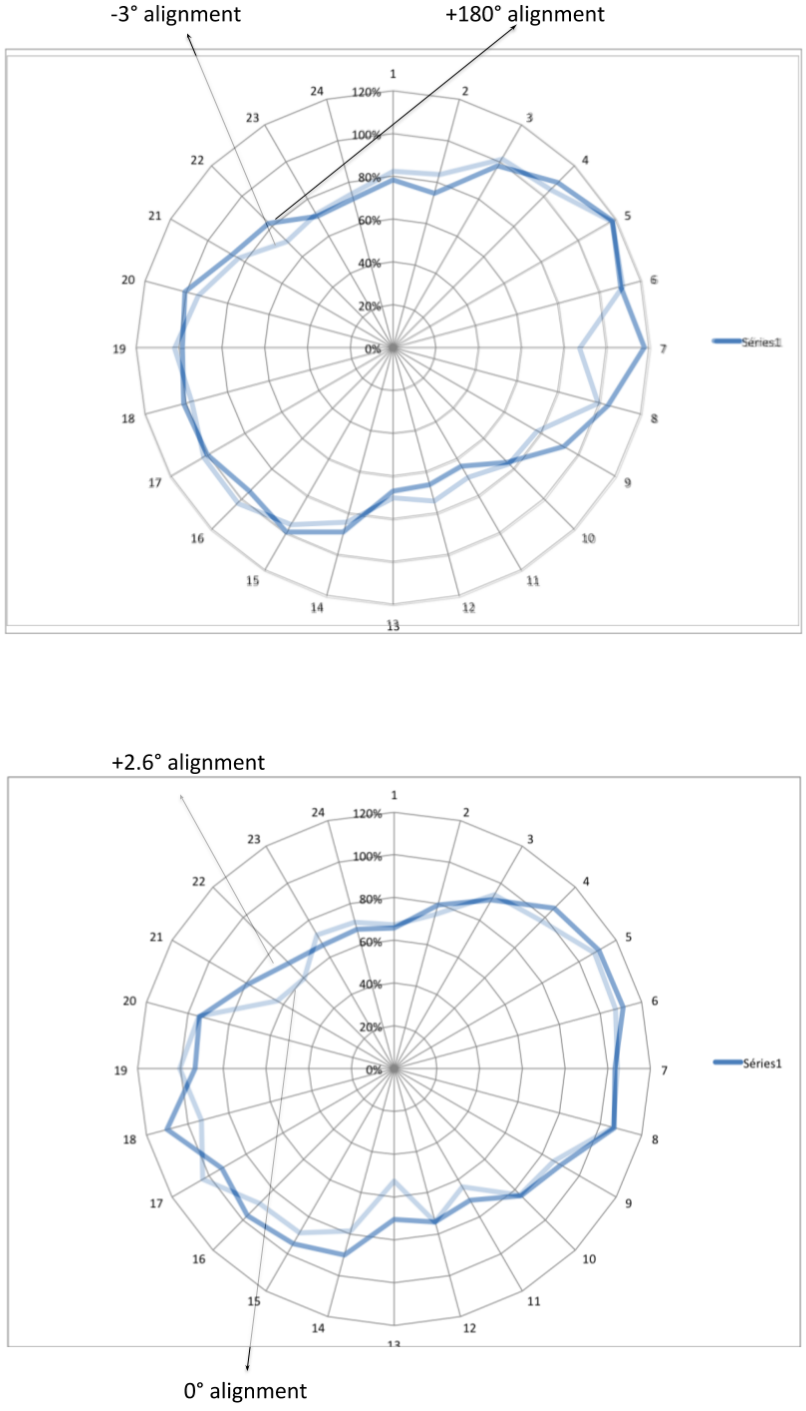

Figure 5.5: Tilt stiffness measurements for orientations slightly differing from 0° or 180°.

The surface of the primary mirror made of polyurethane and supported by axial metallic bars may experience deformation if the interface plates are not aligned optimally. When the ILMT becomes functional, this may lead to instability in the mirror rotation. To check for the vertical run-out we put the air-pressure on the air-bearing and took measurements of surface level variation (as shown in Figure.5.4) for different orientations and at different sectors with the help of micrometers. The vertical run-out measurements showed a minimum dispersion at the 0° orientation (see Figure 5.6).

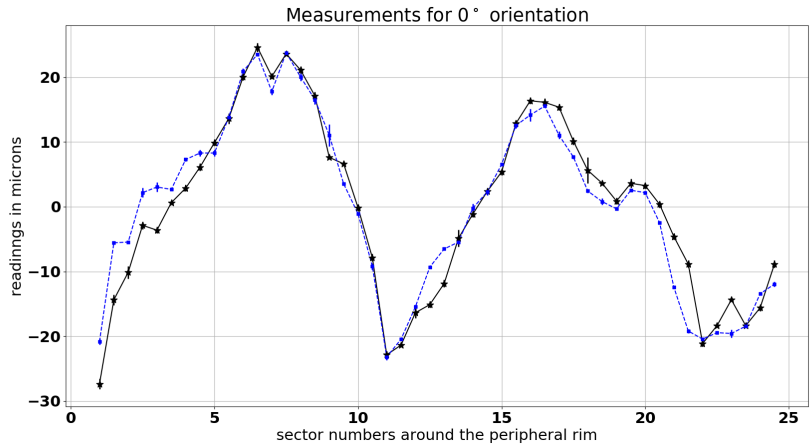

Figure 5.6: Vertical run-out measurements at the 0° orientation.
For better reliability, the measurements were taken twice for each sector, represented in blue and black colors in the concerned plots.

We suspected that the periphery of the mirror structure may get deformed radially. So we took measurements of lateral variation of the outer rim of the mirror as explained in the schematic Figure 5.4. Here also the measurements were taken twice for each sector and represented in same fashion as that of vertical run-out measurement plots in Figure 5.7. However, the measurements of lateral run-outs could not help make any conclusion because they did not show any kind of systematic trend for different orientations.

From the tilt stiffness, vertical and lateral run out measurements carried out for various relative positions of the bowl with respect to the air bearing, only those for an angular offset near 0° are acceptable in terms of vertical run out. All around the 0° angular offset, the tilt stiffness measurements seem not to be sensitive at all to the precise positioning. Therefore, paying most attention to the vertical run out measurements, the optimal offset turns out to be 0°.

For a stable rotating mirror system, the axis of rotation should be perfectly aligned with respect to the local gravitational field. To achieve such

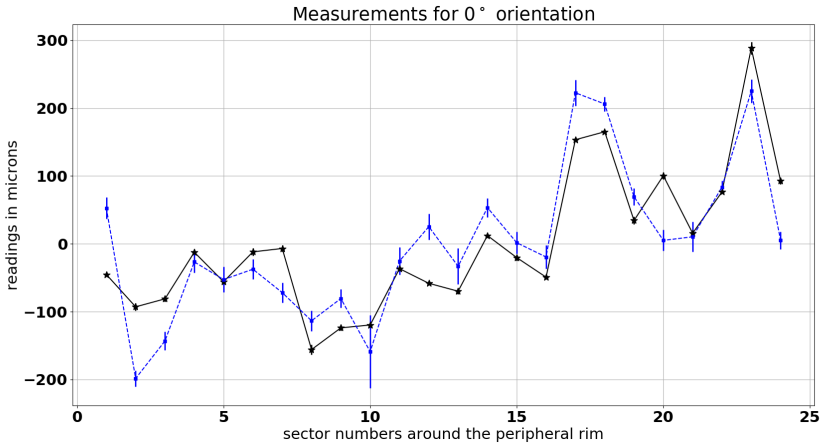

Figure 5.7: Lateral run-out measurements for different orientations.

an adjustment, we have proceeded as follows. Initially a flat machined aluminium plate was placed near the center of the primary mirror. A 2" precision spirit level was put on top of it (see Figure 5.8 (a)). We then adjusted the three screws which support the air bearing in such a way that the central bubble of the spirit level stayed at the same relative position while rotating the mirror around its axis (see Figure 5.8 (b)). After several adjustments, it was found that the optical axis of the mirror was deviating from perfect verticality by less than 0.4 arc-seconds.

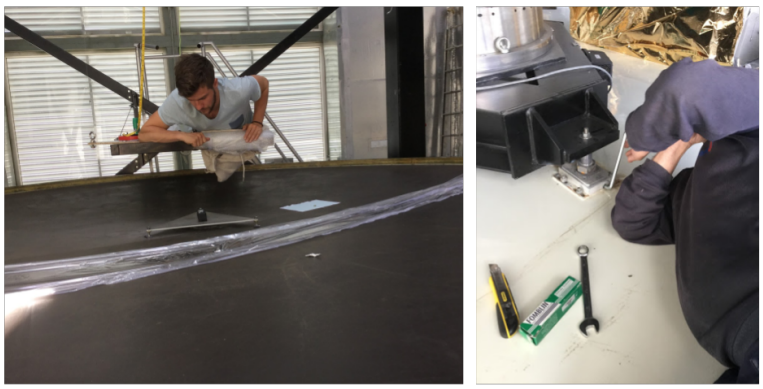

(a) (b)

Figure 5.8: Image on the left shows a spirit level (black) set on a flat aluminium plate close to the mirror center.
The picture on the right was taken while adjusting the tilt of the air-bearing by means of three screws separated by 120° with respect to its center.

5.1.2 Positioning the corrector lens

As the mirror is parabolic, the off-axis imaging becomes blurred due to coma aberration and astigmatism (Schroeder, 1999). The trajectories of the celestial sources passing over the field of view of the CCD camera are curved, but the TDI imaging technique shifts the electronic charge along the CCD columns along a straight line. In addition to it, the angular velocities of the sources in the sky varies as a function of their declination which does not allow the TDI rate to be fixed (at the sidereal rate) through out the field of view. To compensate for these effects, an optical corrector designed by Hickson and Richardson, 1998b has been placed before the CCD camera. The structure of the corrector lens system shown in Figure 5.9 (b) & (c) is not symmetric and the whole set up is built in such a way that it has to be kept perfectly horizontal and correctly set in azimuth.

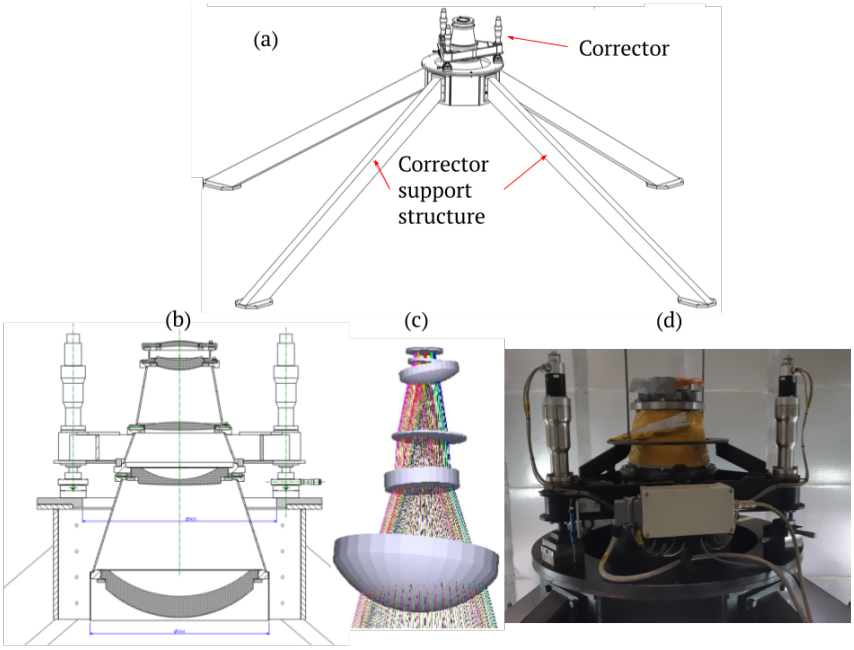

Figure 5.9: Corrector structure drawing and the front view.
(a) Drawing of the corrector setup placed at the prime focus supported by four metallic bars.
(b) Drawing of the cross-section of the corrector setup showing the complex 5 lens system highlighted in dark shade.
(c) Zeemax model of the lens system.
(d) Front view of the corrector structure placed at the prime focus.

During the installation of the ILMT, the corrector lens along with the mechanical structure holding it, was initially not well aligned with respect to the N-S direction. So, it was rotated manually to bring an inbuilt mark on

the mechanical structure indicating the S in perfect alignment with the N-S direction. This proper alignment was made by looking at the shadow of a hanging pendulum from the roof top of the ILMT building at local solar noon (see Figure 5.10 (a)). To make even a better alignment, the same procedure was repeated. The final best alignment can be seen on Figure 5.10 (b).

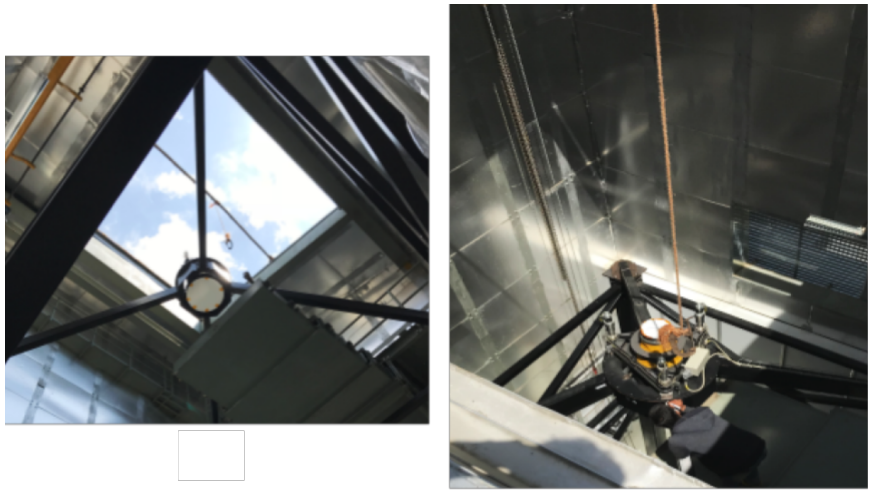

Figure 5.10: Adjusting the corrector structure's azimuth.
(a) A hanging pendulum from the roof of the ILMT telescope on top of the corrector lens was installed at the prime focus building during local noon.
b) The shadow of the pendulum falling on the corrector lens indicates the N-S direction at local noon.

Then we built a simple strategy to place the corrector setup horizontally. Here, the idea was to use a high precision spirit level placed on the corrector and use its electro-mechanical tip-tilt adjustments (see Figure 5.9 (a), (b) & (d)) to set the flatness. However, the challenge was the insufficient space on top of the corrector setup to put a spirit level and the inaccessible top view of the whole set up along with the spirit level. So a frame was manufactured to hold a web camera and a metallic cap was shaped with high accuracy of flatness to accommodate the spirit level on the corrector setup without making any damage to it (see Figure 5.11). The status of the spirit level with 0.01 mm/1 m accuracy could be accessed remotely via a webcam and a mini-computer. Then by adjusting the tip-tilt motion of the corrector structure and bringing the bubble levels to a fixed position for different orientations of the spirit level, we could place the structure horizontally with a precision of $\sim$2".

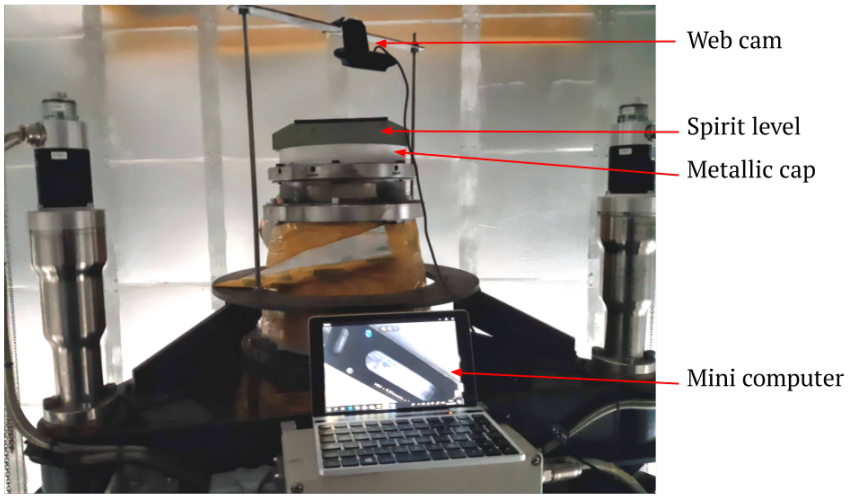

Figure 5.11: Arrangements to make the corrector structure perfectly horizontal.

5.1.3 Aligning the centers of the primary mirror and the corrector structure

We first tried to spot the center of the primary mirror by identifying the precise point on its surface that remained fixed during its rotation. Based on this idea, we put a millimeter paper on the back side of a plexiglas plate very near the mirror center. Then a web camera was placed just over it to record the motion of each millimeter square of the graph paper and hence to identify the most motionless square corresponding exactly to the center of the mirror. In addition, we used the digital magnification of the web camera such that the center of the mirror could be estimated with a precision better than two tenths of a millimeter. See Figure 5.12 to better comprehend the configuration.

Determining the position of the optical corrector lens center surrounded by several mechanical structures at the prime focus was not so trivial. We built a strategy to make use of the baffle located around the corrector lens which has a cylindrical symmetry to determine the center. Initially three nylon wires were hanged separated by 120° around the baffle. An equilateral triangle was then manufactured in wood by ourselves which could fit perfectly inside the circular base of the cylindrical baffle. Then each corner of the triangle was attached to one end of a nylon wire. We then assumed that

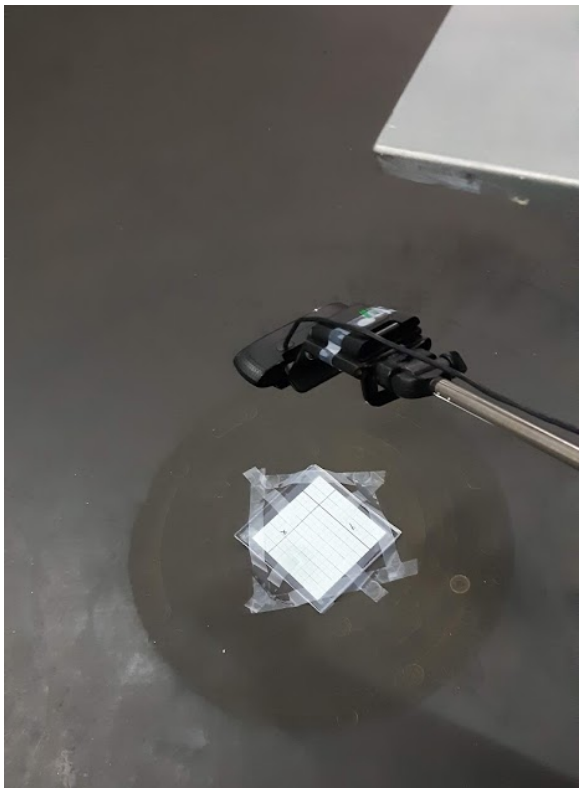

Figure 5.12: Millimeter graph paper placed on the back side of a plexiglas plate near the center of the bowl and live streamed via a web camera.

the center of the horizontally positioned triangle should correspond to the center of the corrector lens. Please see the proposed design in Figure 5.13 and the actual set up in Figure 5.14. A plumb-bob was then hanged from the center of the equilateral triangle towards the surface of the bowl where the millimetric graph paper was already placed (see Figure 5.14). We then used the z-axis or focus movement of the corrector lens to lower the plumb-bob and the impact point of the tip of the plumb-bob covered with some paint indicated the location of the corrector lens center with respect to the center of the primary mirror (see Figure 5.15).

After estimating the centre of the primary mirror and of the corrector lens, our goal was to achieve their alignment by moving the corrector lens center towards the primary mirror center. Initially a laser pointer was installed at the corrector lens structure pointing vertically towards the mirror. Then the sliders on the corrector lens (see Figure 5.16) were used to induce linear motions of the corrector lens. By adjusting the sliders, the motion of the laser point was traced and a correlation was established between the displacement of the laser dot at the mirror plane as a function of the slider movement. Based on the positions of the center of the mirror and corrector

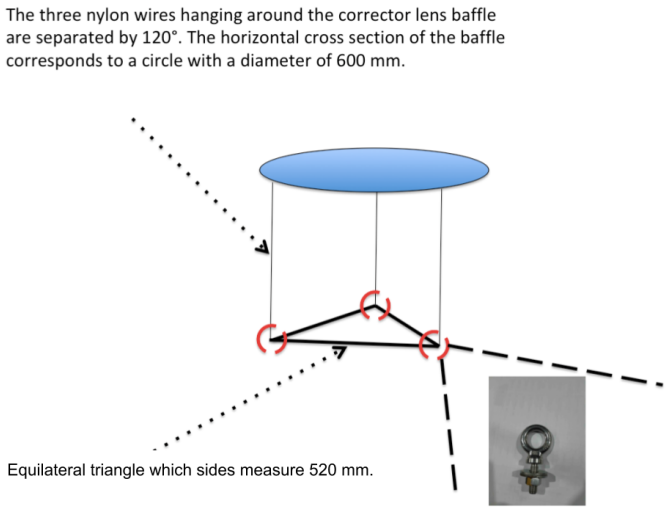

Figure 5.13: Schema of a design to determine the center of the corrector lens.

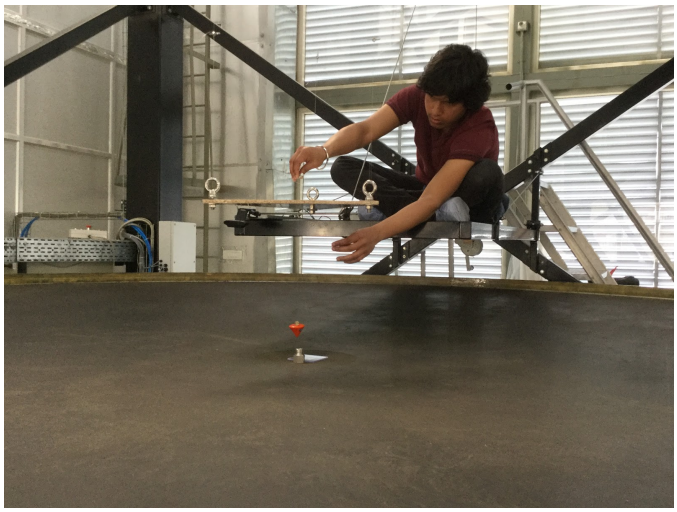

Figure 5.14: Setup to determine the center of the corrector lens.
In this figure, we can see a hanging equilateral triangle above the primary mirror and a plumb-bob hanging from the center of the triangle.

lens, the sliders were adjusted. Subsequently, we repeated the procedure described in the previous subsection to determine the position of the center of the corrector lens. It was found that, we could align the centers of the mirror and of the corrector lens with a precision better than 1 mm. This alignment was then fine tuned by using a laser pointer. The pointer was kept on the mirror surface pointing towards the edge of the first corrector lens (see Figure 5.17). If the center of the mirror and that of the prime focus

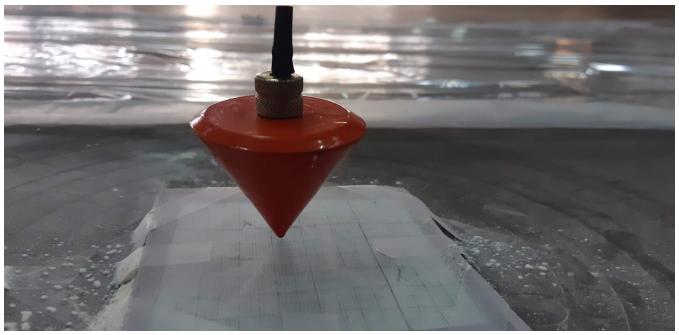

Figure 5.15: The tip of the plumb-bob touching the graph paper on the primary mirror indicates the center of the corrector lens. The tip was covered with some thick paint.

were aligned, then the laser dot should remain along the edge of the lens when the mirror is being rotated. In this way we could confirm and slightly improve the relative centering between the primary mirror and the corrector lens.

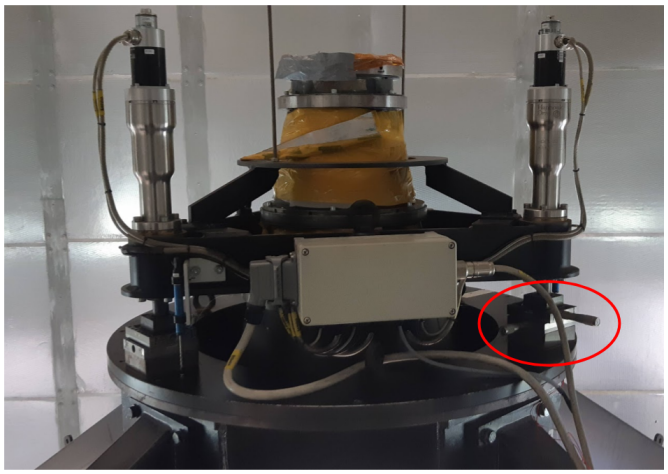

Figure 5.16: Two orthogonal sliders on the corrector lens setup for inducing a linear translation of its center.

Figure 5.17: Image on the left shows a laser pointer kept on the primary mirror. The other image shows the green laser dot at the edge of the corrector lens. During rotation of the mirror, th laser dot remained on the edge of the corrector lens.

5.2 Control systems

There are several subsystems to keep the telescope functioning properly which can be categorized broadly into the pneumatic systems (PS) and the electrical/electronic systems (EES). The sole function of the PS is to provide continuous supply of pressurized clean air to the air-bearing. The EES consists of the electronic devices such as the air-bearing rotation system, compressor system, the CCD camera system, Hg handling system and the dome operating system.

5.2.1 Pneumatic systems

The air-bearing rotor system is equipped with two types of thrust circuits, one supporting the vertical load of the rotating dish with Hg, known as axial thrust and another circuit which maintains a fixed position of the rotor with respect to the stator during the rotation also known as radial thrust. The operating pressures required for the axial and radial thrusts are ∼7 and ∼3 bars, respectively. The two compressors (*Compair L07-13A*) inside the compressor room are operated to provide an uninterrupted supply of compressed air to the air-bearing in case of a compressor failure. Both compressors generate air having 12 bars of pressure which are fed to two storage tanks each having 500 liters of storage capacity, where the 1st stage of the air filtration occurs. The compressed air is cooled and the separated water particles from the air are condensed and collected at the bottom of the tank. Then the outlets of the two tanks are supplied to a 2nd stage filter and dryer modules inside the compressor room. The module consists of two parallel combinations of cascaded filters with a membrane dryer. The output of the filter-dryer module is fed to a filter-sensor module inside the data room equipped with a dew-point sensor , a pressure sensor and a flow meter. The design and installation of the 2nd stage filter and drier module and the filter-sensor module have been performed by Prof. Paul Hickson. The output of the filter sensor module again goes through a pneumatic system designed by AMOS which has got an air-drier and several filters. At this stage the required pressurized air is supplied to the air-bearing. The layout of the pneumatic system of the ILMT is shown in Figure 5.18.

Under the operating conditions of the air-bearing, the air is filtered and dried to such an extent that the dew-point temperature goes below -20°C with a flow rate of ∼130 l/min and thus, any damage to the air-bearing by water condensation or dust accumulation is avoided. The pressure-sensor module also ensures the supply of adequate air-pressure to the air-bearing.

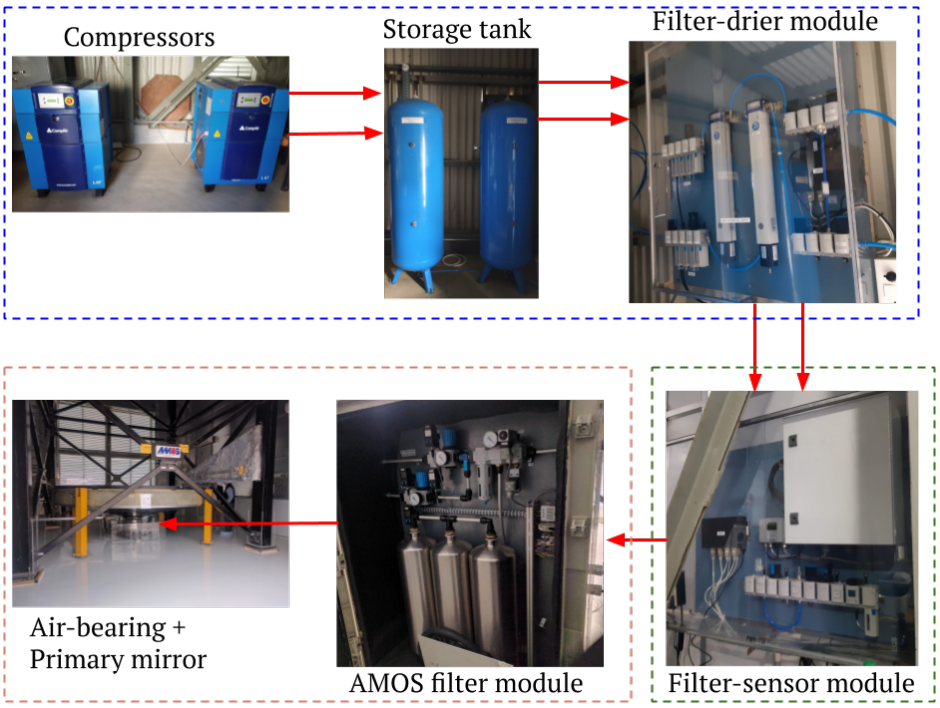

Figure 5.18: Pneumatic system of the ILMT.
The red arrow lines represent the pneumatic tubes connecting different systems. The systems covered by the coloured dashed boxes highlight their respective locations. The blue, green and orange boxes represent the telescope room, data/control room and the compressor room, respectively.

5.2.2 Electrical/electronic systems

The rotor speed of the air-bearing is monitored by 3000 encoders surrounding it. The signal from the encoders are compared to the pulses generated by a synthetic frequency generator in a close loop feedback system to maintain the rotational speed stability of the air-bearing. Borra et al. (1985) have prescribed a rotational period stability better than 10^{-5} for an optimal performance of a liquid mirror. With the current setup, we can achieve an rms rotation period variation of the order of 10^{-6}. The status of the air-bearing is accessed and regulated via a graphical user interface (GUI) which sends and receives signals from a programmable logic circuit (PLC) connected to the air-bearing system.

The compressors are set to automatic operation. This means that the compressor remains in stand-by mode (stops) when there is no consumption and automatically starts when the pressure at the beginning of the pneumatic line falls below 12 bar. The compressors come equipped with variable frequency drives (VFD) which reduce energy consumption, avoid power surges

(during the start of the motor) and provide a better constant pressure than any other compressor driving systems.

The ILMT CCD camera (Spectral Instruments, 2019) is equipped with a 4K×4K E2V CCD 231-84-1-E06 chip (e2v, 2009) capable of TDI imaging. The CCD is cryo-cooled by a compressor (at the floor of the telescope room) with braided stainless steel lines running to the camera head at the prime focus. The camera is maintained at -110°C to eliminate dark current. A link is established to the camera from a computer inside the data/control room via a fibre optic line for readout operations. Three SDSS equivalent filters (g', r', i') are deployed with the CCD camera. An independent set of movements such as a tip-tilt motion, azimuth rotation, focus adjustment motion and linear motion to change filters are provided with the help of a mechanical interface. The motions in the interface can be controlled remotely with the help of a control panel exclusively dedicated to the interface. We have developed a software in Visual Basics to monitor the interface. The camera set-up along with the interface is shown is Figure 5.19.

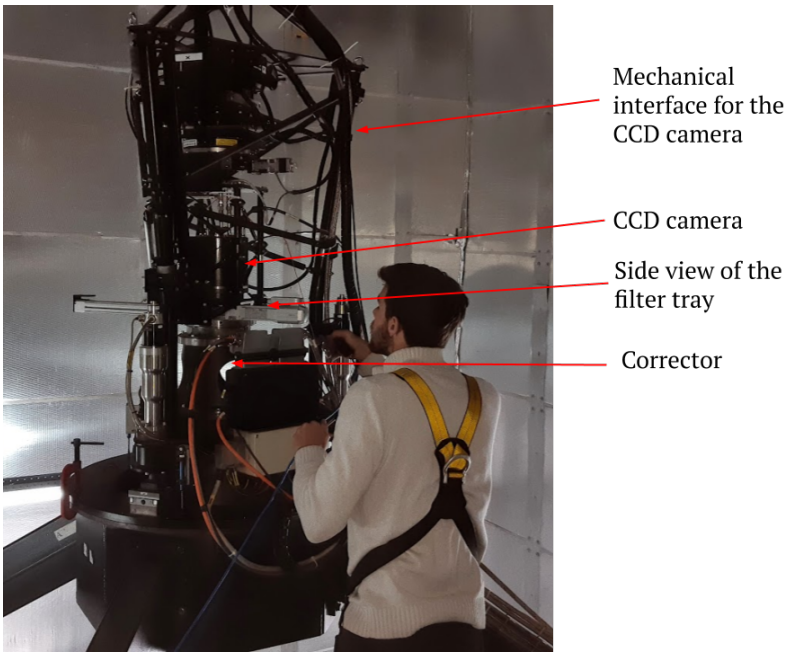

Figure 5.19: The ILMT CCD camera set-up.

The mercury handling system (see Figure 5.20) is composed of a stainless steel arm which pours the liquid Hg into the mirror as well as drains out the mercury from the mirror when necessary. The mercury is transferred to and from a stainless steel container having ∼500 Kg of mercury with the help of a peristaltic pump. One end of the arm is hinged to a metallic pillar and the arm can be moved to place the other end on or away from the primary

mirror. The loose end of the arm is equipped with a linear translation device integrated to a couple of end-stop sensors for placing the open end of the pumping tube close to the center of the primary mirror.

Figure 5.20: Panoramic view of the stainless steel tank (on the right), cylindrical peristaltic pump (close to the tank), pump controller (in front of the tank), and a black hose running through the metallic arm down to the center of the primary mirror.

The dome operating system incorporates many devices such as a hatch cover at the top of the telescope building to provide access to the sky around the zenith, telescope room cooling system (exhaust fans & air-conditioners) to reduce temperature gradient, lighting inside the telescope room, a weather station and a GPS module. All these instruments can also be controlled remotely with help of the relay circuits integrated with a micro controller.

An observatory control software (OCS) has also been developed which contains several modules to communicate with the telescope, compressors, dome, weather station and pneumatic sensors via a hardware interface. It stores the weather information, monitor the autonomous operation of the observatory and performs requested operations from an external user.

5.3 Safety features

There have been several measures taken to eliminate mercury contamination with the surroundings. A large amount of vapour is created while pouring the mercury into the mirror and spreading the mercury over the primary mirror to form a continuous reflecting surface. However, after a stable reflecting surface is formed, the upper layer of the mercury becomes oxidized and stops emitting vapours.

We have used mylar films to cover the primary mirror. By doing so, the mercury vapour is prevented to escape from the mirror, the mirror remains protected from dust or insects and any friction between the mercury surface and the air located just above is annihilated to remove turbulence while the mirror is rotating. In fact, the harmful Hg vapours are sucked through a

hole near the mirror center with the help of a vacuum cleaner like system discussed below. Having a great optical quality, the thickness of the mylar sheet is just of a few microns, which makes it very fragile. An efficient technique has been developed by us to laminate the whole mirror at once (see Figure 5.21), and thus the risk of damaging the mylar film is reduced.

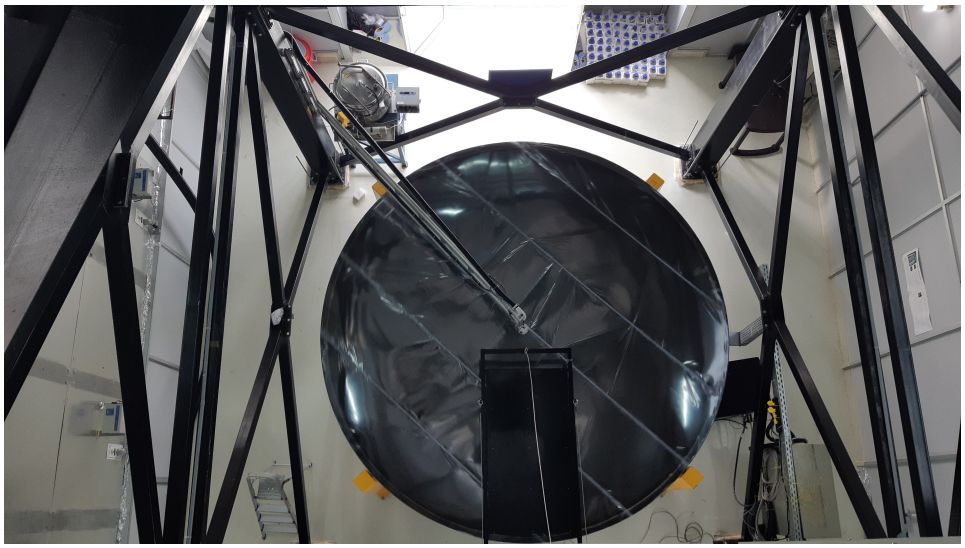

Figure 5.21: Top view of the ILMT primary mirror laminated with the mylar film.

A mercury vapour extractor has also been designed by us and manufactured by the mechanical workshop of Liège University, having a powerful pump and activated charcoal filter. It has been installed inside the telescope room close to the primary mirror (see Figure 5.22). Its inlet is placed just over the center of the primary mirror and the outlet is ducted through one of the dome's exhaust fans. When powered on, the Hg vapour extractor sucks the Hg vapour coming out of the primary mirror and neutralize the Hg content by filtering it through the activated charcoal. A small hole was made on the mylar cover near the center of the primary mirror so that the Hg vapour could be drawn out by the Hg vapour extractor.

The primary mirror is protected by four pillars (painted yellow) at its periphery to prevent any accident if the rotation becomes unstable. For such cases, emergency stops have also been provided at multiple places inside data/control room as well as the telescope room to stop the rotation of the air bearing.

All the operations involving mercury are done while wearing a mercury vapour proof mask, clean room apron, gloves, shoes covers and safety eye glasses. Every contaminated product is either disposed inside a dedicated container or decontaminated using sulphur and isopropyl alcohol. To prevent

Figure 5.22: Hg vapour extractor located on a brown platform at right. One end of the black pipe is connected to the extractor and the other end goes near the center of the primary mirror.

and quickly react in case of any mercury contamination, two Hg vapour detectors are engaged each inside the telescope room and the data/control room. An additional portable Hg vapour detector is also being used for the routine check around the telescope building.

5.4 Heading to the first light

In the month of April 2019, we finished setting up everything necessary for the functioning of the ILMT. Then we performed a few prerequisite checks before making the telescope operational. Pressure readings on the gauges at the compressor room and data room were checked. PLC status was checked to ensure proper functioning of the air-bearing. Proper insulation between the telescope room and data/control room was made. Connections between the CCD cooling compressor, CCD and CCD control system were established. The vapour detectors monitoring the Hg vapour concentration inside the telescope room and the data room were also activated. The Hg vapour extractor was switched on to neutralize the Hg vapour coming out of the primary mirror. From the vapour detector readings, we got assured about the fact that the contamination and danger due to the Hg vapour were eliminated (see Figure 5.23).

After all the safety checks, ∼34.8 liters of liquid mercury was poured into the mirror and subsequently the air-bearing rotary table was activated. The rotating mirror was then accelerated and decelerated using the air-bearing motor in order to spread out the mercury uniformly over the mirror surface. After several intense attempts, we could not succeed in closing the mercury surface. Holes were systematically appearing after some time near the periphery of the mirror. We then tried to accelerate and decelerate the mirror manually but also without success (see the sequence of pictures in Fig 5.24). Experimentally, it is observed that, to form a continuous mercury layer over the primary mirror having a diameter of 4 meters, a minimum initial average

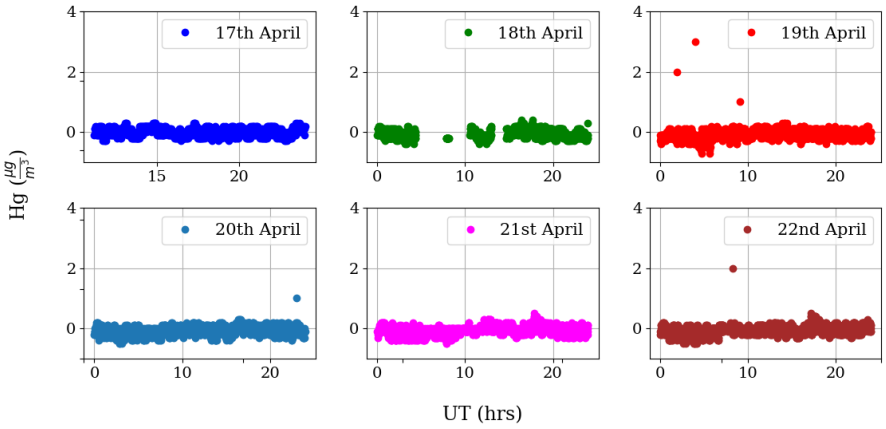

Figure 5.23: Hg vapour monitoring from 17th to 22nd of April, 2019, inside the telescope building during which mercury was poured into the mirror. Normally, when the Hg vapour concentration is less than 25 μg per cubic meter, one can work every day without wearing a mask during a shift of 8 hours. The Hg vapour concentration never exceeded 4 μg per cubic meter.

Hg thickness of 3 mm is required, translating into a minimum volume of ∼40 liters. So we lacked a minimum of ∼5.25 liters of mercury to form a stable mercury layer over the ILMT mirror. Moreover, the stiffness of the mirror structure may also have deteriorated in due course of time after its manufacturing in 2012. So we have planned to use 15 litres of additional mercury to overcome these issues and expect to achieve the first light in early 2020.

Now, we would like to highlight our personal contributions to the activities involved in the ILMT installation. All the installation processes have been monitored and reports have been prepared frequently which have been circulated subsequently among the participating members to keep them updated about the progress. We have also contributed to develop strategies for proper telescope operation and maintenance while training the technical team dedicated to the ILMT project at Devasthal. We have proposed protection system from the surge currents and lightnings during heavy monsoon to make all the electrical equipment safe. All the pneumatic tubes were installed connecting different parts of the pneumatic systems (see Fig. 5.18). Several small gadgets such as temperature sensors to monitor temperature gradient inside the telescope room, GPS systems to achieve accurate time readings, Hg vapour monitors installation/upgrading and automatic monitoring system as well as the design of the Hg vapour extractor have also been prepared by us. We have extensively carried out the primary mirror repairing using epoxy resins as well as the mirror quality tests which involved the

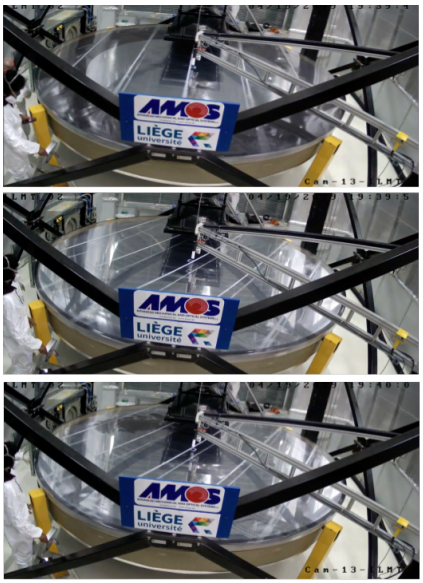

The Hg starts correctly spreading over the mirror after the mirror rotation is being accelerated.

The Hg surface is almost closed after frequent accelerations and decelerations are applied.

But after some time, the surface of Hg breaks (see the holes near the periphery at the top). This is a typical scenario when the quantity of Hg spread over the mirror is not sufficient.

Figure 5.24: Process of liquid mirror formation.

vertical run-out, lateral run-out and tilt stiffness measurements. The alignment of the rotation axis of the mirror and the center of the corrector lens were performed and a strategy was developed by us to place the delicate CCD camera with its mechanical interface above the corrector lens setup successfully. The safety features such as the mylar lamination, Hg vapour extractor and proper setups for mercury handling was also developed by us.

6

Future perspectives and conclusions

Optical observation of space debris constitutes an important asset, providing statistics on their number densities and sizes present at different altitudes. Zenith-pointing telescopes such as the ILMT can make a contribution in this area. Operating in TDI mode, observations will be carried out in survey mode and will be sensitive to any objects passing through the field of view.

In the context of obtaining the first light with the ILMT, once the adequate amount of mercury becomes available, we will perform optimization of the telescope setup to improve the image quality via mirror angular velocity adjustments as well as prime focus lateral, azimuth and tip-tilt adjustments.

With the subsequent optical observations recorded in the TDI mode, we intend to implement the proposed charge transfer strategy to determine the angular velocity of the passing debris overhead. As the first phase, the value of M will be kept to 1 which means that every pixel column in the CCD chip will integrate up to 2P seconds before shifting the accumulated charge into their second next column. We expect to recover the information on the angular velocity from the detected streaks using our proposed matched filtering technique, provided good seeing conditions will prevail.

On the other way, there have already been several ground based wide field optical astronomical surveys (e.g. the Sloan Digital Sky Survey, Canada-France-Hawaii Telescope Legacy Survey, etc.) as well as many will be commissioned soon. The enormous data obtained from these surveys certainly contain many debris streaks which are till today being ignored. Deep learning has been proven to be the most efficient technique for feature extraction and classification when a huge amount of data is involved. We are

planning to make use of this class of machine learning techniques to detect streaks of variable geometry and brightness in some of these existing surveys.

In Chapter 2, we have performed a test study for debris detection using the 1.3-m DFOT operated in the same TDI mode as that planned with the ILMT. The efficient data reduction technique applicable to the TDI frames provided a photometric precision of 0.04 magnitudes and astrometric precision of approximately 0.1 arcsec for point like objects. Twelve debris were successfully detected visually in the form of streaks on the CCD images and identified using the TLE information. It was demonstrated that the effective optical size of the detected debris can be derived by modelling them as hybrid diffuse-specular Lambertian spheres. The detection threshold of DFOT could be used to set an upper size limit to fainter debris which have crossed the field of view of the DFOT CCD but were not visually detected. The 4-m ILMT telescope, with its 22-arcmin-square field of view and fainter detection threshold, should be able to detect many more space debris, down to a size of approximately 5 cm in low Earth orbits.

A comprehensive overview of the matched filtering technique leading to the faint debris streak detection in the CCD images has been provided in Chapter 3. Theoretically, we have shown the optimization of the SNR of a debris streak using the matched filter technique. We took advantage of the discrete Fourier transformation to perform the matched filtering in the Fourier space , resulting in a much faster processing time without compromising the effectiveness of the detection technique. We have also used the wavelet based contrast enhancement technique to improve the detection efficiency by increasing the contrast of the faint streak with respect to the background noise which can be used to visualize and confirm the detection of the faint streaks typically having SNR_{max} more than 10. Monte Carlo simulations were performed to evaluate the proposed detection method efficiencies. We have also used and compared a few other existing detection techniques such as the Hough and Radon transformations. We found that the sensitivity of our proposed technique is better than the others.

During practical observations, many background sources will appear on the CCD images other than the streaks due to the presence of stars, galaxies, etc. So, these unwanted signals should be removed from the image to minimize any false streak detection. To achieve this goal, we successfully used the difference image analysis technique (DanDia) on simulated as well as real astronomical images.

We noted that, the optical magnitude of the detected debris can not be determined unless they are identified from the TLE catalog. Hence, in Chapter 4, we have proposed a new TDI observation strategy to independently characterize the detected space debris by extracting the information on their angular velocities. This involves the segregation of a continuous debris streak into two parallel double dashed streaks by modifying the charge transfer scheme from one CCD column to the other. The length of each

dash from the resulting streak is correlated to the angular velocity of the detected debris. Again, the matched filtering technique in the Fourier space was demonstrated for a dashed double streak and found to be performing better than the other techniques to estimate the length of the dashes. A small statistics, based on the debris detection results with the 1.3-m DFOT has convinced us that the objects at LEO or MEO can be characterized using the 4-m ILMT.

In Chapter 5, we have briefly discussed the various installation stages of the ILMT telescope. The stability analysis of the primary mirror mounted on the air-bearing was done by taking measurements of the vertical run-outs, lateral run-outs and tilt stiffness of the mirror for its different relative orientations with respect to the air-bearing. The procedures adopted to align the rotation axis of the mirror through the center of the corrector lens while keeping both these components horizontal was also discussed in this chapter. The setting up of the pneumatic systems and the electrical/electronic systems necessary for the proper functioning of the ILMT were also highlighted. All the preventive measures for accidental mercury spillage or mercury contamination were listed. The effectiveness of the safety mechanism can be asserted from the Hg vapour detector readings during our last mercury related activities.

The images obtained from the upcoming ILMT survey are expected to generate a strong statistics on the debris population and their optical sizes and thereby to contribute to the space situational awareness which is a concern to every space industry and also relates to every human being on Earth.

APPENDIX

A

List of Publications

Bikram Pradhan, Paul Hickson, and Jean Surdej. Serendipitous detection and size estimation of space debris using a survey zenith-pointing telescope. *Acta Astronautica*, 164:77–83, Nov 2019. doi:10.1016/j.actaastro.2019.07.008.

Bikram Pradhan, Ludovic Delchambre, Paul Hickson, Talat Akhunov, Przemyslaw Bartczak, Brajesh Kumar, and Jean Surdej. Present status of the 4-m ILMT data reduction pipeline: application to space debris detection and characterization. *Bulletin de la Société Royale des Sciences de Liège*, 87:88–91, Apr 2018. doi:10.25518/0037-9565.7525.

Jean Surdej, Paul Hickson, Hermanno Borra, Jean-Pierre Swings, Serge Habraken, Talat Akhunov, Przemyslaw Bartczak, Hum Chand, Michaël De Becker, Ludovic Delchambre, François Finet, Brajesh Kumar, Anil Pandey, Anna Pospieszalska, Bikram Pradhan, Ram Sagar, Olivier Wertz, Peter De Cat, Stefan Denis, Jonathan de Ville, Mukesh Kumar Jaiswar, Patricia Lampens, Nandish Nanjappa, and Jean-Marc Tortolani. The 4-m International Liquid Mirror Telescope. *Bulletin de la Société Royale des Sciences de Liège*, 87:68–79, Apr 2018. doi:10.25518/0037-9565.7498.

List of Figures

List of Tables

Bibliography

Abercromby, K., Seitzer, P., Barker, E., Cowardin, H., Matney, M., and Parr-Thumm, T. (2010). Michigan orbital debris survey telescope observations of the geosynchronous orbital debris environment.

Africano, J., Lambert, J., Jarvis, K., Stansbery, E., Settecerri, T., Hebert, T., and Mulroonery, M. (1999). Liquid mirror telescope observations of the orbital debris environment: October 1997-january 1999. *NASA JSC-28826, Houston*.

Baltay, C., Snyder, J. A., Andrews, P., Emmet, W., Schaefer, B., Sinnott, J., Bailyn, C., Coppi, P., Oemler, A., Sabbey, C. N., Sofia, S., van Altena, W., Vivas, A. K., Abad, C., Bongiovanni, A., Briceño, C., Bruzual, G., Della Prugna, F., Magris, G., Sánchez, G., Sánchez, G., Schenner, H., Stock, J., Adams, B., Gebhard, M., Honeycutt, R. K., Musser, J., Rengstorf, A., Ferrin, I., Fuenmayor, F., Hernandez, J., Naranjo, O., Rosenzweig, P., Harris, F., and Geary, J. (2002). A Large-Area CCD Camera for the Schmidt Telescope at the Venezuelan National Astronomical Observatory. *Publications of the ASP*, 114:780–794.

Barker, E., Jarvis, K., Africano, J., Jorgensen, K., Parr-Thumm, T., Matney, M., and Stansbery, G. (2005). The geo environment as determined by the cdt between 1998 and 2002. In *4th European Conference on Space Debris*, volume 587, page 135.

Bertin, E. (2006). Automatic Astrometric and Photometric Calibration with SCAMP. In Gabriel, C., Arviset, C., Ponz, D., and Enrique, S., editors, *Astronomical Data Analysis Software and Systems XV*, volume 351 of *Astronomical Society of the Pacific Conference Series*, page 112.

Bertin, E. and Arnouts, S. (1996). SExtractor: Software for source extraction. *Astronomy and Astrophysics Supplement*, 117:393–404.

Bertin, E., Mellier, Y., Radovich, M., Missonnier, G., Didelon, P., and Morin, B. (2002). The TERAPIX Pipeline. In Bohlender, D. A., Durand, D., and

Handley, T. H., editors, *Astronomical Data Analysis Software and Systems XI*, volume 281 of *Astronomical Society of the Pacific Conference Series*, page 228.

Bhawna, C. and Shukla, S. (2011). Iris recognition system using canny edge detection for biometric identification. *International Journal of Engineering Science and Technology*, 3.

Black, S. and Butt, Y. (2010). The growing threat of space debris. *Bulletin of the Atomic Scientists*, 66(2):1–8.

Boër, M., Klotz, A., Laugier, R., Richard, P., Pérez, J. C. D., Lapasset, L., Verzeni, A., Théron, S., Coward, D., and Kennewell, J. (2017). Tarot: a network for space surveillance and tracking operations.

Borra, E. F. (1995). THE NEED FOR A PARADIGM SHIFT IN OPTICAL ASTRONOMY: A SOLUTION GIVEN BY LIQUID MIRRORS AND EXAMPLES OF THEIR APPLICATIONS TO COSMOLOGY. *arXiv e-prints*, pages astro–ph/9503019.

Borra, E. F. (1997). Astronomical Research with liquid mirror telescopes. *arXiv e-prints*, pages astro–ph/9706108.

Borra, E. F., Beauchemin, M., and Lalande, R. (1985). Liquid mirror telescopes - Observations with a 1 meter diameter prototype and scaling-up considerations. *The Astrophysical Journal*, 297:846–851.

Borra, E. F., Content, R., Girard, L., Szapiel, S., Tremblay, L. M., and Boily, E. (1992). Liquid mirrors - Optical shop tests and contributions to the technology. *The Astrophysical Journal*, 393:829–847.

Boyce, W. (2004). Examination of norad tle accuracy using the iridium constellation. *Spaceflight mechanics*, 119:2133–2142.

Bracewell, R. N. (1956). Strip Integration in Radio Astronomy. *Australian Journal of Physics*, 9:198.

Bramich, D. M. (2008). A new algorithm for difference image analysis. *Monthly Notices of the Royal Astronomical Society: Letters*, 386(1):L77–L81.

Canny, J. (1986). A computational approach to edge detection. *IEEE Transactions on Pattern Analysis and Machine Intelligence*, PAMI-8(6):679–698.

Chobotov, V. A., Herman, D. E., and Johnson, C. G. (1997). Collision and debris hazard assessment for a low-Earth-orbit space constellation. *Journal of Spacecraft and Rockets*, 34:233–238.

Choi, J., Jo, J., Yim, H.-S., Choi, E.-J., Cho, S., and Park, J.-H. (2018). Optical tracking data validation and orbit estimation for sparse observations of satellites by the owl-net. *Sensors*, 18:1868.

Close, S., Fletcher, A., Dunham, M., and Linscott, I. (2011). Coherent matched filter signal-processing algorithms for probing the ionosphere using broadband rf data. *Journal of Geophysical Research: Space Physics*, 116(A12).

Coifman, R. R. and Donoho, D. L. (1995). Translation-Invariant De-Noising. In *Antoniadis A., Oppenheim G. (eds) Wavelets and Statistics. Lecture Notes in Statistics*, volume 103.

Council, N. R. (1995). *Orbital Debris: A Technical Assessment*. The National Academies Press, Washington, DC.

Diaz-Ramirez, V., Kober, V., and Álvarez Borrego, J. (2006). Pattern recognition with an adaptive joint transform correlator. *Applied Optics*, 45:5929–5941.

Djupvik, A. A. and Andersen, J. (2010). The Nordic Optical Telescope. *Astrophysics and Space Science Proceedings*, 14:211.

Donoho, D. and M. Johnstone, I. (1999). Adapting to unknown smoothness via wavelet shrinkage. *Journal of the American Statistical Association*, 90.

Duda, R. O. and Hart, P. E. (1972). Use of the hough transformation to detect lines and curves in pictures. *Commun. ACM*, 15(1):11–15.

Dwork, B. M. (1950). Detection of a pulse superimposed on fluctuation noise. *Proceedings of the IRE*, 38(7):771–774.

e2v (2009). Ccd231-84 back illuminated scientific ccd sensor 4096 x 4096 pixels, four outputs non-inverted mode operation. https://www.noao.edu/0.9m/observe/hdi/ccd231-84-bi-nimo.pdf. A1A-765136 Version 2.

Flohrer, T., Lemmens, S., Bastida Virgili, B., Krag, H., Klinkrad, H., Parrilla, E., Sanchez, N., Oliveira, J., and Pina, F. (2013). DISCOS- Current Status and Future Developments. In *6th European Conference on Space Debris*, volume 723 of *ESA Special Publication*, page 38.

Freeman, W. T. and Adelson, E. H. (1991). The design and use of steerable filters. *IEEE Trans. Pattern Anal. Mach. Intell.*, 13(9):891–906.

Gaia Collaboration, Brown, A. G. A., Vallenari, A., Prusti, T., de Bruijne, J. H. J., Mignard, F., Drimmel, R., Babusiaux, C., Bailer-Jones, C. A. L., Bastian, U., and et al. (2016a). Gaia Data Release 1. Summary of the

astrometric, photometric, and survey properties. *Astronomy and Astrophysics*, 595:A2.

Gaia Collaboration, Prusti, T., de Bruijne, J. H. J., Brown, A. G. A., Vallenari, A., Babusiaux, C., Bailer-Jones, C. A. L., Bastian, U., Biermann, M., Evans, D. W., and et al. (2016b). The Gaia mission. *Astronomy and Astrophysics*, 595:A1.

Gehrels, T., Marsden, B. G., McMillan, R. S., and Scotti, J. V. (1986). Astrometry with a scanning CCD. *Astronomical Journal*, 91:1242.

Gorjian, V., Wright, E. L., and McLean, I. S. (1997). Drift Scanning Using Infrared Arrays: A Powerful Method for Background Limited Imaging. *Publications of the ASP*, 109:821–826.

Gunn, J. E., Carr, M., Rockosi, C., Sekiguchi, M., Berry, K., Elms, B., de Haas, E., Ivezić, Ž., Knapp, G., Lupton, R., Pauls, G., Simcoe, R., Hirsch, R., Sanford, D., Wang, S., York, D., Harris, F., Annis, J., Bartozek, L., Boroski, W., Bakken, J., Haldeman, M., Kent, S., Holm, S., Holmgren, D., Petravick, D., Prosapio, A., Rechenmacher, R., Doi, M., Fukugita, M., Shimasaku, K., Okada, N., Hull, C., Siegmund, W., Mannery, E., Blouke, M., Heidtman, D., Schneider, D., Lucinio, R., and Brinkman, J. (1998). The Sloan Digital Sky Survey Photometric Camera. *Astronomical Journal*, 116:3040–3081.

Gunn, J. E., Siegmund, W. A., Mannery, E. J., Owen, R. E., Hull, C. L., Leger, R. F., Carey, L. N., Knapp, G. R., York, D. G., Boroski, W. N., Kent, S. M., Lupton, R. H., Rockosi, C. M., Evans, M. L., Waddell, P., Anderson, J. E., Annis, J., Barentine, J. C., Bartoszek, L. M., Bastian, S., Bracker, S. B., Brewington, H. J., Briegel, C. I., Brinkmann, J., Brown, Y. J., Carr, M. A., Czarapata, P. C., Drennan, C. C., Dombeck, T., Federwitz, G. R., Gillespie, B. A., Gonzales, C., Hansen, S. U., Harvanek, M., Hayes, J., Jordan, W., Kinney, E., Klaene, M., Kleinman, S. J., Kron, R. G., Kresinski, J., Lee, G., Limmongkol, S., Lindenmeyer, C. W., Long, D. C., Loomis, C. L., McGehee, P. M., Mantsch, P. M., Neilsen, Jr., E. H., Neswold, R. M., Newman, P. R., Nitta, A., Peoples, Jr., J., Pier, J. R., Prieto, P. S., Prosapio, A., Rivetta, C., Schneider, D. P., Snedden, S., and Wang, S.-i. (2006). The 2.5 m Telescope of the Sloan Digital Sky Survey. *Astronomical Journal*, 131:2332–2359.

Gural, P. S., Larsen, J. A., and Gleason, A. E. (2005). Matched Filter Processing for Asteroid Detection. *The Astronomical Journal*, 130:1951–1960.

Hartman, P. G. (1993). Long-term sgp4 performance. *Space Control Operations Technical Note J3SOM-TN-93-01. US Space Command, USSPACECOM/J3SO. Colorado Springs, CO.*

Hejduk, M. (2011). Specular and Diffuse Components in Spherical Satellite Photometric Modeling. In *Advanced Maui Optical and Space Surveillance Technologies Conference*, page E15.

Helstrom, C. (1968). *Statistical theory of signal detection*. International series of monographs on electronics and instrumentation. Pergamon Press.

Hester, C. F. and Casasent, D. (1980). Multivariant technique for multiclass pattern recognition. *Applied Optics*, 19:1758–1761.

Hickson, P. (2018). A fast algorithm for the detection of faint orbital debris tracks in optical images. *Advances in Space Research*, 62(11):3078–3085.

Hickson, P., Gibson, B., and Hogg, D. (1993). Large astronomical liquid mirrors. *Publications of the Astronomical Society of the Pacific*, 105:501–508.

Hickson, P., Pfrommer, T., Cabanac, R., Crotts, A., Johnson, B., de Lapparent, V., Lanzetta, K. M., Gromoll, S., Mulrooney, M. K., Sivanandam, S., and Truax, B. (2007). The Large Zenith Telescope: A 6 m Liquid-Mirror Telescope. *Publications of the ASP*, 119:444–455.

Hickson, P. and Richardson, E. H. (1998a). A Curvature-compensated Corrector for Drift-Scan Observations. *Publications of the ASP*, 110(751):1081–1086.

Hickson, P. and Richardson, E. H. (1998b). A Curvature-compensated Corrector for Drift-Scan Observations. , 110(751):1081–1086.

Hinze, A., Schildknecht, T., Floher, T., and Krag, H. (2013). Results of space debris survey observations on highly-eccentric meo orbits. *constellations*, 1:2.

Hoots, F. R. and Roehrich, R. L. (1980). *Spacetrack Report #3: Models for Propagation of the NORAD Element Sets*. U.S. Air Force Aerospace Defence Command, Colorado Springs, CO.

Hsia, C.-H., Chiang, J.-S., and Guo, J.-M. (2011). *Multiple Moving Objects Detection and Tracking Using Discrete Wavelet Transform*.

Illingworth, J. and Kittler, J. (1988). A survey of the hough transform. *Computer Vision, Graphics, and Image Processing*, 44(1):87 – 116.

Jacob, M. and Unser, M. (2004). Design of steerable filters for feature detection using canny-like criteria. *IEEE transactions on pattern analysis and machine intelligence*, 26:1007–19.

Jean, C., Claeskens, J.-F., and Surdej, J. (1999). Surveys with a 4 m Liquid Mirror Telescope. In Morganti, R. and Couch, W. J., editors, *Looking Deep in the Southern Sky*, page 89.

Johnson, N. (2011). Usa space debris environment, operations and policy updates. *48th Session of the Scientific and Technical Subcommittee Committee on the Peaceful Uses of Outer Space, United Nations*, pages 7–18.

Johnson, N. and Klinkrad, H. (2009). The international space station and the space debris environment: 10 years on.

Johnstone, I. and Silverman, B. (1997). Wavelet threshold estimators for data with correlated noise. *Journal of the Royal Statistical Society. Series B: Statistical Methodology*, 59:319–351.

Jordi, C., Gebran, M., Carrasco, J. M., de Bruijne, J., Voss, H., Fabricius, C., Knude, J., Vallenari, A., Kohley, R., and Mora, A. (2010). Gaia broad band photometry. *Astronomy and Astrophysics*, 523:A48.

Kelso, T. (2007). Validation of sgp4 and icd-gps-200 against gps precision ephemerides. In *Paper AAS 07-127 presented at the AAS/AQIAA Spaceflight Mechanics Meeting*.

Kessler, D. J. and Cour-Palais, B. G. (1978). Collision frequency of artificial satellites: The creation of a debris belt. *Journal of Geophysical Research: Space Physics*, 83(A6):2637–2646.

Kumar, B., Pandey, K. L., Pandey, S. B., Hickson, P., Borra, E. F., Anupama, G. C., and Surdej, J. (2018). The zenithal 4-m International Liquid Mirror Telescope: a unique facility for supernova studies. *Monthly Notices of the Royal Astronomical Society*, 476:2075–2085.

Kumar, B. and Shreekar, J. Technical parameters of the 1.3m devasthal optical telescope observatory. https://www.aries.res.in/~1.3m/telSpecs-ver4.pdf. Accessed: 19 December 2018.

Lederer, S., Cowardin, H., Buckalew, B., Frith, J., Hickson, P., Pace, L., Matney, M., Anz-Meador, P., Seitzer, P., Stansbery, E., and Glesne, T. (2016). NASA's Orbital Debris Optical and IR Ground-based Observing Program: Utilizing the MCAT, UKIRT, and Magellan Telescopes. In *Advanced Maui Optical and Space Surveillance Technologies Conference*, page 12.

Levesque, M. (2009). Automatic Reacquisition of Satellite Positions by Detecting Their Expected Streaks in Astronomical Images. In *Advanced Maui Optical and Space Surveillance Technologies Conference*, page E81.

Levesque, M. P. and Buteau, S. (2007). Image processing technique for automatic detection of satellite streaks.

Liou, J.-C., A K, A., Virgili, B., Hanada, T., Krag, H., Lewis, H., Raj, M., M Rao, M., Rossi, A., and Sharma, R. (2013). Stability of the future leo environment – an iadc comparison study.

Liou, J.-C. and Johnson, N. L. (2006). Risks in space from orbiting debris.

McGraw, J. T., Angel, J. R. P., and Sargent, T. A. (1980). A charge-coupled device /CCD/ transit-telescope survey for galactic and extragalactic variability and polarization. In Elliott, D. A., editor, *Conference on Applications of Digital Image Processing to Astronomy*, volume 264 of *Proc. Society of Photo-Optical Instrumentation Engineers (SPIE)*, pages 20–28.

Mehrholz, D., Leushacke, F. W., Jehn, R., Klinkrad, H., and Landgraf, M. (2002). Detecting, tracking and imaging space debris. *ESA Bulletin*, 109:128–134.

Mulrooney, M. and Matney, M. (2007). Derivation and Application of a Global Albedo Yielding an Optical Brightness to Physical Size Transformation Free of Systematic Errors. In *Advanced Maui Optical and Space Surveillance Technologies Conference*, page E81.

Mulrooney, M. and Matney, M. (2008). A New Bond Albedo for Performing Orbital Debris Brightness to Size Transformations. In *59th International Astronautical Congress*, page Paper ID: 343.

Portee, D. S. F. and Loftus, Jr., J. P. (1999). *Orbital debris : a chronology.*

Portree, D. S. and Loftus Jr, J. P. (1999). Orbital debris: A chronology.

Pradhan, B., Hickson, P., and Surdej, J. (2019). Serendipitous detection and size estimation of space debris using a survey zenith-pointing telescope. *Acta Astronautica*, 164:77–83.

Prasad, P., Naidu, G., and Chiranjeevi, K. (2016). Medical image edge detection using mra based wavelet transforms. *International Journal of Latest Trends in Engineering and Technology*, 7:644–650.

Radon, J. (1917). 1.1 über die bestimmung von funktionen durch ihre integralwerte längs gewisser mannigfaltigkeiten. *Classic papers in modern diagnostic radiology*, 5:21.

Radon, J. (1986). On the determination of functions from their integral values along certain manifolds. *IEEE Transactions on Medical Imaging*, 5(4):170–176.

Richards, M. (2014). *Fundamentals of Radar Signal Processing, Second Edition*. McGraw-Hill Education.

ROBONET, T. T. (2019). pydandia. https://github.com/pyDANDIA/. VERSION 0.1.

Sagar, R., Kumar, B., and Omar, A. (2013). Optical Astronomical Facilities at Nainital, India. *ArXiv e-prints*.

Sanders, J. N. (1992). Optimal three-dimensional matched filter processing for detection of point-like moving objects in clutter. Technical report.

Santa Barbara Instrument Group, I. Operating manual research camera models: Stl-1001e, stl-1301e, stl-4020m, stl-6303e and stl-11000m. http://diffractionlimited.com/wp-content/uploads/2016/03/ST-L-Operating-Manual.pdf.

Savvides, M., Kumar, B., and Khosla, P. (2002). Face verification using correlation filters. *3rd IEEE Automatic Identification Advanced Technologies*.

Schaub, H., Jasper, L. E. Z., Anderson, P. V., and McKnight, D. S. (2015). Cost and risk assessment for spacecraft operation decisions caused by the space debris environment. *Acta Astronautica*, 113:66–79.

Schildknecht, T., Schild, K., and Vannanti, A. (2015). Streak Detection Algorithm for Space Debris Detection on Optical Images. In *Advanced Maui Optical and Space Surveillance Technologies Conference*, page 36.

Schroeder, D. J. (1999). *Astronomical optics*. Elsevier.

Singh, S. and Datar, A. (2013). Edge detection techniques using hough transform. *International Journal of Emerging Technology and Advanced Engineering*, 3(6):333–337.

Sobel, I. and Feldman, G. (1968). A 3x3 isotropic gradient operator for image processing. *a talk at the Stanford Artificial Project in*, pages 271–272.

Sona, D., Prayline, R., Dey, D., Jain, A., Das, R., and Olabiyisi, S. (2017). A case study: Edge detection techniques using hough transform and canny edge algorithm. *International Journal of Mechanical Engineering and Technology*, 8:729–740.

Spectral Instruments (2019). 1100s ccd camera. http://www.specinst.com/BrochuresDatasheets/1110sBrochure_2017.pdf.

Surdej, J., Absil, O., Bartczak, P., Borra, E., Chisogne, J.-P., Claeskens, J.-F., Collin, B., De Becker, M., Defrère, D., Denis, S., Flebus, C., Garcet, O., Gloesener, P., Jean, C., Lampens, P., Libbrecht, C., Magette, A.,

Manfroid, J., Mawet, D., Nakos, T., Ninane, N., Poels, J., Pospieszalska, A., Riaud, P., Sprimont, P.-G., and Swings, J.-P. (2006). The 4m international liquid mirror telescope (ILMT). In *Society of Photo-Optical Instrumentation Engineers (SPIE) Conference Series*, volume 6267, page 626704.

Surdej, J., Hickson, P., Swings, J.-P., Habraken, S., Akunov, T., Bartczak, P., Chand, H., Becker, M., Delchambre, L., Finet, F., Kumar, B., Pandey, A., Pospieszalska, A., Pradhan, B., Sagar, R., Wertz, O., Cat, P., Denis, S., J.D., V., M.K., J., P., L., N., N., and Tortolani, J.-M. (2018). The 4-m International Liquid Mirror Telescope. *Bulletin de la Société Royale des Sciences de Liège*, 87:68–79.

Thomas, W., Remko, S., Michiel, R., Marco, L., and W., P. (2019). Using all-sky optical observations for automated orbit determination and prediction for satellites in low earth orbit. In *1st NEO and Debris Detection Conference*.

Tsai, D.-Y. and Lee, Y. (2004). A method of medical image enhancement using wavelet-coefficient mapping functions. volume 2, pages 1091 – 1094 Vol.2.

Vallado, D. and Agapov, V. (2010). Orbit determination results from optical measurements.

Vallado, D. A. and Cefola, P. J. (2012). Two-line element sets–practice and use. In *63rd International Astronautical Congress, Naples, Italy*.

Vallado, D. A., Crawford, P., Hujsak, R., and Kelso, T. S. (2006). Revisiting Spacetrack Report #3. In *American Institute of Aeronautics and Astronautics*, volume 2006-6753, pages 1–88.

Vangeyte, B., Manfroid, J., and Surdej, J. (2002). Study of CCD mosaic configurations for the ILMT: Astrometry and photometry of point sources in the absence of a TDI corrector. *Astronomy and Astrophysics*, 388:712–731.

Williams, J. and G.A., M. (1966). An analysis of satellite optical characteristics data. *Planetary and Space Science*, 14(9):839 – 847.

Wright, D. (2007). Space debris from anti-satellite weapons. *Bulletin of Atomic Scientists*, 1:1–12.

Wright, J. F. and Mackay, C. D. (1981). The Cambridge Charge-Coupled Device / CCD / System. In *Society of Photo-Optical Instrumentation Engineers (SPIE) Conference Series*, volume 290 of *Proc. Society of Photo-Optical Instrumentation Engineers (SPIE)*, page 160.

Xu, X. and Xiong, Y. (2013). A method for calculating collision probability between space objects. *Research in Astronomy and Astrophysics*, 14.

Zaritsky, D., Schectman, S. A., and Bredthauer, G. (1996). The Great-Circle Camera: A New Drift-Scanning Instrument. *Publications of the ASP*, 108:104.

Zhang, B., Wang, Z., and Zhang, Y. (2017). *Collision risk investigation for an operational spacecraft caused by space debris.* Cambridge, UK: Cambridge University Press.